

**TECHNICAL  
TRANSACTIONS**

**CHEMISTRY**

**CZASOPISMO  
TECHNICZNE**

**CHEMIA**

**ISSUE  
1-Ch (4)**

**ZESZYT  
1-Ch (4)**

**YEAR  
2016 (113)**

**ROK  
2016 (113)**



**WYDAWNICTWO  
POLITECHNIKI  
KRAKOWSKIEJ**

# TECHNICAL TRANSACTIONS

# CZASOPISMO TECHNICZNE

## CHEMISTRY

## CHEMIA

ISSUE 1-Ch (4)  
YEAR 2016 (113)

ZESZYT 1-Ch (4)  
ROK 2016 (113)

Chairman of the Cracow  
University of Technology Press  
Editorial Board

**Tadeusz Tatar**

Przewodniczący Kolegium  
Redakcyjnego Wydawnictwa  
Politechniki Krakowskiej

Chairman of the Editorial Board

**Józef Gawlik**

Przewodniczący Kolegium  
Redakcyjnego Wydawnictw  
Naukowych

Scientific Council

**Jan Błachut  
Tadeusz Burczyński  
Leszek Demkowicz  
Joseph El Hayek  
Zbigniew Florjańczyk  
Józef Gawlik  
Marian Giżejowski  
Sławomir Gzell  
Allan N. Hayhurst  
Maria Kuśnierova  
Krzysztof Magnucki  
Herbert Mang  
Arthur E. McGarity  
Antonio Monestiroli  
Günter Wozny  
Roman Zarzycki**

Rada Naukowa

Chemistry Series Editor

**Krzysztof Pieliowski**

Redaktor Serii Chemia

Section Editor  
Editorial Compilation

**Dorota Sapek  
Aleksandra Urzędowska**

Sekretarz Sekcji  
Opracowanie redakcyjne

Proofreading

**Katarzyna Mstowska  
Karolina Rymut  
Małgorzata Sikora**

Korekta

Native Speaker

**Justin Nnorom**

Weryfikacja językowa

Typesetting

**Anna Basista**

Skład i łamanie

Cover Design

**Michał Graffstein**

Projekt okładki

Basic version of each Technical Transactions magazine is its online version

Pierwotną wersją każdego zeszytu Czasopisma Technicznego jest jego wersja online

[www.ejournals.eu/Czasopismo-Techniczne](http://www.ejournals.eu/Czasopismo-Techniczne) [www.technicaltransactions.com](http://www.technicaltransactions.com) [www.czasopismotechniczne.pl](http://www.czasopismotechniczne.pl)



**Series Chemistry**

1-Ch/2016

**Editor-in-chief:**

Krzysztof PIELICHOWSKI, Cracow University of Technology, Poland

**Editorial Board:**

Dariusz BOGDAŁ, Cracow University of Technology, Poland

Marek CZERNICKI, École Nationale Supérieure de Chimie de Lille, France

Vladimír ČABLÍK, Technical University of Ostrava, Czech Republic

Józef HOFFMANN, Wrocław University of Technology, Poland

Teofil JESIONOWSKI, Poznan University of Technology, Poland

James LEWICKI, Lawrence Livermore National Laboratory, United States

James NJUGUNA, Robert Gordon University Aberdeen, Great Britain

Mária OMASTOVÁ, Polymer Institute of Slovak Academy of Sciences, Bratislava, Slovakia

Sascha ROHN, University of Hamburg, Germany

Julian PLEWA, Münster University of Applied Sciences, Germany

Małgorzata SZYNKOWSKA, Lodz University of Technology, Poland

Zygmunt KOWALSKI, Cracow University of Technology, Poland

GABRIELA BERKOWICZ, DARIUSZ BRADŁO, WITOLD ŻUKOWSKI\*

## CENOSPHERES AS AN INNOVATIVE FLUIDISED BED MATERIAL

---

## CENOSFERY JAKO INNOWACYJNY MATERIAŁ ZŁOŻA FLUIDALNEGO

### Abstract

In this paper, the possibility of achieving a stable fluidised bed made of the cenospheres was examined. Cenospheres are the waste material from hard coal power plants. This material is perfectly spherical, and it is thin-walled and filled with gases (mainly CO<sub>2</sub>, N<sub>2</sub>). Because of their low density, particle size and sphericity, cenospheres can be easily fluidised even at low flow rates of the fluidising medium. Moreover, the application of acoustic waves during the fluidisation of cenospheres removes the apparent effect of double stationary states and moves the minimum fluidisation velocity into lower gas flow rates.

*Keywords: cenospheres, fluidised bed, minimum fluidization velocity*

### Streszczenie

W niniejszej pracy zbadano możliwość stworzenia złoża fluidalnego z materiału cenosfer. Cenosfery są materiałem odpadowym z elektrowni. Idealnie kuliste, o cienkich ściankach, wypełnione w środku gazami (CO<sub>2</sub>, N<sub>2</sub>) są materiałem niezwykle lekkim. Ze względu na niewielkie wartości gęstości, sferyczny kształt oraz rozmiary ziaren cenosfery dają się łatwo sfluidyzować już przy niewielkich przepływach czynnika fluidyzującego. Zastosowanie fal akustycznych podczas fluidyzacji cenosfer niweluje pozorny efekt podwójnej stacjonarności oraz przesuwa początek fluidyzacji w kierunku niższych wartości przepływu gazu przez złożo.

*Słowa kluczowe: cenosfery, złożo fluidalne, prędkość minimum fluidyzacji*

---

\* Ph.D. Eng. Gabriela Berkowicz, M.Sc. Eng. Dariusz Bradło, Prof. Ph.D. Eng. Witold Żukowski, Faculty of Chemical Engineering and Technology, Cracow University of Technology.

## 1. Introduction

The fluidisation phenomenon is based on the suspension of solid particles in a stream of liquid or gas flowing from the bottom of the reactor [1]. In this way, solid particles take the form of pseudo-liquid, thereby gaining properties that are advantageous from the technological point of view. The most important benefits of a fluidised bed are good temperature equalisation, good mass and heat transfer as well as a low pressure drop [2]. These features allow for the fluidisation to be applied in many industrial applications, including coating [3], combustion [4] and heterogeneous synthesis [5–7]. Not every type of powder is able to achieve stable fluidisation, due to the fact that it depends on the individual characteristics of the powder, such as shape, particle size and density of the material. The ability of the powder to fluidise can be assessed on the basis of the classification created in 1973 by the Geldart [8]. Material density and the average grain size are the main criteria for this powder classification. Geldart's powder classification is shown in Figure 1.

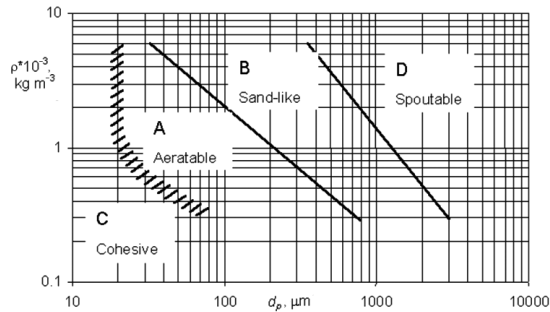


Fig. 1. Geldart's powder classification

Class C powders have the smallest size, which typically does not exceed 30 microns. Such small grains have maximum cohesiveness, hence, they tend to stick together. A large interaction force between particles makes the formation of a stable fluidisation for this type of material difficult, and it often results in channelling. Examples of Group C powders include powder, flour and starch [9]. Group A powders are materials that can be easily fluidised. Such particles have a relatively small average particle size (30–100  $\mu\text{m}$ ) and a low apparent density, below 1.4  $\text{g/cm}^3$ . Fluidisation of Group A powders is relatively mild and is characterised by small bubbles, high bed expansion and good circulation of the grains [10]. The gas velocity at which bubbles are observed is significantly higher than the minimum fluidisation velocity. The catalyst for fluid catalytic cracking (FCC) is an example of a Class A material. Geldart assigned powders with a particle size of 0.1–1 mm to class B. These powders readily form a bubbling fluidised bed (the minimum fluidisation velocity is equal to the minimum bubbling velocity). The bubbling fluidised beds are classified as heterogeneous beds because a large part of the gas is enclosed in bubbles. Quartz sand with a diameter of approx. 0.5 mm is the most typical representative of group B [11]. Grains greater than 1 mm and with high density (Class D) can be fluidised only at a large momentum value. The bed made out of this material is characterised by large bubbles, whose velocity is lower than the velocity of remaining gas in the emulsion. The low level of mixing also makes the transport of mass and heat is low.

In this paper, the possibility of achieving a stable fluidised bed made of the cenospheres was examined. Cenospheres are the waste material from hard coal power plants equipped with pulverised boilers. It is estimated that cenospheres constitute up to 5% mass of fly ash [12]. This material is perfectly spherical, and it is thin-walled and filled with gases (mainly  $\text{CO}_2$ ,  $\text{N}_2$ ). In addition, cenospheres have low density (ca.  $0.7 \text{ g cm}^{-3}$ ) and they are characterised by high temperature resistance (up to  $1300^\circ\text{C}$ ), mechanical strength (up to 6 on the Mohs scale) and a low thermal conductivity (about  $0.07 \text{ Wm}^{-1}\text{K}^{-1}$ ) [13, 14]. The physical properties of cenospheres indicate that this material could be easily introduced in the fluidised state. The application of the cenosphere material as a carrier for the catalyst grains may be very beneficial in the processes occurring in a catalytic fluidised bed. Covering cenospheres with a catalyst powder allows to obtain catalyst particles with a much lower density compared to the original material grains, so that it will be possible to lower the minimum fluidisation velocity and the carrying processes at low gas flows, and therefore, cause a longer contact time of the reactants with the catalyst.

## 2. Experimental Methods

Cenospheres were supplied by the Polanec Power Plant, where its acquisition is based on the wet method. Raw microspheres were subjected to initial drying at  $105^\circ\text{C}$  for 12 h, followed by purification in boiling water according to the procedure described before [15]. Furthermore, the cenospheric material was sieved and divided into four fractions: with a particle size less than 45 microns, 45–71 microns, 71–100 microns, 100–125 microns. The processes of fluidisation of the separated fractions of cenospheres were examined by passing a gas through the bed of each fraction of the material. In order to measure the pressure drop caused by the bed of cenospheres, a laboratory installation was built. A transparent flow tubular reactor, having an inner diameter of 3.6 cm and a height of about 25 cm, was used. The pressure sensor was placed under the bottom sieve. Nitrogen was used as the fluidising medium. The measuring system scheme is shown in Figure 2.

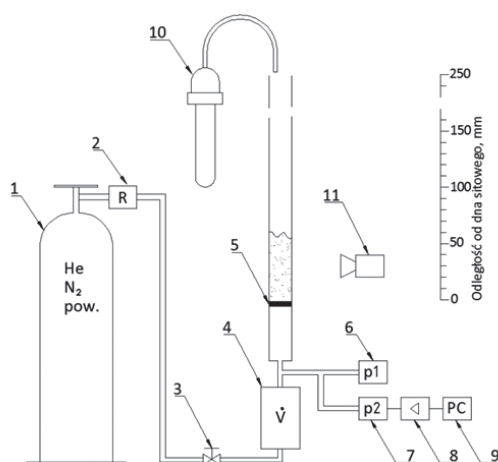


Fig. 2. Installation diagram for measuring the pressure drop: 1 – compressed gas, 2 – reducer, 3 – valve, 4 – flow meter, 5 – bottom sieve, 6, 7 – pressure sensors, 8 – converter, 9 – computer, 10 – dedusting system, 11 – camera

At first, the pressure drop that occurred during gas flow through an empty reactor was determined. The measured dependence of the pressure drop, caused only by the bottom sieve and the filter with a pore size of 10–20 microns, was linear. Thus, it was possible to calculate an arbitrary pressure drop caused only by one layer of cenospheres.

### 3. Results and Discussion

The plots of the pressure drop versus the velocity of the fluidising gas were calculated on an empty cross-section of the reactor, which is shown in Figure 3a. Fluidisation is characterised by a constant level of pressure drop, despite increasing the nitrogen velocity, and the beginning of this stabilisation indicates the minimum fluidisation velocity. The value of the minimum fluidisation velocity for each fraction of material was determined from the curve by extrapolating linear lines within the ranges of the lowest and the highest gas flow rates. The abscissa of the intersection point of these lines represents the minimum gas velocity at which fluidisation occurs (Fig. 3b). The coefficients of regression equations for the range of lower and higher flow rate of the gas through the bed, and the minimum fluidisation velocity calculated based on them, were shown in Table 1.

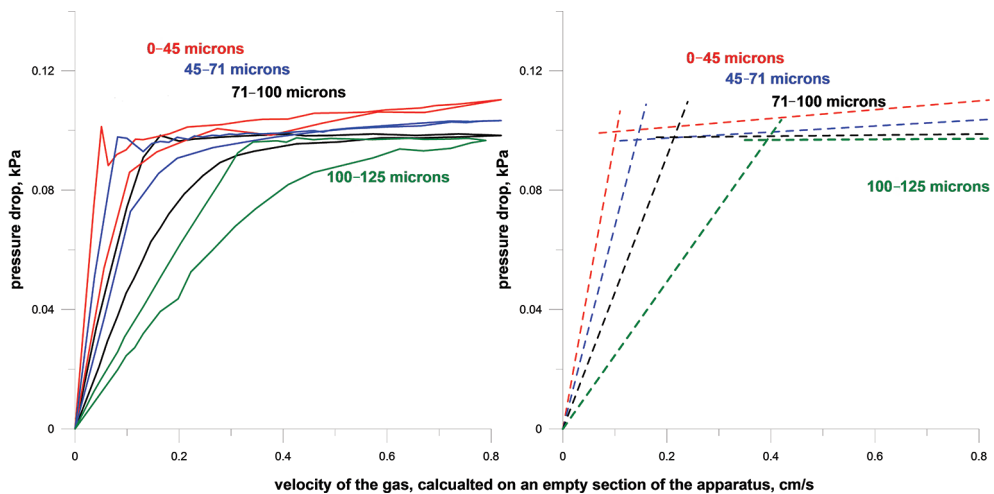


Fig. 3. The dependence of the pressure drop in the layer of cenospheres with a different grain size versus the flow rate of nitrogen: a) actual course of the curves b) extrapolation within ranges of the lowest and the highest flow rates of gas

All of the examined fractions of cenospheres can be easily introduced in the fluidised state. The stable fluidised states of the tested materials were achieved at low flow rate of the fluidising gas (from 0.1 to 0.4 cm s<sup>-1</sup>). The process of fluidisation was mild because the layers were characterised by a large expansion of the bed and a high degree of mixing.

**Coefficients of regression equations for the lower and higher flow rate of the gas through the bed and the minimum fluidisation velocity**

Cenospheres fraction $\mu\text{m}$	Bed mass $g$	Lower range of flow rate of the gas, $\Delta p = a^*u$		Higher range of flow rate of the gas, $\Delta p = a^*u + b$			Minimum fluidisation velocity, $U_{mf}$ $\text{cm/s}$
		$a$	$R^2$	$a$	$b$	$R^2$	
0–45	10	0.9679	1.000	0.0148	0.0981	0.986	0.103
45–71	10	0.6797	1.000	0.0101	0.0954	0.973	0.143
71–100	10	0.4568	1.000	0.0018	0.0974	0.439	0.214
100–125	10	0.2465	1.000	0.0010	0.0964	0.132	0.393

In the following study, the fraction of 71–100  $\mu\text{m}$  was purified by heating in water at a temperature of 90°C. Therefore, broken and perforated cenospheres sank to the bottom. The purified fraction of cenospheres is labelled as IMS (intact microspheres). The fluidisation processes of fraction 71–100 microns before and after purification are summarised in Fig. 4. The results of the coefficients of linear regression equations derived from data, obtained in the low and the high value of the fluidising gas flow, are presented in Table 2.

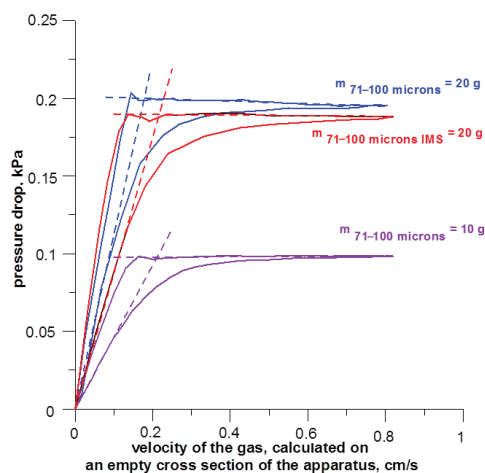


Fig. 4. The dependence of the pressure drop in the layer of cenospheres with a particle size of 71–100  $\mu\text{m}$  versus the flow rate of nitrogen

The pressure drop in a layer of cenospheres is directly related to the weight of the bed. The ratio of pressure drop for fraction 71–100 microns with masses of 10 and 20 grams is the same as the ratio of their masses. It is known that the minimum fluidisation velocity does not depend on the weight of the bed. Minimal difference between minimum fluidisation velocities of fraction 71–100 microns, calculated for 10 g and 20 g of bed mass, can be

explained by a greater stability of the heavier bed and, thereby, the greater accuracy of  $U_{mf}$  determination. The minimum fluidisation velocities of raw and purified cenospheres slightly differ from each other (0.214 and 0.220 respectively). However, this difference is not the result of purification because the weight loss after heating was less than 2%, and thus it can be neglected.

Table 2

**Coefficients of regression equations for the lower and higher flow rate of the gas through the bed and the minimum fluidisation velocity for raw and purified cenospheres of 71–100  $\mu\text{m}$**

Cenosphere fraction $\mu\text{m}$	Bed mass g	Lower range of flow rate of gas, $\Delta p = a*u$		Higher range of flow rate of gas, $\Delta p = a*u + b$			Minimum fluidization velocity, $U_{mf}$ cm/s
		$a$	$R^2$	$a$	$b$	$R^2$	
71–100	10	0.4568	1.000	0.0018	0.0974	0.439	0.214
71–100	20	1.1235	0.983	-0.0081	0.2015	0.892	0.178
71–100 IMS	20	0.8628	0.999	-0.0030	0.1907	0.559	0.220

Furthermore, the characteristic hysteresis loop after decreasing of fluidising gas flow rate was observed. The phenomenon of the occurrence of the local maximum, which is the result of large interaction between small grains, is known. Dispersion of the hysteresis is large, which suggests the simultaneous existence of two steady states. For example, fluidisation of 20 g of 71–100 microns IMS could be carried out at a gas velocity of 0.3 cm/s and with a pressure drop equal to approx. 0.17 and 0.19 kPa, respectively. In order to exclude the existence of two stationary states, experiments for fractions 45–71 and 71–100 were repeated with the additional presence of acoustic waves with different frequencies. An example plot for a fraction of cenospheres with a grain size 45–71  $\mu\text{m}$  was shown in Figure 5. The minimum fluidisation velocities were determined on the basis of extrapolation and are summarised in Table 3.

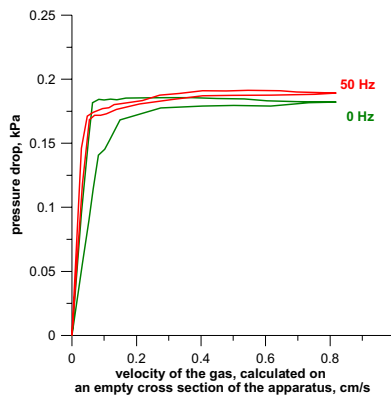


Fig. 5. Changes in pressure drop during the fluidisation of cenospheres with a particle size 45–71  $\mu\text{m}$  in the presence of sound waves of 50 Hz

Table 3

**Minimum fluidisation velocity of cenospheres with a grain size of 45–71  $\mu\text{m}$  and 71–100  $\mu\text{m}$  in the presence of the acoustic waves**

Particle Size Distribution $\mu\text{m}$	Frequency of a acoustic Wave Hz	Minimum Fluidisation Velocity cm/s
45–71	0	0.107
	50	0.052
	100	0.072
71–100	0	0.220
	25	0.100
	50	0.108
	75	0.105
	100	0.107
	150	0.131

The application of acoustic waves during fluidisation of cenospheres removes the apparent effect of double stationary states and moves the minimum fluidisation velocity into lower gas flow rates.

The application of sound waves from the 20–100 Hz range makes the minimum fluidisation velocity of cenospheres fraction with a grain size of 71–100 reduced from 0.220 cm/s (for an experiment without vibroacoustics) to the range of 0,100–0,108 cm/s. After a certain level of the impact of sound waves from the range of 20–100 Hz, the efficiency of the influence of lower sound waves on the minimum fluidisation velocity is decreased, and for waves of 150 Hz, this difference in velocities is smaller. It can be stated that the damping of waves with higher frequencies occurs because of the inertia of the individual grains, and it is greater than for the lower waves.

#### 4. Conclusions

Because of their low density, particle size and sphericity, cenospheres can be easily fluidised even at low flow rates of the fluidising medium. For example, the minimum fluidisation velocity of cenospheres with a grain size of 45–71 microns is 0.107 cm/s. Moreover, acoustic waves of 50 Hz may reduce this value to 0.052 cm/s. The physical properties of cenospheres and the easiness of its fluidisation process allow to classify this material to group A in the Geldart's classification.

## References

- [1] Orzechowski Z., *Przepływy dwufazowe jednowymiarowe ustalone adiabaticzne*, PWN, Warszawa 1990.
- [2] Kunii D., Levenspiel O., Brenner H., *Fluidization Engineering*, Second edition, Butterworth-Heinemann, Newton 1991.
- [3] Dewettinck K., Huyghebaert A., *Fluidized bed coating in food technology*, Trends in Food Science & Technology, 10(4–5), 1999, 163–168.
- [4] Wielgościński G., *Przegląd technologii termicznego przekształcania odpadów*, Nowa Energia, 1, 55, 2011.
- [5] Adlhoch W., Sato H., Wolff J., *High-Temperature Winkler Gasification of Municipal Solid Waste*, 2000 Gasification Technologies Conference, San Francisco 2000, [https://www.netl.doe.gov/File%20Library/Research/Coal/energy%20systems/gasification/gasifiedia/5-ASADAL\\_BOARD\\_bbs02.pdf](https://www.netl.doe.gov/File%20Library/Research/Coal/energy%20systems/gasification/gasifiedia/5-ASADAL_BOARD_bbs02.pdf) (access: 13.04.2016).
- [6] Contractor R.M., Garnett D.I., Horowitz H.S., Bergna H.E., Patience G.S., Schwartz J.T., Sisler G.M., *A New Commercial Scale Process for n-Butane Oxidation to Maleic Anhydride Using a Circulating Fluidized Bed Reactor*, Studies in Surface Science and Catalysis, 82, 1994, 233–242.
- [7] Zhou J., *Fluidization Technology and its Applications*, <http://www.ispe.org/great-lakes/zhou-fluidization-basics-2010-presentation.pdf>, 2010 (access: 13.04.2016).
- [8] Geldart D., *Types of Gas Fluidization*, Powder Technology, 7, 1973, 285–292.
- [9] Thomas B., Mason M.O., Squires A. M., *Some behaviors of shallow vibrated beds across a wide range in particle size and their implications for powder classification*, Powder Technology, 111, 2000, 34–49.
- [10] Lii-Ping Leu, Fu-Chien Tsai, *Hydrodynamics of Geldart group A particles in gas-solid fluidized beds*, Korean J. Chem. Eng., 26(2), 2009, 513–517.
- [11] Hariprasad J. Subramani, M.B. Mothivel Balaiyya, Lima Rose Miranda, *Minimum fluidization velocity at elevated temperatures for Geldart's group-B powders* Experimental Thermal and Fluid Science, 32, 2007, 166–173.
- [12] Anshits N.N., Mikhailova O.A., Salanov A.N., Anshits A.G., *Chemical composition and structure of the shell of fly ash non-perforated cenospheres produced from the combustion of the Kuznetsk coal (Russia)*, Fuel, 89(8), 2010, 1849–1862.
- [13] Kruger R.A., *The Use of Cenospheres in Refractories*, Energeia, Center for Applied Energy Research, 7, 4, 1996.
- [14] Elpologistyka Sp. z o.o. homepage: *Raport z badań mikrosfery*, <http://www.elpologistyka.pl/wp-content/uploads/2015/11/Raport-z-badan-mikrosfery1.pdf> (access: 13.04.2016).
- [15] Bradło D., Żukowski W., Czupryński P., Witkowski K., *Pozyskiwanie oraz dobór metody frakcjonowania cenosfer z popiołów lotnych/Acquisition and choice of method for fractionation of cenospheres from fly ashes*, Przemysł Chemiczny, 93(7), 2014.

MAŁGORZATA DJAS, MAREK HENCZKA\*

INFLUENCE OF MIXING ON THE COURSE  
OF REACTIVE EXTRACTION OF CITRIC ACID  
USING SUPERCRITICAL CO<sub>2</sub>

WPLYW MIESZANIA NA PRZEBIEG REAKTYWNEJ  
EKSTRAKCJI KWASU CYTRYNOWEGO  
Z UŻYCIEM CO<sub>2</sub> W STANIE NADKRYTYCZNYM

Abstract

This paper presents the investigation results of mixing effects on the course of reactive extraction of citric acid from an aqueous solution, with the use of supercritical CO<sub>2</sub> and tertiary aliphatic amines. The influence of the mixing rate and the mixing time on the efficiency of the considered process has been studied. This paper also presents the influence of the tertiary amine chain length and the molar ratio of reactants on the efficiency of the process.

*Keywords: reactive extraction, supercritical CO<sub>2</sub>, citric acid*

Streszczenie

W artykule przedstawiono badania dotyczące wpływu mieszania na przebieg procesu ekstrakcji reaktywnej kwasu cytrynowego z roztworu wodnego z zastosowaniem CO<sub>2</sub> w stanie nadkrytycznym oraz trzeciorzędowych alifatycznych amin. Zbadano wpływ szybkości i czasu mieszania na efektywność rozważanego procesu. Zaprezentowano również wyniki badań wpływu długości łańcucha trzeciorzędowej aminy i stosunku molowego reagentów na efektywność procesu.

*Słowa kluczowe: ekstrakcja reaktywna, CO<sub>2</sub> w stanie nadkrytycznym, kwas cytrynowy*

\* Ph.D. Małgorzata Djas, Ph.D. D.Sc. Marek Henczka, Faculty of Chemical and Process Engineering, Warsaw University of Technology.

## 1. Introduction

Nowadays, modern chemical engineering is directed at the design of efficient and environmentally friendly industrial technologies. An increase of the efficiency of the applied technologies can be achieved by the integration of the following step processes: chemical reaction and simultaneous separation of products from the reaction environment. Reactive extraction is an example of such a process. Its application allows for a significant intensification of transport processes by increasing the rates of mass transfer and chemical reactions. In addition, this method allows for beneficial changes in the equilibrium position of a reversible chemical reaction, and therefore, increases its efficiency and selectivity for the desired product.

The production of carboxylic acids recently became of high interest to the chemical industry. Organic acids play an important role as pharmaceuticals and chemical intermediates, additives in the food industry, precursors of synthetic resins and biodegradable polymers. Recently, fermentation technology has been found to be an attractive and effective process for producing carboxylic acids. However, the product must be recovered from fermentation broth. The recovery of carboxylic acids from the fermentation broth is an important step in the production process, and it generates most of the economic and environmental problems. About 60% of the total production costs are created by downstream processing. The conventional industrial method of the separation of carboxylic acids from a fermentation broth is still acid precipitation in the form of insoluble calcium salts. The main disadvantages of this method are the high amount of by-product calcium sulphate and the high consumption of sulphuric acid [1]. Reactive extraction of acid using various suitable extractants has been found to be an alternative and effective method, when compared to the conventional process. The conventional reactive extraction processes are performed with the use of organic solvents. However, the use of organic solvents is a significant burden for the environment, it reduces the safety of the process, and it may also adversely affect the activity of the biochemical reagents. Therefore, eliminating organic solvents from industrial extraction processes and replacing them with safe media, e.g. supercritical CO<sub>2</sub>, is the basis for the dynamic development of industrial technologies using supercritical fluids.

Reactive extraction using supercritical fluids has a great potential as a new, efficient and clean method, in comparison with conventional methods of extraction. Moreover, its application is consistent with the principles of green chemistry and technology. Supercritical carbon dioxide is the most commonly used fluid due to its specific properties: non-toxicity, non-flammability, inertness and a low critical point ( $P_c = 7.38$  MPa,  $T_c = 304.3$  K). Supercritical fluids are of densities in-between those of liquids and gases, while their viscosities and diffusivities are closer to that of gases. Supercritical fluids also offer advantageous physicochemical properties by being good solvents. The application of reactive extraction using supercritical CO<sub>2</sub> for the separation of carboxylic acids from an aqueous solution is an innovative technology that is still under development.

This paper is dedicated to the reactive extraction process of citric acid (HOOC-CH<sub>2</sub>-C(OH)(COOH)-CH<sub>2</sub>-COOH) from an aqueous solution using supercritical CO<sub>2</sub> and tertiary aliphatic amines. The influence of the mixing rate and the mixing time on the efficiency of the considered process is presented. This paper presents the influence of the tertiary amine chain length and the molar ratio of reactants on the efficiency of the process.

## 2. Background of the process

### 2.1. Principles of reactive extraction of carboxylic acids

Reactive extraction of carboxylic acids is based on complex formation, in which the extractant soluble in the supercritical  $\text{CO}_2$  phase reacts with carboxylic acid in the aqueous phase, and the formed complex is solubilised into the supercritical fluid phase. The solubility of carboxylic acids in supercritical  $\text{CO}_2$  is very low because carboxylic acids are polar and  $\text{CO}_2$  is nonpolar [2]. In order to increase solubility, polar entrainers or reactants are added to the supercritical fluid phase. There are two categories of extractants used in reactive extraction of carboxylic acids: high molecular weight aliphatic amines and phosphorus bonded oxygen bearing extractants [3]. For the reactive extraction of carboxylic acid from an aqueous solution, long chain aliphatic primary, secondary and tertiary amines are known to be efficient and selective extractants. In the considered system, tertiary amines are used because primary amines are soluble in the aqueous phase and secondary amines react irreversibly with carboxylic acids, which makes stripping difficult [4]. Moreover, primary and secondary amines react with  $\text{CO}_2$  at low temperatures and pressures to form carbamates [5].

### 2.2. Mechanism of acid-amine complex formation

The stoichiometry of acid and amine in the acid-amine complex varies with the properties and concentrations of the amine, acid and diluents [6]. The notation (p,q) of the complex denotes p as the number of acid molecules, and q as the number of amine molecules. For example, the extraction of citric acid with trioctylamine dissolved in organic solvents is followed by the formation of acid-amine complexes of the (1,1) and (1,2) type, or their aggregates – (2,3) complex. The formation of the acid-amine complex is a reversible reaction.

Two possible structures of the citric acid-amine complex are shown in Fig. 1. Two major mechanisms have been reported for the extraction of carboxylic acids using amine: ion-pair formation and hydrogen bonds. Interaction between the first acid and the amine molecules is different from the interaction between the second acid and the (1,1) complex. The first acid forms an ion pair or a hydrogen bond with the amine, while the second acid forms a hydrogen bond to the carboxylate of the first acid [7].

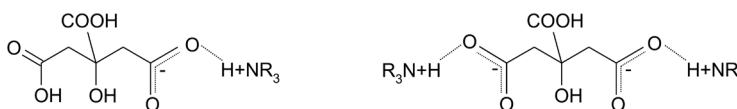


Fig. 1. Structure of a) (1,1) and b) (1,2) citric acid-amine complexes

## 3. Experimental

### 3.1. Materials

Citric acid with purity of > 99% was purchased from Merck. As the extractants formed complexes with citric acid, tertiary aliphatic amines have been applied: tripropylamine (TPA, Merck, > 98%), tributylamine (TBA, Merck, > 99%), trioctylamine (TOA, Merck, > 93%).

Liquid CO<sub>2</sub> with purity of more than 99.995% was purchased from Linde Gas. The aqueous solution of citric acid with an initial concentration equal to 0.014 mol dm<sup>-3</sup> was prepared by diluting citric acid with distilled water.

### 3.2. Apparatus and experimental procedure

The schematic diagram of the system for the supercritical CO<sub>2</sub> reactive extraction experiments is shown in Fig. 2.

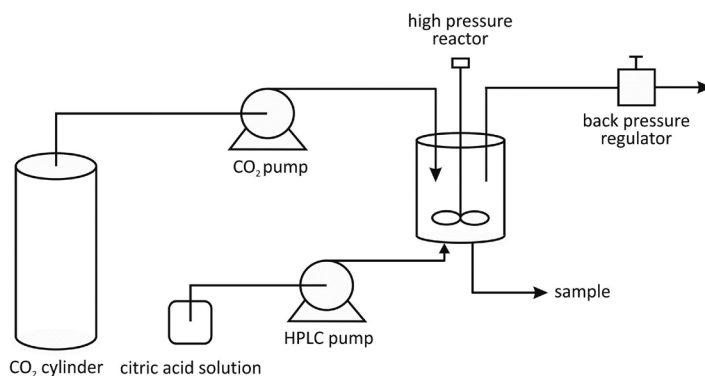


Fig. 2. Schematic diagram of the system for supercritical fluid reactive extraction

The main component of the apparatus consists of a high pressure reactor (Amar Equipments, 100 cm<sup>3</sup>, max. pressure 20 MPa). A piston pump (Supercritical Fluid Technologies, SFT-10) is used to deliver CO<sub>2</sub> to the high pressure reactor. During experiments on the influence of the amine chain length and the molar ratio of reactants, 50 cm<sup>3</sup> of citric acid solution (0.014 mol dm<sup>-3</sup>) and a specific volume of tertiary amine (TPA, TBA, TOA) was placed in the reactor, in order to keep a constant initial amine concentration of 0.014, 0.028, 0.042, 0.056 mol dm<sup>-3</sup> (molar ratio amine and acid 1:1, 2:1, 3:1, 4:1). Liquid CO<sub>2</sub> was subsequently purged into the system. The experiments were performed in a batch system for 60 minutes at a pressure of 16 MPa, a temperature of 308 K, and stirrer speed of 500 rpm.

During the experiments, according to the influence of the mixing rate, tertiary amine TPA with a constant initial concentration of 0.056 mol dm<sup>-3</sup> was placed in the reactor. Liquid CO<sub>2</sub> was subsequently purged into the system and the back pressure regulator was closed for the CO<sub>2</sub> pressurising process in the reactor with the pump. When the system pressure reached the desired value of 16 MPa, amine (TPA) and carbon dioxide were heated and mixed to reach the desired temperature of 308 K. The back pressure regulator was opened to enable CO<sub>2</sub> flow. When the pressure and the temperature reached the desired conditions, 50 cm<sup>3</sup> of citric acid solution (0.014 mol dm<sup>-3</sup>) was purged into the reactor with the HPLC pump (Knauer, Smartline 1000). An equal volume 50 cm<sup>3</sup> of the aqueous phase and the supercritical CO<sub>2</sub> phase were then agitated (250, 350, 500 rpm). All experiments were performed as batch reactive extractions, at a pressure of 16 MPa and a temperature of 308 K. Samples of the aqueous phase were taken after 1, 5, 10, 20 and 60 min. using the valve at the bottom of the reactor.

The applied experimental conditions were limited by the solubility of tertiary amines, in particular of trioctylamine, in supercritical CO<sub>2</sub>. The concentration of citric acid in the aqueous phase was determined by titration with aqueous sodium hydroxide, in the presence of phenolphthalein as the indicator.

#### 4. Results and discussion

The efficiency of reactive extraction of citric acid using tertiary amine and supercritical CO<sub>2</sub> ( $E$ ) is defined as:

$$E = \frac{C_{A0} - C_A}{C_{A0}} \cdot 100\% \quad (1)$$

where:

$C_{A0}$  – the initial concentration of citric acid in the aqueous phase,

$C_A$  – the concentration of citric acid in the aqueous phase after the process.

The results of the performed experiments are presented in Fig. 3, 4 and 5.

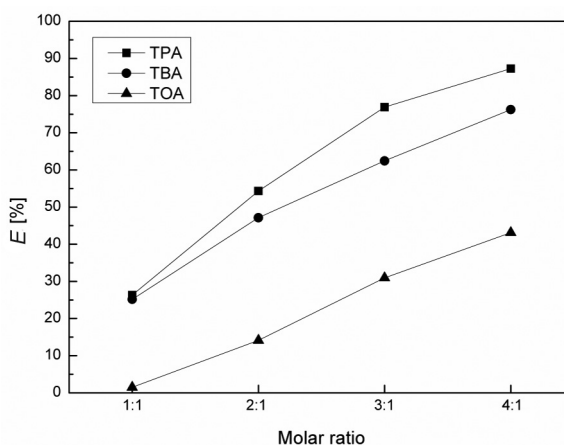


Fig. 3. Influence of the tertiary amine chain length and the molar ratio of reactants on the process efficiency (16 MPa, 308 K, 60 min, 500 rpm)

The aim of the performed experiments was to determine the influence of the molar ratio of the amine and acid reactants (1:1, 2:1, 3:1, 4:1), and the type of tertiary amine, on the final efficiency of the reactive extraction process. The results of experiments show that the molar ratio of citric acid and the amine is an important parameter affecting the efficiency of the process. It has been shown that an increase of the mole ratio of the amine, according to the concentration of citric acid, increases the process efficiency. The highest process efficiency, regardless of the amine, was obtained with a 4:1 molar ratio of the reactants. The highest efficiency of 87.28% was obtained using tripropylamine with 4:1 molar ratio. In the case of trioctylamine, a 4-fold increase of the concentration of amine allows to increase the process efficiency to 43.13%.

As shown in Fig. 3, the reactive extraction efficiency of carboxylic acids depends on the chain length of the tertiary aliphatic amine. The efficiency of the process using supercritical CO<sub>2</sub> increases with decrease of the amine chain length. The highest efficiency was obtained for tripropylamine at all molar ratios, while the least efficient process was using trioctylamine. The extraction efficiency increases with the chain length of tertiary amines in an active (polar) diluent, such as 1-octanol, however, it decreases with the chain length in an inactive (nonpolar) diluent, such as n-heptane [8,9]. The value of the dipole moment of a tertiary amine increases with the number of carbon atoms in the amine chain. The basicity of amines increases with their dipole moments. In the case of an active diluent with increasing polarity of the formed acid-amine complex, with an increasing amine chain length in the complex, the solubility and efficiency of the process increases. In the case of a nonpolar diluent, the more inert the diluent, the more unfavourable it is for polar complexes.

Carbon dioxide is a nonpolar, inactive solvent. Therefore, the efficiency of the reactive extraction of citric acid using supercritical CO<sub>2</sub> increases with the decrease of number of carbon atoms in the aliphatic tertiary amine chain (Fig. 3). In the case of a 1:1 molar ratio of reactants, for trioctylamine, an efficiency equal to zero was observed, while the use of tripropylamine allows to achieve an efficiency of 24.86%. The process efficiency obtained by the use of tripropylamine is 2-fold higher than in the case of trioctylamine, while maintaining a 4:1 molar ratio of the reactants.

The aim of the second part of the performed experiments was to investigate the effect of the mixing rate on the course of the process. The obtained results are shown in Fig. 4 and Fig. 5. In Fig. 4, the change of concentration of acid in the aqueous phase after the process versus the time is presented. In Fig. 5, the efficiency of the process versus the time is shown. The experiments have been performed at stirrer speeds of 250, 350 and 500 rpm.

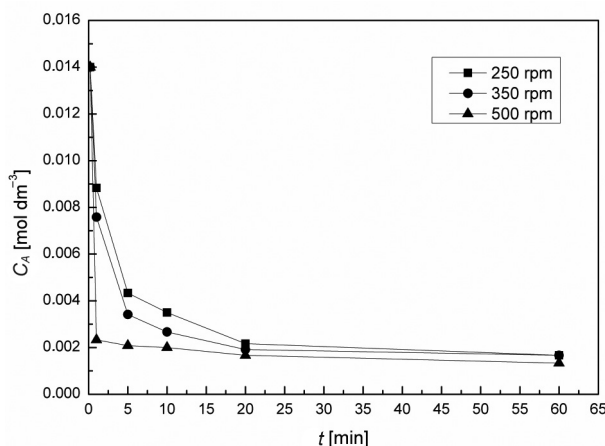


Fig. 4. Effect of stirrer speed on the concentration of citric acid in the aqueous phase versus the time (16 MPa, 308 K,  $C_{A0} = 0.014 \text{ mol dm}^{-3}$ ,  $C_{TPA} = 0.056 \text{ mol dm}^{-3}$ )

As shown in Fig. 4, an increase of the stirrer speed increases the reactive extraction process rate. A positive effect of the high mixing rates on the course of the reactive extraction process is clearly observed in the case of stirrer speeds of 250, 350 and 500 rpm. For example, at

500 rpm, the equilibrium concentration of acid in the aqueous phase was achieved already after 20 min. An increase of the stirrer speed leads to an increase of the process rate, so the final efficiency is obtained in a shorter period of time (Fig. 5). An increase in the stirrer speed leads to an increase of dispersion of the heterogeneous mixture and to a reduction of the mass transfer resistance between the phases of the system, which contributes to an increase of the process efficiency. The application of a stirrer speed of 500 rpm allows for an efficiency of 83.72% after 1 min, while the use of 250 rpm and 350 rpm results in an efficiency of 38.37% and 47.09%, respectively. This effect demonstrates the very fast reaction of acid-amine complex formation and mass transfer in a heterogeneous system.

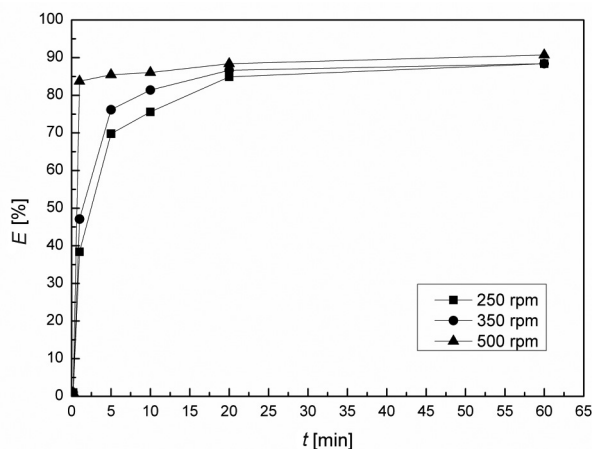


Fig. 5. Effect of stirrer speed on the efficiency of citric acid reactive extraction versus the time (16 MPa, 308 K,  $C_{A0} = 0.014 \text{ mol dm}^{-3}$ ,  $C_{TPA} = 0.056 \text{ mol dm}^{-3}$ )

## 5. Conclusions

The obtained results indicate the legitimacy of the application of supercritical  $\text{CO}_2$  in the reactive extraction process in order to recover citric acid from an aqueous solution. The supercritical reactive extraction process of carboxylic acid can be controlled by changing the type of tertiary amine, the molar ratio of reactants, and the mixing rate in the system. A concentration of amine that is higher than the concentration of acid, and a decrease of the tertiary amine chain length, result in the highest efficiency of the reactive extraction of citric acid from an aqueous solution. More intensive mixing intensifies the process and increases its final efficiency in a shorter period of time. For a high stirrer speed, the reactive extraction process is controlled by kinetics of the reaction of complex formation.

In the batch mode, the efficiency of the considered process is limited by the solubility of the reactant forming a complex with an acid in supercritical  $\text{CO}_2$ . Therefore, the obtained efficiencies of the process performed for higher acid concentrations could be relatively low. An increase of the process efficiency can be achieved by the application of a continuous system, in which the flow of supercritical  $\text{CO}_2$  is saturated with an extractant.

*This project was funded by the National Science Centre (Poland) granted on the basis of decision no. DEC-2013/09/N/ST8/04336.*

## References

- [1] Kurzrock T., Weuster-Botz D., *Recovery of succinic acid from fermentation broth*, Biotechnology Letters, Vol. 32, 2010, 269–282.
- [2] Kapucu N., Guvenc A., Mehmetoglu U., Calimli A., *Reactive extraction of organic acids by supercritical CO<sub>2</sub>*, Reviews in Chemical Engineering, Vol. 15, 1999, 233–243.
- [3] Kertes A.S., King C.J., *Extraction chemistry of fermentation product carboxylic acids*, Biotechnology and Bioengineering, Vol. 28, 1986, 269–282.
- [4] Ricker N.L., Pitman E.F., King C.J., *Solvent extraction with amines for recovery of acetic acid from dilute aqueous industrial streams*, Journal of Separation Process Technology, Vol. 1(2), 1980, 23–30.
- [5] Hampe E.M., Rudkevich D.M., *Exploring reversible reactions between CO<sub>2</sub> and amines*, Tetrahedron, Vol. 59, 2003, 9619–9625.
- [6] Poposka F.A., Nikolovski K., Tomovska R., *Kinetics, mechanism and mathematical modeling of extraction of citric acid with isodecanol/n-paraffins solutions of trioctylamine*, Chemical Engineering Science, Vol. 53, 1998, 3227–3237.
- [7] Tamada J.A., King C.J., *Extraction of carboxylic acids with amine extractants. 2. Chemical interactions and interpretation of data*, Industrial and Engineering Chemistry Research, Vol. 29, 1990, 1327–1333.
- [8] Hong Y.K., Hong W.H., *Influence of chain length of tertiary amines on extractability and chemical interactions in reactive extraction of succinic acid*, Korean Journal of Chemical Engineering, Vol. 21, 2004, 488–493.
- [9] Djas M., Henczka M., *Badania przebiegu procesu reaktywnej ekstrakcji kwasów karboksylowych*, III Ogólnopolskie Sympozjum „Reaktory Wielofazowe i Wielofunkcyjne dla Procesów Chemicznych i Ochrony Środowiska”, Warsaw–Serock, 10–12 October 2012, 47–52.

KATARZYNA Z. GACA\*

## A REVIEW: THE INFLUENCE OF THE CATALYST ON FORMATION AND PROPERTIES OF RESORCINOL- -FORMALDEHYDE GELS

### PRZEGLĄD: WPŁYW KATALIZATORA NA POWSTAWANIE ORAZ WŁAŚCIWOŚCI ŻELI REZORCYNOWO- -FORMALDEHYDOWYCH

#### Abstract

The paper summarises the findings of the most significant studies on the effect that the catalyst has on the formation and properties of organic gels, synthesised *via* the sol-gel method from resorcinol and formaldehyde. These materials exhibit excellent electrical and mechanical properties, as well as have great specific surface areas, and thus are excellent materials for manufacturing electrodes in a variety of appliances, from rechargeable batteries to supercapacitors. The properties of these gels can be adjusted to meet the desired values, however, they are controlled by a number of factors. The most interesting of these is the catalyst and its role, as it is elusive and has been investigated only by several authors across the globe.

*Keywords: organic gels, organic aerogels, catalyst, formaldehyde, resorcinol*

#### Streszczenie

W artykule streszczono wyniki najistotniejszych prac naukowych poświęconych wpływowi katalizatora na powstawanie oraz właściwości końcowe żeli organicznych, otrzymywanych metodą zol-żelową z rezorcyny i formaldehydu. Materiały te posiadają doskonale właściwości elektryczne i mechaniczne, a także posiadają duże wartości powierzchni właściwych, przez co są doskonałymi materiałami do produkcji elektrod w różnych urządzeniach, począwszy od akumulatorów aż po superkondensatory. Właściwości tych żeli mogą być dostosowane do oczekiwanych wartości, jednakże są one też kontrolowane przez wiele czynników. Najbardziej interesującym z nich jest katalizator oraz jego rola, ponieważ jest ona niejasna i była zbadana zaledwie przez kilkoro naukowców na świecie.

*Słowa kluczowe: żele organiczne, aerożele organiczne, katalizator, formaldehyd, rezorcyna*

\* Ph.D. Katarzyna Z. Gaca, Department of Chemistry and Technology of Polymers, Faculty of Chemical Engineering and Technology, Cracow University of Technology.

## 1. Introduction

Organic aerogels were first synthesised using the sol-gel technology by R. W. Pekala in 1989, at the Lawrence Livermore National Laboratories in the USA [1]. Since then, they have gained international interest and became the focus of research in the broad field of energy-related materials. The precursors of these materials are organic wet gels, synthesised in aqueous solutions of resorcinol and formaldehyde, in the presence of a basic catalyst, such as sodium carbonate, sodium and potassium hydroxides. The reaction follows a general path shown in Fig. 1.

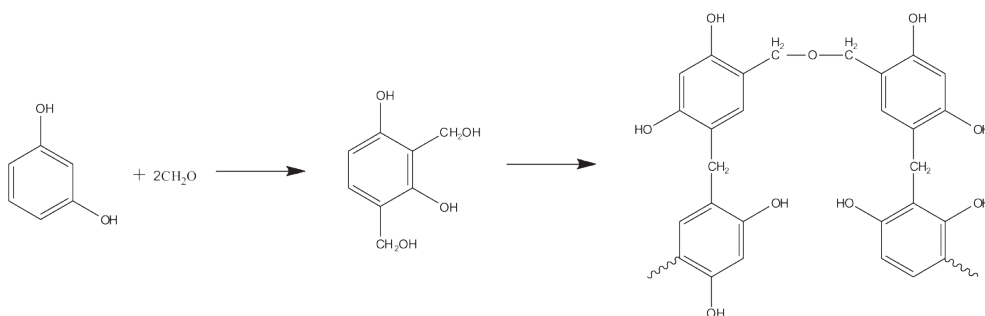


Fig. 1. Overall path of resorcinol and formaldehyde reactions in aqueous solutions, leading to the formation of resorcinol-formaldehyde gels

These aerogels are characterised by very high porosity, and thus high surface area, reaching several hundreds of square metres per gram. Their most interesting feature is their excellent electrical properties, such as capacity and conductivity. Owing to these properties, they are ideal materials for the construction of electrodes in a variety of appliances, such as batteries, rechargeable batteries and supercapacitors [2–4].

The sol-gel process, in which their precursors are obtained, is controlled by a number of factors, such as temperature, concentration of reagents – both total and relative – and concentration of catalyst and its type. It is also probable that the duration of the process and stirring also have an effect on the physical mechanism of the gel synthesis, and thus the final properties of the resulting gel.

## 2. Influence of the initial pH on the properties of the resulting gel

Several key issues need to be taken into account when investigating the influence of the catalyst on the porous properties of an organic gel. The main role of the catalyst, in this particular case, is providing the most favourable conditions for the reaction between resorcinol and formaldehyde. In practice, this means adjusting the pH to the desired level, and thus enabling the reaction. Later on, the chosen pH value can affect the whole process. The catalyst type needs to be chosen appropriately, along with its concentration.

The most commonly used catalysts chosen for the synthesis of resorcinol-formaldehyde gels are those, which provide an alkaline solution upon dissolution in water. The very first studies [1] proved that the gels, with arbitrarily named best properties, are those synthesised at pH above 6.0, however, the study did not cover solutions with initial pH values above 7.5. Some of the later studies [5, 6] also did not include these, however, a couple of studies [7, 8] also included experiments in which the initial pH was as high as 9.0. The overall conclusions drawn from these studies were that gels could not be obtained from solutions with an initial pH below 6.0, and instead, the solutions became opaque or a precipitate formed after heating. Interestingly, when the initial pH was above 8.0, the gel also did not form according to one study [7] or it contained virtually no pores, according to another study [8]. Research carried out by Lin et al. [5] proved that carbon xerogels synthesised with an initial pH in the range of 7.0–7.5, and were virtually solid with no pores. Only when the pH was decreased by the addition of nitric acid, both the pore volume and the surface area increased, which is natural as these are related to each other. The most significant increase, from 0 to  $600 \text{ m}^2 \cdot \text{g}^{-1}$ , was observed for samples with the initial pH decreased with addition of nitric acid, from 7.0 to 6.5. Moreover, the results of this study have shown that the pore volume increased linearly with the decrease of pH in the range of 7.0–5.7. Moreover, findings of Lin et al. [5] also included the fact that the lower the initial pH, the broader the pore size distribution, therefore, a more uniform structure could be obtained from solutions with pH closer to 7.0. Results of Zanto et al. [9] appear to confirm these findings, underlining that the most significant factor affecting the surface area and pore volume is the initial pH, and not the weight percentage of solids, a measure chosen by some as a factor determining the final properties of gel. Nevertheless, it is worth reminding that the pH is strictly connected to the concentration of the catalyst, which is typically added at a given molar ratio to resorcinol, which is in turn at a fixed molar ratio with formaldehyde.

Research done by Job et al. [6] confirmed an assumption arising from previous literature that the specific surface area can be adjusted by varying the initial pH value. An increase of pH from 5.45 to 7.35 caused the specific surface area to increase from  $330 \text{ m}^2 \cdot \text{g}^{-1}$  to  $470 \text{ m}^2 \cdot \text{g}^{-1}$ , however, a maximum of  $510 \text{ m}^2 \cdot \text{g}^{-1}$  was found at pH equal to 6.50. Therefore, this study confirms that the relationship between the initial pH and the surface area is not linear in the range of 5.45 to 7.35. Similarly, a more recent study by Zubizarreta et al. [8] focused on the influence of the initial pH on the surface area of resorcinol-formaldehyde gels. The main conclusion arising from this paper is that the highest surface area can be achieved when the initial pH was between 6 and 7, and that it is much higher than of those synthesised at pH equal to 9.

Several researchers [10, 11] investigated the use of acidifying agents (acetic acid) as catalysts. These studies successfully covered pH range lower than 5.0 and proved that gels can also be formed in such conditions. Nevertheless, their porous properties are different than of those synthesised using basic catalysts. Moreover, they strongly depend on the chosen resorcinol to catalyst molar ratio (R/C). For instance, only a very weak relationship between the pore size and the R/C ratio was found, while for basic-catalysed gels this relationship is strong. Nevertheless, at very high R/C ratios (above 1000), both acid- and base-catalysed resorcinol-formaldehyde gels have almost the same properties, as far as electrical conductivity, elastic moduli, micropore size and volume are concerned [11].

### 3. Influence of the catalyst type on the properties of the resulting gel

As it appears from the published results of numerous studies, not only the pH of the initial solution influences the properties of the resulting material, but also the chemical compound used as a catalyst. The most often chosen catalysts are alkaline because the preferred reaction conditions are mildly basic, while both resorcinol and formaldehyde produce an acidic environment upon dissolution in water. Most researchers use the same catalyst as Pekala did in 1989 and afterwards [1, 12, 13], i.e. sodium carbonate. This compound does not cause difficulties in handling and storing, it is relatively safe, easily available and inexpensive, hence its popularity [2, 14–19]. Nonetheless, other basifying agents were investigated, such as sodium and potassium hydrogencarbonates [20, 21] and potassium carbonate [21, 22]. Alkaline hydroxides are also popular with researchers – hydroxides of sodium, potassium, lithium, calcium, barium, magnesium and strontium were extensively studied [20, 23]. The prevailing hypothesis states that the primary role of the catalyst is to provide an appropriate pH, therefore, even ammonia was studied as a potential catalyst [20], however, with little success. Tamon et al. [20] proved that the alkaline metal cation is necessary for the synthesis and gel formation, as ammonia failed to successfully catalyse the reaction.

Fairen-Jimenez et al. [22] found that for the same concentration of the reactants, i.e. formaldehyde and resorcinol, gels produced with sodium carbonate were denser than those synthesised with potassium carbonate as the catalyst. They also had smaller a pore volume and smaller pore diameters. This study was followed by a far more extensive one by Job et al. [23], in which alkali metal hydroxides and alkali earth metal hydroxides were examined, leading to a conclusion on the influence of the type of metal on the synthesis process. The results showed that the size of the metal cation does not influence the pore characteristics of the resulting gel, however, its charge and concentration do. Alkali earth metals (charge +2) led to gels with larger pore sizes than those synthesised in the presence of alkali metals (charge +1). The initial pH was kept constant, meaning that the concentration of alkali metal hydroxides was roughly twice the concentration of alkali earth metal hydroxides. The explanation for this effect provided by Job et al. binds the effect of ions on the pore structure with electrostatic effects on the microphase separation process prior to the gelation. It is known that salts destabilise colloidal suspensions and may lead to their coagulation and Job et al. claim that this is what controls the gelation step. The repulsion between colloidal particles

is screened over the Debye–Hückel distance, which is inversely proportional to  $\sqrt{\sum nq^2}$ ,

where  $n$  is the concentration of ions and  $q$  is their charge. Therefore, earth metal cations with a +2 charge are more effective in screening these repulsive forces, leading to a destabilisation of the suspension and gel formation at an earlier stage of the reaction. As a consequence, the obtained gels have larger pores, even when the same initial pH was provided.

Findings of Job et al. [23] were mostly in agreement with findings of a more recent study by Morales-Torres et al. [16], in which five alkali carbonates were used as catalysts (Li, Na, K, Rb, Cs). The results showed a relationship between the size of the counter-ion and the gelation time. Moreover, the slower the gelation, the larger the primary particles, therefore, also larger pores. In their study, Morales-Torres et al. suggest that the growth of the resorcinol- formaldehyde gels takes place via the formation of anionic species induced

by the catalyst. Therefore, electrostatic interactions are present, and thus it might be worth to consider the application of surfactants in order to provide a better control over the process.

A study on acid-catalysed sol-gel process of resorcinol-formaldehyde gels synthesis in aqueous solutions was done by Brandt et al. [11]. The study observed that the greater the concentration of the catalyst – acetic acid – the smaller the particles that form the gel network. At the same time, the dependence of the pore sizes of the gel on the R/C ratio is much weaker than for gels synthesised using basic agents, as it was previously mentioned in this paper.

Mulik et al. [10] performed a study in which resorcinol-formaldehyde gels were synthesised using hydrochloric acid as catalyst and acetonitrile as solvent. Even though two factors were altered – solvent type and catalyst – the results showed that these gels were virtually indistinguishable by IR and  $^{13}\text{C}$  CP/MAS NMR from the base-catalysed materials. Mulik et al. reason that the acid-catalysed route to gel formation is acceleration of the reaction *via* increasing the positive charge of the electrophile rather than the activation of the aromatic ring by enhancing the ability to donate electrons of the substituents (OH to O-), as it is in case of the base-catalysed synthesis. On the other hand, results provided by Fairen-Jimenez et al. [22], before Mulik et al. study, proved that the acidic catalyst affected only the gelation process. This study [22] also proved that when using acidic catalyst, oxalic acid or para-toluenesulfonic acid, the density of the resulting material is greater than in the case of alkaline carbonate catalysts by a factor of two or even three, suggesting that the use of acidic catalyst greatly enhances cross-linking and condensation.

A number of studies revealed a dependence of the porous properties of the resorcinol-formaldehyde gels on the concentration of the catalyst. In most cases, the catalyst influence is examined not as an absolute concentration, but as a relative measure – the resorcinol-to-catalyst molar ratio.

There is a large number of studies, which handle the effect of the R/C ratio on the properties of the final material, but they are mostly consistent in their findings. A study performed by Saliger et al. [24] showed that the growth of particles forming the gel could be controlled by the concentration of the catalyst, appropriate concentration of the reactants and the temperature. The amount of catalyst was claimed to control the size of the particles constituting the gel network, under the assumption that more catalyst translates into more numerous active sites in which these particles are formed, leading to structures with smaller particles, and thus pores. Interestingly, Saliger et al. managed to obtain materials with cluster sizes in the  $\mu\text{m}$  range, while typically, particles of a nanometre scale are observed. Findings of Saliger et al. were confirmed by findings of Bock et al. [25], who found that for lower R/C ratios (i.e. higher catalyst concentrations), the gel structures were finer, which corresponds to smaller primary particles.

A review by Al-Muhtaseb et al. [3] summarises some research findings on the resorcinol-formaldehyde gels. The overall conclusion is that the structure of gels synthesised in the presence of a low concentration of catalyst (i.e. high R/C ratio) resembles “string-of-pearls”. This means that there is a number of rather large (16–200 nm in diameter) particles connected with thin strings. This is not the case for materials that are more fibrous in appearance, obtained in conditions of a high catalyst concentration. In that case, the diameter of the particles and the links between them is virtually the same and varies around much smaller values of only 3–5 nm. The reasoning behind this finding is that a lower catalyst concentration allows longer growth of the primary particles prior to gel the formation. As a result, the pore sizes are greater.

A study by Job et al. [6] is in agreement with these findings and attempts to provide an explanation for this phenomenon. When high concentration of catalyst is used, the rate of hydroxymethyl derivatives formation, as well as the extent of substitution, are high. As a result, highly-branched clusters are formed. These structures condense readily, therefore, they do not remain in the nucleation regime for long, and thus, form smaller clusters. When a low concentration of catalyst is used, the effect is contrary: lowly-branched structures are formed and they persist in the nucleation regime for a longer period of time, allowing growth without condensation and gelation.

A significant majority of the available studies focus on the influence of the R/C ratio on the resulting properties of the gel, and not directly on the mechanism itself. Only some attempted at explaining the role of the catalyst by correlating the final properties with the reaction conditions. Nevertheless, a direct observation would be far more valuable. There is a very limited number of such studies using Dynamic Light Scattering (DLS) to examine the changes caused by altering the R/C ratio, or the catalyst type, on the gelation mechanism. One of the studies was done by Berthon et al. [15], who mostly studied the influence of the solvent and the type of catalyst on the gels. While the authors dedicated a significant amount of research to the non-aqueous reacting solutions, only one R/C ratio of aqueous solution was investigated. Nonetheless, the study suggested that the mechanism of gel formation is different for acid and base-catalysed syntheses. A far more relevant study was conducted by Yamamoto et al. [17], in which DLS experiments were carried out on samples with a varying catalyst (sodium carbonate) and resorcinol concentrations. The main findings of this study are that the growth rate of the primary particles depends on the catalyst and resorcinol concentrations. Moreover, this relationship is not linear throughout the whole synthesis process. Yamamoto et al. [17] also found that as the reaction reaches approximate gelation time, the shape of the decay time spectrum becomes bimodal, indicating the formation of a less-mobile structure, probably the gel network. The most recent study by Gaca et al. [18] employed DLS to examine the influence of the R/C ratio on the growth rate of primary particles, namely agglomerates of hydroxymethyl resorcinol derivatives, at two different temperatures. The results indicated that the size of primary clusters forming the gel network appears to be thermodynamically controlled and the miscibility limit is reached upon the formation of reaction intermediates, which most likely are relatively small. This results in nanoscale molecular demixing, leading to the formation of monodisperse primary clusters. At higher catalyst or reactant concentrations, more numerous primary clusters are produced due to faster reactions. Authors believe that the primary clusters may be initially liquid-like, and further polymerisation may proceed faster within them than in the bulk solution due to locally higher concentrations of intermediates. The overall conclusion of these papers is that the process appears to be far more complex than previously assumed.

#### 4. Conclusions

As numerous studies have shown, the catalyst plays a decisive role in the synthesis of resorcinol-formaldehyde gels. Its role is complex and appears to be of both physical and chemical nature. Not only does its concentration has an effect, but also its type. Moreover, its influence can be synergistic with other factors, such as concentration of the reactants.

The effect of the R/C ratio on the surface area is significant, however, it varies across studies. In many cases, a maximum value was found for certain conditions and it appears that more factors than just R/C ratio determined this. It also seems that the pH is a more influential factor than the R/C ratio, though these two are connected.

A lack of thorough studies on the influence of the catalyst, its type and concentration is seen in the literature. Only a couple of papers cover this matter, while it appears to be crucial in determining the actual role played by the catalyst in the sol-gel process.

## References

- [1] Pekala R.W., Mater J., Sci. 24, 1989, 3221.
- [2] Hall P.J., Mirzaeian M.P.J., Fletcher S.I., Sillars F.B., Rennie A.J.R., Shitta-Bey G.O., Wilson G., Cruden A., Carter R., Energy Environ. Sci. 3, 2010, 1238.
- [3] Al-Muhtaseb S.A., Ritter J.A., Adv. Mater. 15, 2003, 101.
- [4] Tashima D., Yamamoto E., Ka N., Fujikawa D., Sakai G., Otsubo M., Kijima T., Carbon N. Y. 49, 2011, 4848.
- [5] Lin C., Ritter J. A., Carbon N.Y. 35, 1997, 1271.
- [6] Job N., Pirard R., Marien J., Pirard J.-P, Carbon N.Y. 42, 2004, 619.
- [7] Feng Y.N., Miao L., Tanemura M., Tanemura S., Suzuki K., Mater. Sci. Eng. B 148, 2008, 273.
- [8] Zubizarreta L., Arenillas A., Domínguez A., Menéndez J.A., Pis, J.J., Non J., Cryst. Solids 354, 2008, 817.
- [9] Zanto E.J., S.A. Al-Muhtaseb S.A., Ritter J.A., Ind. Eng. Chem. Res. 41, 2002, 3151.
- [10] Mulik S., Sotiriou-Leventis C., Leventis N., 2007, 6138.
- [11] Brandt R., Petricevic R., Probstle H., Fricke J., J. Porous Mater. 10, 2003, 171.
- [12] Fung A.W.P., Reynolds G.A.M., Wang Z.H., Dresselhaus M.S., Dresselhaus G., Pekala R.W., 186, 1995, 200.
- [13] Pekala R.W., Farmer J.C., Alviso C.T., Tran T.D., Mayer S.T., Miller J.M., Dunn B., J. Non. Cryst. Solids 225, 1998, 74.
- [14] Petričević R., Reichenauer G., Bock V., Emmerling A., Fricke J., J. Non. Cryst. Solids 225, 1998, 41.
- [15] Berthon S., Barbieri O., Ehrburger-Dolle F., Geissler E., Achard P., Bley F., Hecht A.M., Livet F., Pajonk G.M., Pinto N., Rigacci A., Rochas C., J. Non. Cryst. Solids 285, 2001, 154.
- [16] Morales-Torres S., Maldonado-Hódar F.J., Pérez-Cadenas A.F., Carrasco-Marín F., Phys. Chem. Chem. Phys. 12, 2010, 10365.
- [17] Yamamoto T., Yoshida T., Suzuki T., Mukai S.R., Tamon H., J. Colloid Interface Sci. 245, 2002, 391.
- [18] Gaca K.Z., Sefcik J., J. Colloid Interface Sci. 406, 2013, 51.
- [19] Mirzaeian M., Hall P.J., J. Mater. Sci. 44, 2009, 2705.
- [20] Tamon H., Ishizaka H., J. Colloid Interface Sci. 223, 2000, 305.
- [21] Horikawa T., Hayashi J., Muroyama K., Carbon N.Y., 42, 2004, 1625.

- [22] Fairén-Jiménez D., Carrasco-Marín F., Moreno-Castilla C., Carbon N.Y., 44, 2006, 2301.
- [23] Job N., Gommès C.J., Pirard R., Pirard J.P., J. Non. Cryst. Solids 354, 2008, 4698.
- [24] Saliger R., Fischer U., Herta C., Fricke J., 1998, 81.
- [25] Bock V., Emmerling A., Fricke J., J. Non. Cryst. Solids 225, 1998, 69.

MONIKA GWADERA, BARBARA LARWA, KRZYSZTOF KUPIEC\*

## MODELLING OF HEAT CONDUCTION IN THE GROUND

## MODELOWANIE PRZEWODZENIA CIEPŁA W GRUNCIE

### Abstract

Simple cases of heat conduction in the ground are presented. Systems without interaction with the ground surface are considered. For heating or cooling of the ground by a flat slab, an analytical solution was used. Heat transfer between the ground and a single pipe and several parallel pipes is also considered. In these cases, a numerical solution was used. The analysed problems are of practical importance for modelling and simulation of ground heat exchangers cooperating with heat pumps.

*Keywords: process modelling, transient heat conduction, renewable energy sources*

### Streszczenie

Przedstawiono proste przypadki przewodzenia ciepła w gruncie. Rozważono układy, w których nie występuje oddziaływanie z powierzchnią gruntu. Do ogrzewania lub chłodzenia gruntu przez dużą płaską płytę zastosowano rozwiązanie analityczne. Rozważono również przenoszenie ciepła pomiędzy pojedynczą rurą oraz kilkoma równoległe ułożonymi rurami a gruntem. W tych przypadkach zastosowano rozwiązania numeryczne. Analizowane problemy mają praktyczne znaczenie przy modelowaniu i symulacji gruntowych wymienników ciepła sprzężonych z pompami ciepła.

*Słowa kluczowe: modelowanie procesów, niustalone przewodzenie ciepła, odnawialne źródła energii*

\* Ph.D. Eng. Monika Gwadera, Ph.D. Eng. Barbara Larwa, Prof. Ph.D. D.Sc. Eng. Krzysztof Kupiec, Chair of Chemical and Process Engineering, Faculty of Chemical Engineering and Technology, Cracow University of Technology.

## 1. Introduction

Heat transfer from horizontal pipes located in the ground has been studied for many years because of widespread applications of such systems. They are used in industrial pipelines, district heating, buried power cables, and also in earth tube heat exchangers and ground source heat pumps [1, 2, 3]. Studies on ground thermal behaviour showed that the effect of geothermal heat transferred to the ground from the centre of the Earth on ground thermal behaviour can be ignored, when compared to the solar effect on the ground surface. Therefore, ground-coupled heat pumps use the ground as a solar collector during the heating season and as heat storage during the cooling season.

Heat transfer in the ground, with a heat exchanger installed in it, is a complex process; modelling and designing of the process requires many simplifying assumptions. All models are based on equations of transient heat conduction [4]. The differences lie in the adaptation of a one-, two- or three-dimensional model and the application of different boundary conditions and the initial condition. In some cases, model equations can be solved analytically.

In this work, some simple cases referring to heat conduction in the ground are presented. They are of practical importance for modelling and simulation of ground heat exchangers cooperating with heat pumps. Systems without interaction with the ground are considered. For one-dimensional systems, analytical solutions are known. For a two-dimensional system, a numerical procedure was used.

## 2. The solution for a semi-infinite body

Heating or cooling of the ground by a slab of large dimensions and a constant temperature is the simplest case. When a slab with a uniform and constant temperature  $T_0$  is located in the ground at a temperature  $T_i$ , then the heat transfer occurs perpendicularly to the slab surface. Heat conduction is one-dimensional. In this simple case of transient heat conduction in a semi-infinite body, the temperature of the ground is a function of the distance from the slab surface  $x$  and time  $t$ . The process is described by the equation:

$$\frac{\partial T}{\partial t} = a \frac{\partial^2 T}{\partial x^2} \quad (1)$$

The initial condition is as follows:

$$t = 0 \quad T = T_i \quad (2)$$

The first boundary condition refers to the surface of the slab:

$$x = 0 \quad T = T_0 \quad (3)$$

The second boundary condition refers to the place suitably distant from the slab surface, which ensures temperature constancy:

$$x \rightarrow \infty \quad T = T_i \quad (4)$$

For initially homogeneous temperature of the ground, the temperature dependence on the position and time is described by the relationship [5–8]:

$$\frac{T - T_0}{T_i - T_0} = \operatorname{erf}\left(\frac{x}{2\sqrt{at}}\right) \quad (5)$$

Short process times, i.e. these for which there is no interaction with the ground surface, have been considered. For calculations of ground temperature changes, the data shown in Table 1 were used.

Table 1  
Calculations data

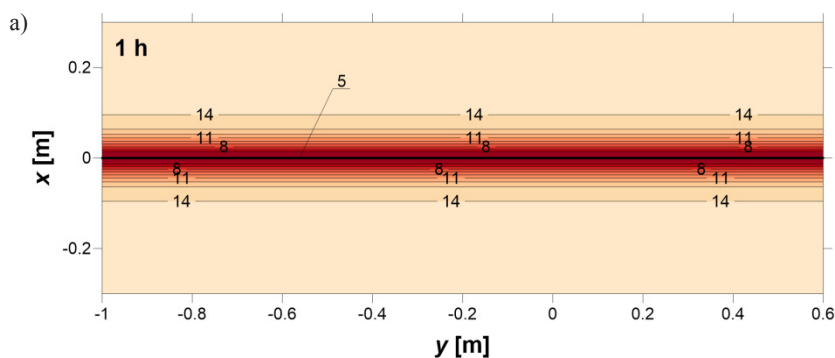
Quantity	Value
Initial temperature of the ground $T_i$	15 [°C]
Slab temperature $T_0$	5 [°C]
Ground thermal conductivity $k$	0.9 [W/(mK)]
Ground density $\rho$	2600 [kg/m <sup>3</sup> ]
Ground heat capacity $c$	900 [J/(kg·K)]

It can be concluded from Table 1 that the slab causes the ground to cool down. The heat transfer occurs symmetrically through the axis of the slab.

The coefficient of thermal diffusivity of the ground is  $a = k/(c\rho) = 0.384 \cdot 10^{-6} \text{ m}^2/\text{s}$ , which follows from the values presented in Table 1.

The calculation results are shown in Figs. 1a, b and c. Lines of constant temperature (contour lines) for different process times are presented.

The longer the process time, the greater the thermal effect of the slab installed in the ground. For example, after 1 h, an approx. 0.1 m thick ground layer (measured unilaterally) cools down to the temperature of 14°C or less. After 3 h, the thickness of this layer increases to approx. 0.15 m, and after 5 h – to 0.2 m.



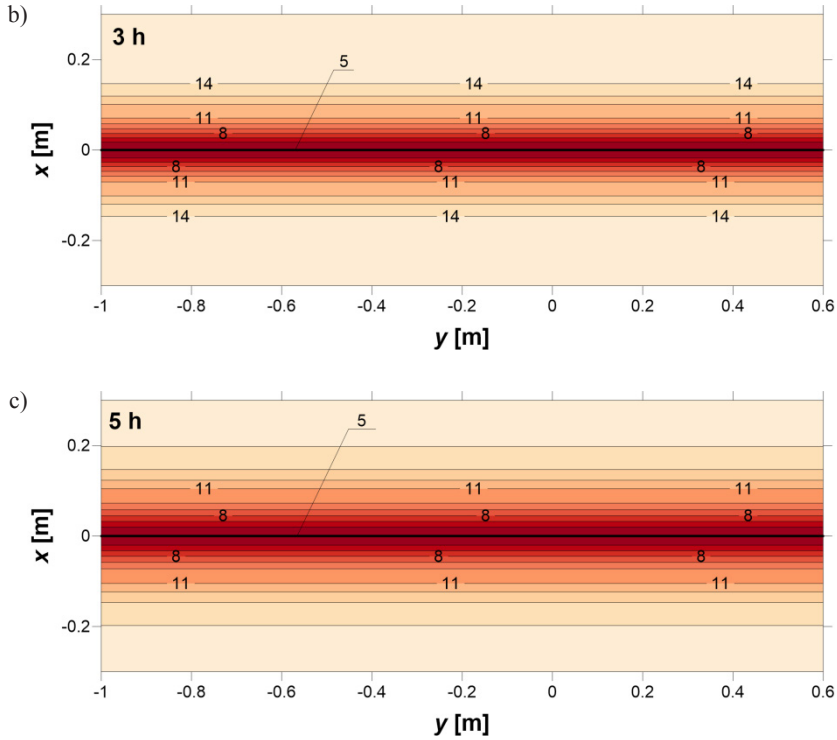


Fig. 1a, b, c. Cooling down of the ground by a slab at a constant temperature

### 3. The solution for an infinite plate

When the time of heating or cooling of a semi-infinite body (ground) by a flat slab is relatively short, the depth of heat penetration in the ground is limited, and for an analysis of the problem presented in the previous chapter, the ground can be treated as a plate of a finite thickness. The differences between the interpretation of position variables  $x$  and  $z$ , in both cases, are presented in Fig. 2. For an infinite plate, the following equation is valid:

$$\frac{\partial T}{\partial t} = a \frac{\partial^2 T}{\partial z^2} \quad (6)$$

The initial condition (2) and the following boundary conditions were used:

$$z = s \quad T = T_0 \quad (7)$$

$$z = 0 \quad \frac{\partial T}{\partial z} = 0 \quad (8)$$

where  $s$  is half of the plate thickness. The solution has the form [5–8]:

$$\frac{T - T_0}{T_i - T_0} = \frac{4}{\pi} \sum_{i=1}^{\infty} \frac{(-1)^{i+1}}{2i-1} \exp \left[ -(2i-1)^2 \left( \frac{\pi}{2} \right)^2 \frac{at}{s^2} \right] \cdot \cos \left( \pi \frac{z}{s} \frac{2i-1}{2} \right) \quad (9)$$

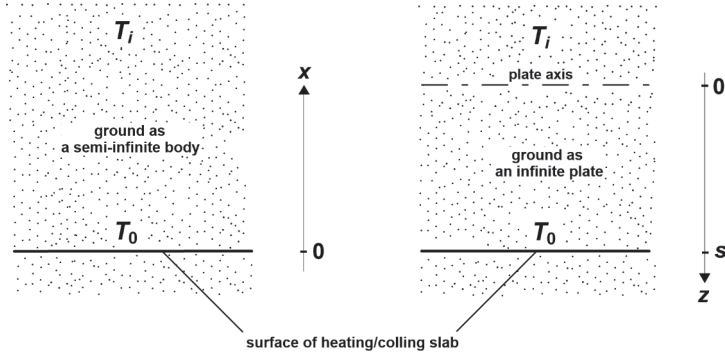


Fig. 2. Symbols for a semi-infinite body and an infinite plate

In Fig. 3, the comparison of temperature profiles obtained from Eqs. (5) and (9) for different process times is presented. In calculations, it was assumed that  $s = 0.2$  m. When interpreting the graph, one must take into account that the symbols for the position coordinate are different for a semi-infinite body ( $x$ ) and an infinite plate ( $z$ ). For conditions under which the simulation was conducted, after 1 hour, there are no differences in heat transfer in the semi-infinite body and the plate. After 3 hours, some differences in the profiles occur. After 5 hours, these differences are large, especially near the axis of the plate. The differences in temperature profiles for the semi-infinite body and the plate are not important when the temperature front is close to the surface of the plate, i.e. when temperature changes have not reached (yet) the centre of the plate.

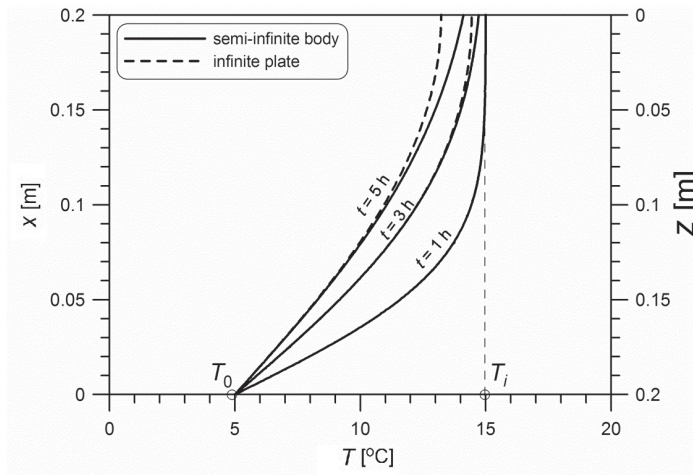


Fig. 3. Comparison of temperature profiles for a semi-infinite body and an infinite plate

#### 4. The solution for an infinite cylinder

A horizontal ground heat exchanger is comprised of a system of pipes with a working liquid flowing inside. When straight pipes are used, they are arranged at some distances from each other. It was assumed that, at the beginning, the ground temperature is uniform. At the beginning of ground cooling (heating), the process can be considered separately for each pipe. The assumption that the temperature of the external surface of a pipe does not change with the time and position was taken. In this case, the heat conduction problem can be treated as one-dimensional. Conduction occurs in a layer of the ground, whose cross-section is shown in Fig. 4.

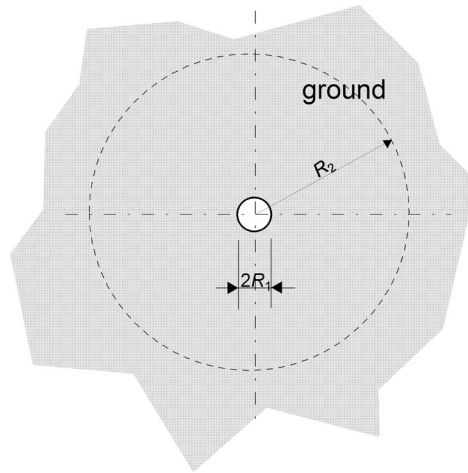


Fig. 4. Heat transfer between the ground and pipe surface

$R_1$  is the radius of the pipe, which is surrounded by the ground.  $R_2$  is any radius ( $R_2 > R_1$ ) for which it can be assumed that temperature does not change. Therefore, the longer the process time, the larger  $R_2$  must be taken for calculations.

The equation of heat conduction in an infinite cylinder has the form:

$$\frac{\partial T}{\partial t} = a \left( \frac{\partial^2 T}{\partial r^2} + \frac{1}{r} \frac{\partial T}{\partial r} \right) \quad (10)$$

Relationship (2) was taken as the initial condition, while the boundary conditions have the form:

$$r = R_1 \quad T = T_0 \quad (11)$$

$$r = R_2 \quad T = T_i \quad (12)$$

where  $r$  is a radial position coordinate ( $R_1 < r < R_2$ ).

In Fig. 5, temperature isolines in the ground around the pipe after 1, 3 and 5 hours of the process are presented. Data from Table 1 – pipe radius  $R_1 = 0.019$  m and  $R_2 = 0.5$  m – were taken for calculations. The problem was solved numerically with the use of the Crank-Nicolson scheme.

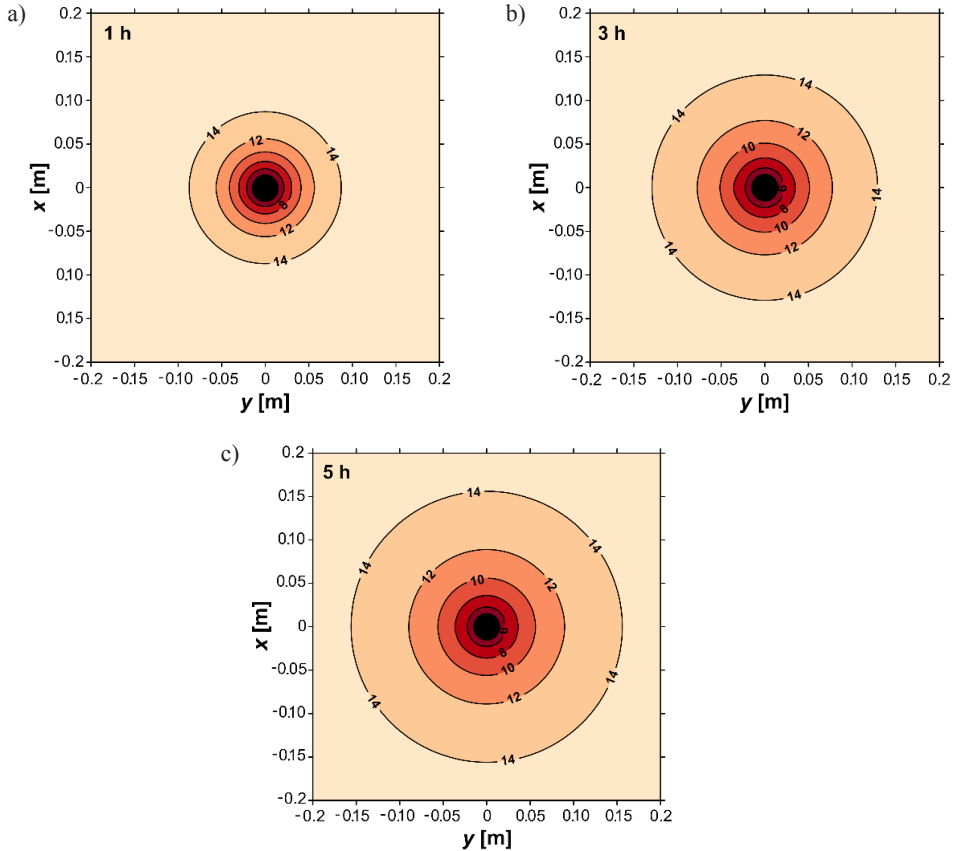


Fig. 5. Maps of temperature isolines in the ground around the pipe with constant surface temperature

As time passes, the ground temperatures decrease because of the relationship  $T_0 < T_r$ . The lowest temperatures are near the pipe surface (pipe cross-section was marked black). After 5 hours, the temperature front does not reach the radius  $R_2$ , so it was right to choose  $R_2 = 0.5$  m for calculations.

## 5. 2D simulation – application of the Peaceman-Rachford procedure

A system with several parallel pipes of a ground heat exchanger is considered below. Except for the initial period, the description of heat conduction requires considering a two-dimensional system. The equation of heat conduction in a two-dimensional system has the form:

$$\frac{\partial T}{\partial t} = a \left( \frac{\partial^2 T}{\partial x^2} + \frac{\partial^2 T}{\partial y^2} \right) \quad (13)$$

In the applied numerical procedure [9], the solution is searched for in a square of a side  $b$  (Fig. 6).

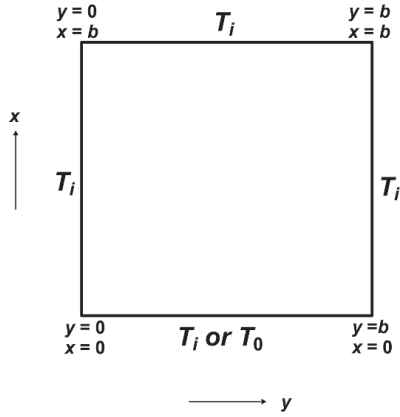


Fig. 6. Interpretation of boundary conditions

The solution has the form of a function of three variables:  $T = T(x, y, t)$ . Values of the temperature at the sides of the square are determined in the boundary conditions. These conditions are as follows:

$$T(x, 0, t) = T_i \quad (14a)$$

$$T(x, b, t) = T_i \quad (14b)$$

$$T(0, y, t) = f(y) \quad (14c)$$

$$T(b, y, t) = T_i \quad (14d)$$

wherein the following equalities referring to temperatures at vertices of the square:

$$f(0) = T(0, 0, t) \quad (15a)$$

$$f(b) = T(0, b, t) \quad (15b)$$

The aim of the calculations is to determine the temporal and spatial distribution of temperatures of the ground at an initial temperature  $T_p$ , which is cooled down by 4 pipes at a 300 mm distance from each other (Fig. 7a). Since the formulation of the boundary conditions for curved surfaces is impossible in the numerical procedure used in this chapter, the real system was substituted by a 'linear' system according to the scheme in Fig. 7b.

The shaded symbols refer to pipe surfaces; in these places, it was assumed, in the boundary conditions, that  $T = T_0$ , and in the others  $T = T_i$ . Data for calculations are shown in Table 1.

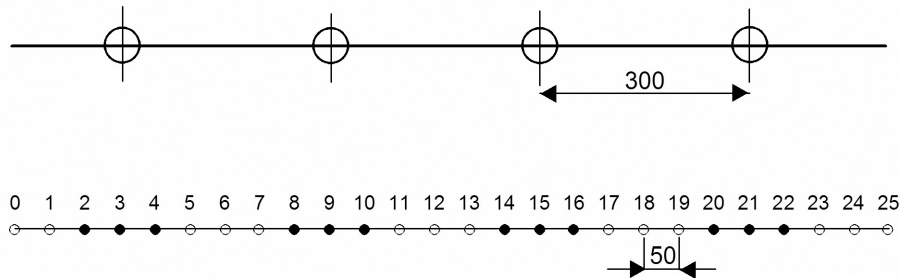
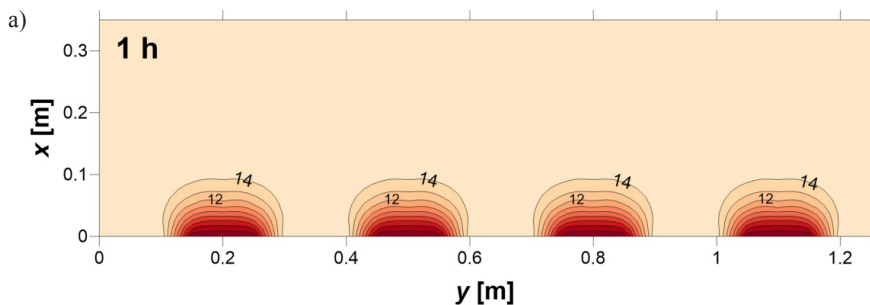


Fig. 7. Explanation of the form of the boundary condition (14c) and function (16)

Function  $f(y)$  in the boundary condition (14c) has the form ( $j$  – node number):

$$f(y) = \begin{cases} T_i & \text{for } j = 0, 1, 5, 6, 7, 11, 12, 13, 17, 18, 19, 23, 24, 25 \\ T_0 & \text{for } j = 2, 3, 4, 8, 9, 10, 14, 15, 16, 20, 21, 22 \end{cases} \quad (16)$$

In order to solve the problem, the Peaceman-Rachford alternating direction implicit (ADI) method was used. The ADI methods are two step methods. In the first step, a tridiagonal system of equation along the lines parallel to the  $x$  axis is solved, while in the second step, an analogical system of equations has to be solved, but along the lines parallel to the  $y$  axis.  $25 \times 25$  nodes were used in numerical calculations. The results of calculations are presented in Figs. 8a, b, c.



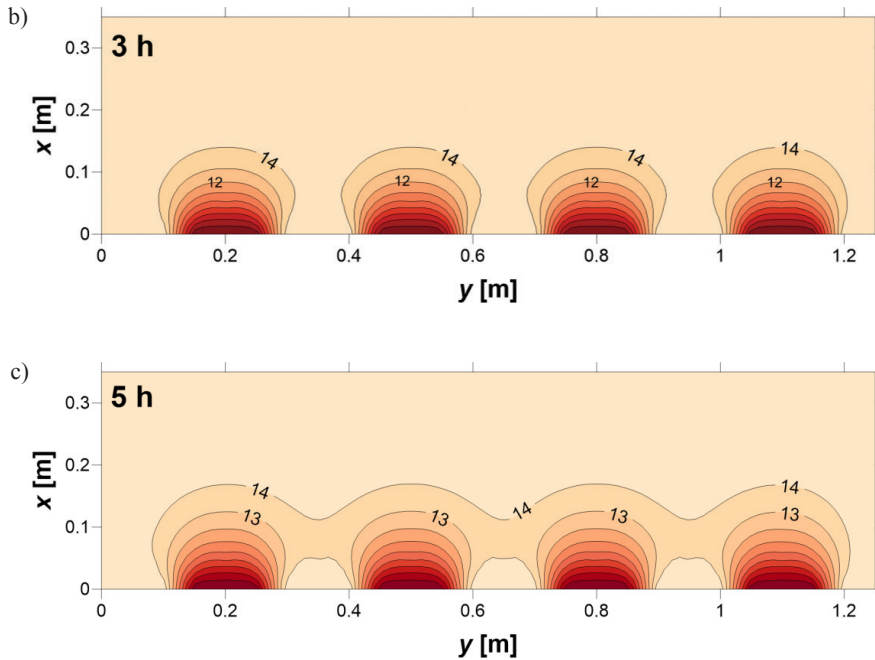


Fig. 8. Results of 2D simulation with the use of the Peaceman-Rachford procedure

The figures refer to the cross-section of the system of pipes. Contour lines for the ground are presented; temperatures are expressed by numbers (in  $^{\circ}\text{C}$ ). Position coordinates in the ground are on the axes. The pipes are far enough from the ground surface to ensure that there is no interaction with the surroundings. As can be seen, at the beginning, each pipe cools the ground individually, independently of the other pipes. However, after some time, temperature fronts connect with each other and an increasing part of the constant temperature line is more and more rectilinear and parallel to the  $y$  axis. Hence, the system behaves similarly as during cooling of the ground by an infinite plate. This similarity becomes greater, the greater the number of pipes and the denser they are arranged.

## 6. Conclusions

- The described models represent simple systems for heating and cooling of the ground. Under real conditions, there are systems that differ in, for example:
  - a) Interactions with the ground surface.
  - b) Periodic work of the heat exchanger.
- For short times of heating/cooling, the ground can be treated as a finite thickness plate (instead of a semi-infinite body). However, for heating/cooling of the ground by a system of parallel pipes, solutions for a single pipe can be used.
- It was noticed for simulation of heat conduction for a system of parallel pipes of a ground heat exchanger that, after some time, the temperature isolines are similar to straight lines.

This gives a basis for using one-dimensional equations of heat conduction for the modeling of horizontal ground heat exchangers.

- The presented calculations can be used as a special case of heat transfer in the ground, which is useful for testing complex models that refer to transient heat conduction in ground heat exchangers.

## References

- [1] Al-Khoury R., *Computational Modeling of Shallow Geothermal Systems*, CRC Press, 2012.
- [2] Rubik M., *Pompy ciepła w systemach geotermii niskotemperaturowej*, Multico Oficyna Wydawnicza, Warszawa 2011.
- [3] Sedova M., Adamovsky R., Neuberger P., *Analysis of ground massif temperatures with horizontal heat exchanger*, Research in Agricultural Engineering, Vol. 59(3), 2013, 91–97.
- [4] Kupiec K., Larwa B., Gwadera M., *Heat transfer in horizontal ground heat exchangers*, Applied Thermal Engineering, Vol. 75, 2015, 270–276.
- [5] Carslaw H.S., Jaeger J.C., *Conduction of heat in solids*, second ed., Clarendon Press, Oxford 1959.
- [6] Crank J., *The Mathematics of diffusion*, Oxford University Press, 1956.
- [7] Cengel Y., Ghajar A., *Heat and mass transfer: fundamentals and applications*, McGraw-Hill, 2010.
- [8] Staniszewski B., *Wymiana ciepła – podstawy teoretyczne*, WNT, Warszawa 1979.
- [9] Marciniak A., Gregulec D., Kaczmarek J., *Basic numerical procedures in Turbo Pascal for your PC*, Nakom, Poznań 1992.



TADEUSZ KOMOROWICZ, KRZYSZTOF NEUPAUER, KATARZYNA SABAT\*,  
ANETA GŁUSZEK\*\*

## LABORATORY TESTS OF PHOTOVOLTAIC MODULES FORMED OF MULTICRYSTALLINE SILICON CELLS

### BADANIA LABORATORYJNE MODUŁÓW FOTOWOLTAICZNYCH ZBUDOWANYCH Z POLIKRYSTALICZNYCH OGNIW KRZEMOWYCH

#### Abstract

The paper presents the results of laboratory tests of both a photovoltaic module formed of 36 multicrystalline silicon cells and a four-module generator, in the form of voltage-current characteristic curves. An analysis of the obtained data is conducted as well.

*Keywords: photovoltaics, multicrystalline silicon cells, voltage-current characteristic curves*

#### Streszczenie

W artykule przedstawiono wyniki badań laboratoryjnych zarówno modułu fotowoltaicznego zbudowanego z 36 polikrystalicznych ogniw krzemowych i czteromodułowego generatora, w formie charakterystyk prądowo-napięciowych. Przeprowadzono również analizę otrzymanych wyników.

*Słowa kluczowe: fotowoltaika, polikrystaliczne ogniwa krzemowe, charakterystyki prądowo-napięciowe*

\* Ph.D. Eng. Tadeusz Komorowicz, Ph.D. Eng. Krzysztof Neupauer, M.Sc. Eng. Katarzyna Sabat, Chair of Chemical and Process Engineering, Faculty of Chemical Engineering and Technology, Cracow University of Technology.

\*\* Ph.D. Eng. Aneta Głuszek, Office of Technical Inspection (UDT) – Warsaw.

## 1. Introduction

According to the “20–20–20 targets” in European Union, by the year 2020, all EU countries should meet at least 20% of their energy needs with renewable energy, the energy efficiency should be improved by 20%, and thereby the reduction of CO<sub>2</sub> emissions, in comparison to the year 1990, should be decreased by 20% [1, 2, 3]. The Sun is a source of energy on the Earth. Radiation power outside the Earth’s atmosphere is equal to 1337 W/m<sup>2</sup> (the solar constant) [4]. Passing through the Earth’s atmosphere, it reduces to 1000 W/m<sup>2</sup>. Photovoltaics, converting solar energy into electric energy, is one of the renewable energy sources.

The basic elements of photovoltaic equipment are photovoltaic cells. The most popular are silicon cells [4]. There are three types of silicon cells:

- monocrystalline,
- poly- or multicrystalline,
- amorphous.

Monocrystalline solar cells, also known as Czochralski or CZ-pulled cells (abbreviation: CZ-Si), are pulled, in a high temperature process, from a crystal (round) and cut into sheets approximately 0.3 mm thick. Pseudo-square wafers are created by sawing the round silicon sheets. The global market share of this type of cells was approximately 30% in 2010 [4]. Monocrystalline silicon cells are the most expensive cells and reach the highest efficiency of about 20%.

Poly- or multicrystalline silicon cells (abbreviation: poly-Si) are poured from a Si melt into a mould. Then, the material is cut from rectangular blocks into 0.3 mm thick wafers. Multicrystalline cells reached a global market share of about 50% in 2010 [4]. The energy expended in the manufacturing process is lower than that of monocrystalline cells. Therefore, the energy payback period is shorter, but the efficiency of cells is lower – about 15%.

Amorphous silicon cells (abbreviation: a-Si) belong to the group of thin film cells. They are produced as a silicon steam precipitate on a glass substrate. The layer thickness does not exceed 0.5 μm. The global market share of amorphous silicon cells was about 5% in 2010 [4]. Less energy is expended when manufacturing them than in the case of monocrystalline cells. The efficiency of amorphous cells ranges from 5 to 10%. The largest surface area, in order to obtain an energy unit, is therefore required compared to other kinds of cells.

The voltage of individual solar cell ranges from 0.5 to 0.6 volt. Therefore, for the standard low voltage range of 6–24 volts, many cells are connected together in series. By doing this, one obtains a solar module or a solar panel that can consist of 12–42 solar cells. When building larger photovoltaic systems (PV systems), many solar modules are connected together in series and in parallel to make a solar generator.

The Chair of Chemical and Process Engineering at the Cracow University of Technology has been involved in the research of renewable energy sources. Photovoltaics is one of their branches. In the Chair, there are laboratory stands for testing modules and generators [5].

The results of laboratory tests of a solar module consisting of 36 multicrystalline silicon cells, and a solar generator formed of four modules combined in series and in parallel, are presented in this paper in the form of current-voltage characteristic curves. An analysis of the obtained data is conducted as well.

## 2. Description of laboratory tests

### 2.1. Description of test stations

The first photovoltaic test station is equipped with a single photovoltaic module (Fig. 1). The second station consists of a set of 4 modules forming a current generator (Fig. 2). All of the modules are identical. Each module consists of 36 multicrystalline rectangular silicon cells ( $310 \times 364$  mm) connected in series, arranged in six rows containing 6 cells each (Fig. 3). The modules are illuminated with separate incandescent lamps with an adjustable light intensity. The measurements of light intensity can be carried out using a luxmeter.



Fig. 1. The photovoltaic test station equipped with a single photovoltaic module

The modules in the generator can be connected either in series or in parallel. It is also possible to make a serial-parallel connection. A serial connection consists in the connection of a “+” electrode of one module with a “-” electrode of the next module, while a parallel connection consists in connecting a “+” electrode of one module with a “+” electrode of another module, and connecting the “-” electrodes in a similar way. A serial-parallel connection consists in a serial connection of  $2 \times 2$  modules and a parallel connection of the 2 rows.



Fig. 2. The photovoltaic test station equipped with four photovoltaic modules

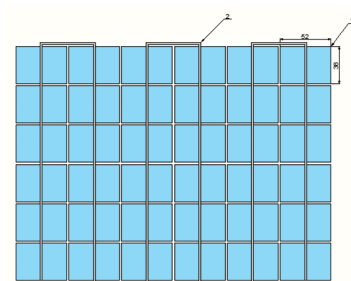


Fig. 3. Scheme of connection of cells in the tested photovoltaic modules,  
1 – an individual cell, 2 – connection of cells

## 2.2. Methodology of measurements

The two basic quantities used in photovoltaics are [6]:

- open circuit voltage – the highest voltage of a voltage source;
- short circuit current – the strongest current in an electric circuit.

The basic parameters of a photovoltaic module are obtained by examining its voltage-current characteristics [6]. In order to obtain these characteristics, the electric system presented in Fig. 4 was applied.

In the first photovoltaic station, the following measurements were carried out:

- A. The measurements of open circuit voltage and short circuit current at a temperature of 22°C and in the functions of:
- the radiation power (in the range from 4 to 540 W/m<sup>2</sup>, 14 measurement points); the angle of module inclination equal to 0° (the angle of radiation insistence equal to 90°); no shading;
  - the angle of module inclination (from 0° to 90°, with an interval of 10°); the radiation power 550 W/m<sup>2</sup>, no shading;
  - the ratio of module shading in the range from 0 to 5/6 (fraction), with an interval of 1/6 (fraction) in two ways: from left to right and from top to bottom (Fig. 3); the radiation power 550 W/m<sup>2</sup>; the module inclination angle 0°.

The temperature was measured on the module surface (see a thermometer in Fig. 1). In order to keep a constant temperature during the measurements, fans were applied (Fig. 1, 2). “No shading” means that the whole module surface was illuminated. It was easy to receive a shading interval of 1/6 to shadow the individual rows (Fig. 3).

- B. Tests of voltage-current characteristics ( Fig. 4) of the module at different values of radiation power (160, 300 and 520 W/m<sup>2</sup>) with a change of electric resistance from 0 to 970 Ω; the module inclination angle 0°; no shading.

In the second photovoltaic station, the above measurements were repeated for each individual module and the following voltage-current characteristics were tested:

- separately for the serial and parallel connections of modules 1 and 2,
- separately for the serial and parallel connections of modules 1, 2 and 3,
- separately for the serial and parallel connections of modules 1, 2, 3 and 4,

- for combined connection – a parallel connection of two separate serial connections of the modules 1 and 2 and the modules 3 and 4.

In electrical measurements, a digital multi-meter was used. The accuracy of the individual measurements were:

- ± (0.8% + 5 Digit) for voltage measurements,
- ± (1.2% + 5 Digit) for current measurements below 200 mA,
- ± (2.0% + 5 Digit) for current measurements above 200 mA.

For testing the stand, it was possible to measure the radiation power with a luxmeter using an approximate conversion factor:  $100 \text{ lux} \approx 1 \text{ W/m}^2$ . The luxmeter accuracy was ± (4% + 50 Digits).

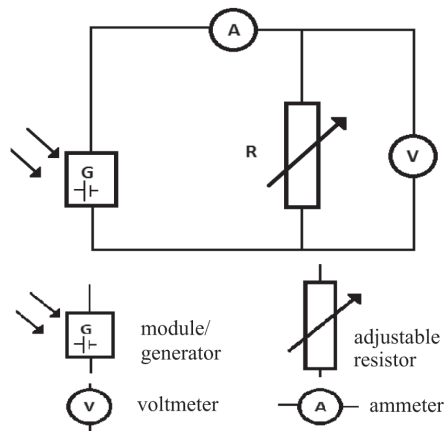


Fig. 4. Diagram of a voltage-current characteristics measurement station

### 3. Test results

The results are presented in the form of graphs. Each measurement point in the graphs represents a mean value of three results of measurements, which differ no more than 5%.

The following graphs present the results obtained in the test photovoltaic station equipped with a single module:

- the effect of radiation power on the open circuit voltage (Fig. 5),
- the effect of radiation power on the short circuit current (Fig. 6),
- the effect of the module inclination angle on the open circuit voltage (Fig. 7),
- the effect of the module inclination angle on the short circuit current (Fig. 8),
- the effect of the shading ratio of the module on the open circuit voltage (Fig. 9),
- the effect of the shading ratio of the module on the short circuit current (Fig. 10),
- the voltage-current characteristics and the power vs. voltage for three values of radiation power (Fig. 11),
- the voltage-current characteristics and the power vs. the voltage, and the module efficiency vs. the voltage for radiation power equal to  $300 \text{ W/m}^2$  (Fig. 12).

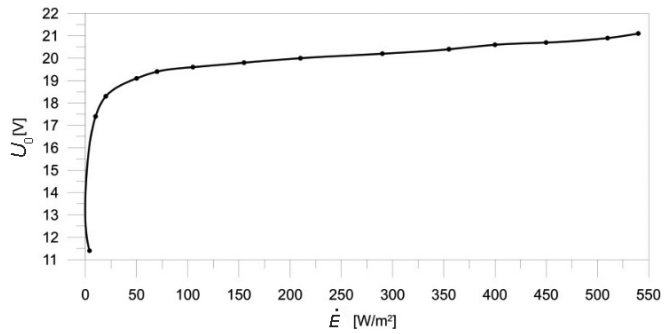


Fig. 5. The effect of radiation power on the open circuit voltage

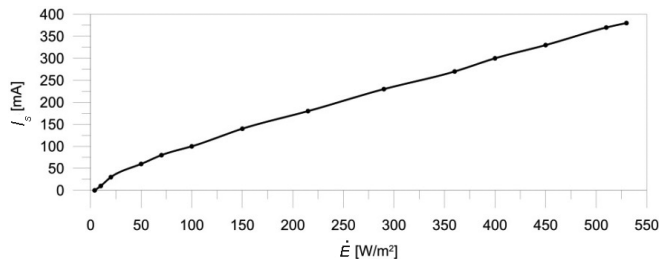


Fig. 6. The effect of radiation power on the short circuit current

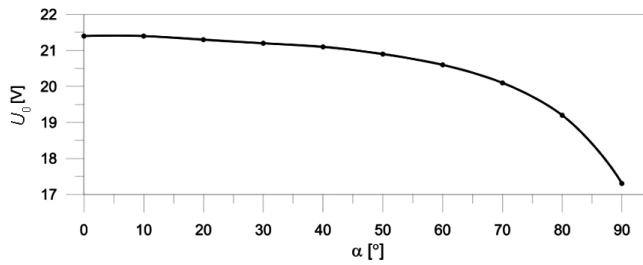


Fig. 7. The effect of the module inclination angle on the open circuit voltage

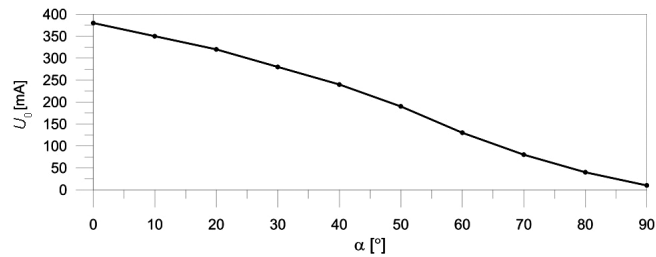


Fig. 8. The effect of the module inclination angle on the short circuit current

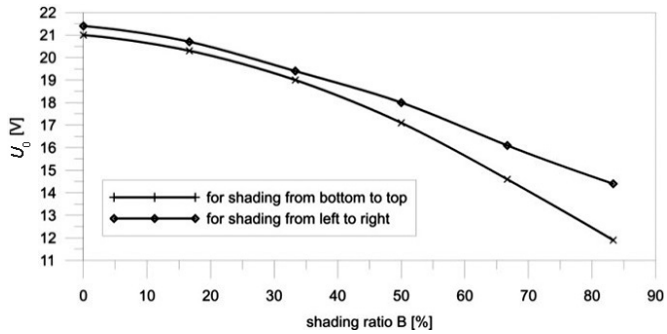


Fig. 9. The effect of the shading ratio of the module on the open circuit voltage

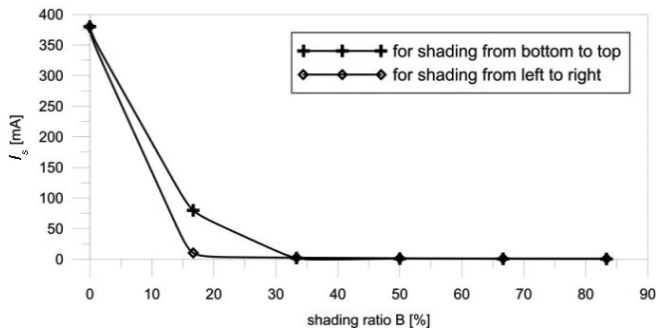


Fig. 10. The effect of the shading ratio of the module on the short circuit current

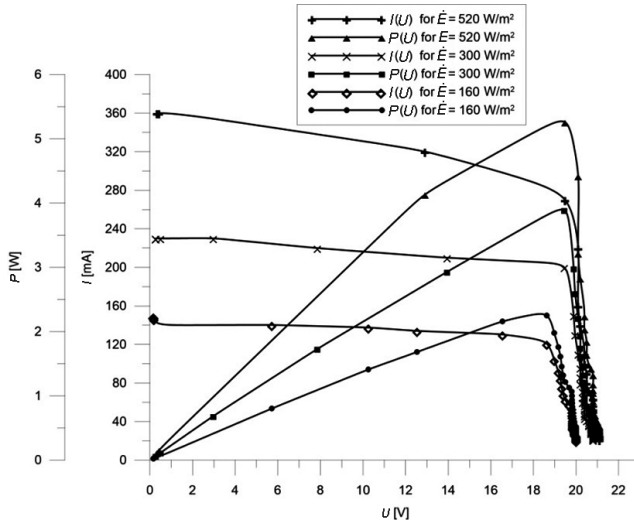


Fig. 11. The voltage-current characteristics and the power vs. the voltage for three values of radiation power

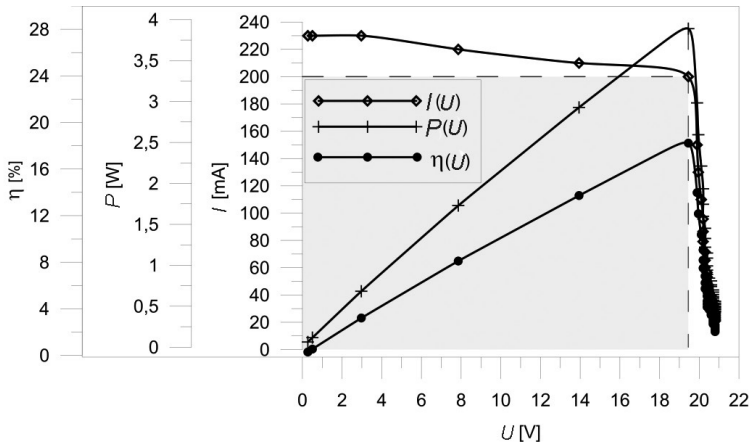


Fig. 12. The voltage-current characteristics and the power vs. the voltage, and the module efficiency vs. the voltage for radiation power equal to  $300 \text{ W/m}^2$

In Fig. 12, the point (200 mA, 18,7 V) corresponding to the maximum efficiency is the Maximum Power Point. The ratio of the shaded area to the area of rectangle  $230 \text{ mA} \times 21 \text{ V}$  is a filling factor FF. The filling factor is a measure of correctness of the module operation. In the case of an ideal module,  $FF = 1$ . In the case of the tested module,  $FF = 0,774$ .

On the other hand, the following exemplary graphs present the results obtained in the tests of photovoltaic station equipped with four modules:

- the voltage-current characteristics of individual modules 1, 2, 3, 4 and in case of serial connections 1+2, 1+2+3 and 1+2+3+4 at radiation power equal to  $640 \text{ W/m}^2$  (Fig. 13);
- the voltage-current characteristics of individual modules 1, 2, 3, 4 and in case of parallel connection 1+2+3+4 at radiation power equal to  $150 \text{ W/m}^2$  (Fig. 14).

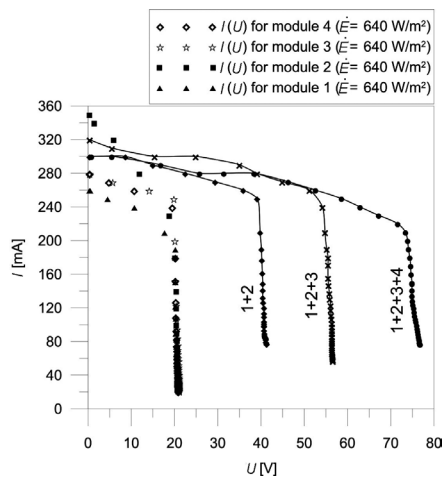


Fig. 13. Voltage-current characteristics of individual modules 1, 2, 3, 4 and in case of serial connections 1+2, 1+2+3 and 1+2+3+4 at radiation power equal to  $640 \text{ W/m}^2$

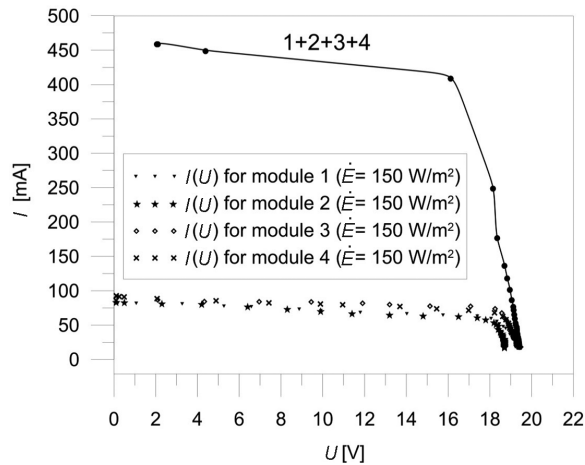


Fig. 14. Voltage-current characteristics of individual modules 1, 2, 3, 4 and in case of parallel connection 1+2+3+4 at radiation power equal to  $150 \text{ W/m}^2$

### 3. Conclusions

The results of measurements lead to the following conclusions:

- The photovoltaic cell has approximately a constant open circuit voltage. An increase in radiation power results in a slight increase of open circuit voltage, whereas a considerable, approximately linear, increase in the short circuit current (Fig. 5, 6).
- An increase in the module inclination angle results in both a decrease in the open circuit voltage and a fast decrease in the short circuit current, in comparison to the perpendicular angle of the radiation incidence (Fig. 7, 8).
- An increase of the shading ratio of the module results in a slight decrease in the open circuit voltage and in a fast decrease of the short circuit current (Fig 9, 10). A shading ratio of 15–30% decreases the short circuit current almost to 0, depending on the method of shading.
- An increase of radiation power results in a higher current at the same voltage, which results in a larger module power (Fig. 11).
- The filling factor for the tested modules is relatively high (Fig. 12). The closer the value of the filling factor is to 1, the closer the voltage-current characteristics are to that of an ideal cell.
- In the case of serial connections of the modules, theoretically, their total voltage should be the sum of the voltages of individual modules. In the case of a parallel connection, theoretically, their total current should be the sum of the currents of individual modules. Small deviations from this rule observed in practice – Figs. 13 and 14 respectively – result from some differences in the individual characteristics of the modules.
- A similarity of characteristics of various technical devices can be observed. The voltage-current characteristics of a photovoltaic module and the characteristics of a centrifugal pump are analogous (Fig. 12, 15): the module voltage corresponds with the pressure generated by the pump, whereas the module current corresponds with the pump capacity. On the other hand, the radiation power (module characteristics) corresponds with the rotational speed (pump characteristics). The courses of power and efficiency are similar in both cases.

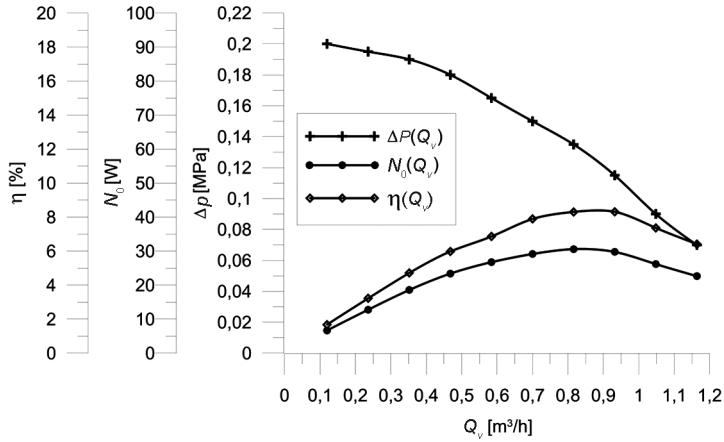


Fig. 15. An exemplary centrifugal pump characteristics received in laboratory tests: the pressure, the power and the pump efficiency vs. the pump capacity

The tested station can be successfully applied for research in the photovoltaic field.

## References

- [1] Directive 2009/29/EC of the European Parliament and of the Council of 23 April 2009 amending Directive 2003/87/EC so as to improve and extend the greenhouse gas emission allowance trading scheme of the Community, Document 32009L0029.
- [2] Decision No 406/2009/EC of the European Parliament and of the Council of 23 April 2009 on the effort of Member States to reduce their greenhouse gas emissions to meet the Community's greenhouse gas emission reduction commitments up to 2020 ("Effort Sharing Decision").
- [3] Directive 2009/28/EC of the European Parliament and of the Council of 23 April 2009 on the promotion of the use of energy from renewable sources and amending and subsequently repealing Directives 2001/77/EC and 2003/30/EC ("Renewable energy Directive").
- [4] Luque A., Hegedus S., *Handbook of Photovoltaic Science and Engineering*, 2<sup>nd</sup> Edition, John Wiley & Sons Ltd., New Jersey 2011.
- [5] Głuszek A., Pater S., Neupauer K., *Renewable Energy Sources – Laboratory Exercises*, Wydawnictwo Politechniki Krakowskiej, Kraków 2014.
- [6] Kirchensteiner W., *Solar Power Laboratory, Experimental Manual Off-grid and On-grid Technology*, Dr. Ing. Paul Christiani GmbH & Co. KG, Konstanz 2010.

JOANNA KUC, ADAM GROCHOWALSKI, TOMASZ ŚWIERGOSZ\*

## CORRELATION OF HEXABROMOCYCLODODECANE AND CONTENT OF FAT IN FISH

---

### BADANIE KORELACJI STĘŻENIA HEKSABROMOCYKLODODEKANU I ZAWARTOŚCI TŁUSZCZU W RYBACH

#### Abstract

A study on the correlation between the concentration of hexabromocyclododecane and the percentage of fat in meat tissues of selected marine fish species, both marine and farmed, has been carried out. The relationships between variables based on a determination of the coefficients of linear correlation  $r$ -Pearson were determined and graphs illustrating these dependencies were presented.

*Keywords: hexabromocyclododecane, correlation analysis*

#### Streszczenie

Przeprowadzono badanie korelacji pomiędzy stężeniem heksabromocyklododekanu i procentową zawartością tłuszczu w tkance mięsnej wybranych gatunków ryb morskich połowowych i hodowlanych. Określono zależności pomiędzy zmiennymi na podstawie wyznaczania współczynników korelacji liniowej  $r$ -Pearsona i przedstawiono wykresy obrazujące te zależności.

*Słowa kluczowe: heksabromocyklododekanm, badanie korelacji*

---

\* Ph.D. Eng Joanna Kuc, Prof. Ph.D. D.Sc. Eng. Adam Grochowalski, Eng. Tomasz Świergosz, Department of Analytical Chemistry, Faculty of Chemical Engineering and Technology, Cracow University of Technology.

## Abbreviations

BFR	–	Brominated Flame Retardant
EPS	–	Expanded Polystyrene
ESIS	–	European Chemical Substances Information System
HBCD	–	1,2,5,6,9,10 – hexabromocyclododecane
HIPS	–	High Impact Polystyrene
HPV	–	High Production Volume
OECD	–	Organization for Economic Cooperation And Development
POP	–	Persistent Organic Pollutant
REACH	–	Registration, Evaluation, Authorisation and Restriction of Chemicals
SD	–	Standard Deviation
XPS	–	Extruded Polystyrene

## 1. Introduction

Hexabromocyclododecane (CAS: 25637-99-4 for HBCD; 3194-55-6 for 1,2,5,6,9,10 – HBCD) is a brominated fire retardant added to many products made from plastic in order to ensure their incombustible properties [1–3]. According to information provided by the European Chemical Substances Information System (ESIS) [4], HBCD is on the list of HPV substances [5]. The HBCD production volume between 1995 and 1997 is estimated at 11,500 tons per year [6], while in 2001, production increased to 16700 tons of HBCD per year, of which most (9,500 tons) was in Europe [7]. Statistical data from 2002 indicate that the global production volume of HBCD from 2003 to 2007 also saw an increase [8], and as in the previous years, the largest consumer is Europe, especially Poland and Eastern European countries [6]. HBCD is mainly used as an additive to non-flammable expanded and extruded (EPS and XPS) polystyrene foams, high impact polystyrene (HIPS) and the textile industry. The segment production of building materials EPS and XPS consume the largest quantities of the total amount of HBCD production – more than 90% [9, 10]. EPS and XPS foams are known under the trade name ‘styrofoam’, which is mainly used as an insulating material of external and internal walls, foundations and at the attics, but also as insulation boards in transport vehicles and trucks as well as in child car seats, and as packaging materials [11, 12].

The physicochemical properties of polystyrene and especially the low density value and high porosity make it a highly desirable insulating material, and thus it is used in various products intended for the coastal aquaculture environment. The results of studies [13] confirm that buoys made with ESP contain significant levels of HBCD, which enters the water and bottom sediments, and consequently also the tissues of aquatic organisms. Furthermore, the containers used for storage and fish transport are also often made from EPS or XPS containing HBCD, resulting in a passage of this xenobiotic to the fish’s tissues [14].

There is no doubt that, in view of the risks to human health, the use of HBCD in EPS and XPS materials in products used in aquaculture coastal environments and on the market for the sale and breeding of fish seems to be pointless, especially as the danger of possible ignition of these materials is negligible. Fish are an important research material to the assessment of human exposure to the adverse effects of pollution, even though they are less consumed than meat and dairy products [15]. Another factor, which justifies the need to monitor the

concentrations of HBCD in fish, is frequently observed that the tissues of aquatic organisms, particularly fish with high fat content, is determined BFR at higher concentration levels than in the case of terrestrial organisms [16–18].

The Member States of the Organization for Economic Cooperation and Development (OECD) on the 24<sup>th</sup> meeting in 2007 agreed that HBCD has a high potential for bioaccumulation and biomagnification at different levels of the trophic pyramid and the properties indicating a threat to the environment including human health [19]. Bioaccumulation is a process resulting in the increase of concentration of the chemical substances in the living body as compared to the concentration observed in the environment in which the organism exists, taking into account all routes of exposure or absorption via the respiratory tract, skin and in food [20]. The HBCD bioaccumulation potential is linked to the lipophilic properties of the compound [21]. The biomagnification process can be considered as a special case of bioaccumulation, which relates to the increase in concentration of chemical substances in the living body compared to the concentration of the substance in the diet [20] and it is often the relationship between predator and prey thereof [22].

Tomy G. et al. [23, 24] confirm the strong positive linear correlation between concentrations of HBCD and trophic levels in the food web of Lake Ontario and the waters of the Arctic areas, which demonstrates the ability of HBCD to bioaccumulate and biomagnification in the chain of trophic relationships. Similar findings also indicate Law et al. based on the study of aquatic life in Lake Winnipeg (Canada) [25] and Morris et al. leader of the study samples from the North Sea (Europe) [26].

The procedure for the determination of HBCD is similar to other BFR or POP, and is usually multi-step and time consuming. Methods of extracting and purifying the samples have been well-developed over the past few/several years and they are commonly used as a reference in the analysis of environmental and biological samples as well as in food [27, 28]. HBCD is normally secreted from the sample in the extraction process, the extract is then purified, analytes are isolated from the sample matrix and separated from the interfering components. Choosing the appropriate techniques at different stages of the analytical methodology mainly depends on the sample matrix and the purpose of research. Various analytical techniques are applicable to samples, which are in various states of aggregation. Keeping quality control at every stage of the analytical methodology is a necessary element. In order to ensure the integrity of research, it is important to care about the representativeness of the taken samples, to ensure the uniformity and the immutability of the composition of samples from the moment of its collection to the final determination, validation of individual stages and the whole procedure, analytical and statistical evaluation of measurement results using various chemometric methods as a tool dedicated to analytical chemistry [29]. According to chemometric measurements, tools for the visualisation of the relationships in the data collection and classification of objects are useful as well as the relation between variables, which is implemented on the basis of determination of the coefficients of linear correlation ( $r$ ) – the most common r-Pearson, together with graphs showing these dependencies [30].

## 2. Materials

The samples of food constitutes meat tissues from farmed, marine and freshwater fish, such as the Atlantic salmon (Norwegian), rainbow trout, pangasius and tilapia and marine fish species: Alaska pollack, cod, hoki, hake, Atlantic herring, Atlantic halibut, Atlantic mackerel and sole. The study was selected from among the most common species of fish consumed in Poland, according to the information provided in reports of the Statistical Institute of Agricultural and Food Economics [15] and in [31]. In a few cases, two fish of the same species were investigated. All of the tested fish were purchased from the fish shop, to which the products are delivered directly from suppliers in fisheries or farming, according to information provided by the owner.

The general scheme of the analytical procedure with respect to the research is presented in Fig. 1. Details describing the individual steps of the experiment and the parameters of validation methods have been presented in previous studies [32].

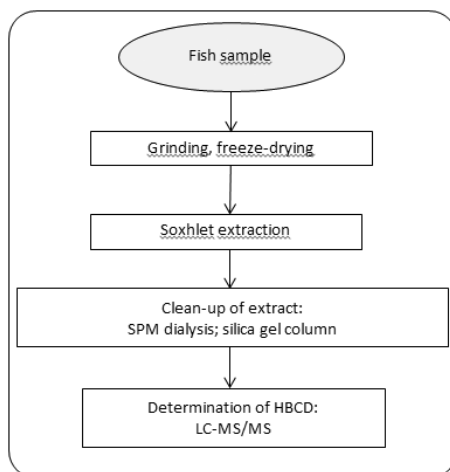


Fig. 1. Scheme of analytical procedure to prepare fish samples for LC MS/MS analysis

## 3. Results and discussion

For the determination of lipophilic compounds in food samples, such as HBCD, an important step is to determine the fat content [33, 34]. Hence, before cleaning extract/isolation of HBCD from fat matrix, fat determinations were performed for each sample. Using a rotary evaporator, the solvent was evaporated and the residual fat fraction was weighed and it determined the weight of raw fat, based on the weight of the sample to be analysed. The results of the fat content of the test samples of fish are summarised together with the result indications of HBCD in Table 1.

The lipophilic nature of HBCD causes that this compound accumulates in the adipose tissue of living organisms. Therefore, a study for the assessment of the concentration of the sum of isomers of HBCD on the fat content in the test samples has been conducted. In order

to test the correlation, all of the obtained results and studied groups were considered, and they were limited to the following factors:

- a) type of sample, all samples and one group consisted of farmed fish (No. 1–6) and the other consisted of marine fish (No. 7–16),
- b) fat content: divided into two groups of samples – the first comprised the fish that the fat content was less than 7%; the second group of those containing more than 7% fat. The value of 7% was taken as the limit based on the distribution of fish, taking into account the fat content in fish muscle PN-A-86770: 1999 [35]. Thus, the first group accounted for an average of fatty fish and lean fish, while the second group of oily fish.

The results are shown below.

Table 1

**Fat and HBCD content of the test samples of fish**

No.	Fish	Fat content %	Concentration of HBCD [pg/g fresh weight] ± SD
1	Atlantic salmon (Norwegian)	13	434 ± 44
2	Atlantic salmon (Norwegian)	14	152 ± 16
3	Rainbow trout	6.5	78 ± 7.1
4	Rainbow trout	6.0	101 ± 12
5	Pangasius	12	5.4 ± 0.65
6	Tilapia	12	2.4 ± 0.17
7	Pollack	4	6.4 ± 0.58
8	Cod	1	376 ± 36
9	Hoki	2	23 ± 2.1
10	Hake	1	14 ± 1.4
11	Atlantic herring	16	404 ± 33
12	Atlantic halibut	11	154 ± 14
13	Atlantic halibut	10	366 ± 26
14	Atlantic Mackerel	15	906 ± 75
15	Atlantic Mackerel	18	650 ± 55
16	Sole	12	18 ± 2.4

Based on a survey of correlation between the concentration of HBCD and fat content in the samples, it was found that there is a strong positive linear relationship ( $r = 0.6105$ ) only in the case of samples with a fat content of more than 7%. The correlation coefficient for marine fish catch is also positive, and it is a highly linear relationship ( $r = 0.6377$ ), which may result from the fact that, in the present group, most fish species are oily fish.

It can therefore be argued that the potential accumulation of HBCD will increase with increasing fat content in the tissue of the test fish, due to the lipophilic properties of the compound. The statistical significance of the correlation coefficients was confirmed by the  $t$ -test ( $|t| \geq t_{\alpha=0,05, n-2}$ ).

Test results of HBCD in the tissues of fish confirm the ability of this compound to bioaccumulate, while the results of the correlation between the analyte concentration and fat content of the samples confirm the lipophilic character of the compound. In the study on the category of “Fish meat” [36], the results indicate a significant relationship between the fat content and the concentration of polybrominated diphenyl ethers (PBDEs), which are also in the group of additive flame retardants.

## References

- [1] Heeb N.V., Schweizer W.B., Kohler M., Gerecke A.C. *Structure elucidation of hexabromocyclododecanes – a class of compounds with a complex stereochemistry*. Chemosphere, 61, 2005, 65–67.
- [2] Heeb N.V., Schweizer W.B., Mattrel P., Haag R., Gerecke A.C., Kohler M., Schmid P., Zennegg M., Wolfensberger M., *Solidstate conformations and absolute configurations of (+) and ()alpha-, beta-, and gamma-hexabromocyclododecanes (HBCDs)*, Chemosphere 68, 2007, 940–950.
- [3] Law R.J., Kohler M., Heeb N.V., Gerecke A.C., Schmid P., Voorspols S., Covaci A., Becher G., Janak K., Thomsen C., *Hexabromocyclododecane challenges scientists and regulators*. Environmental Science & Technology, 39, 2005, 281A–287A.
- [4] Data Sheet: *Result for EC#: 247-148-4 HBCD* <http://esis.jrc.ec.europa.eu/index.php?P-GM=hpv> (access january 2015).
- [5] *HPV data summary and test plan for hexabromocyclododecane (HBCD) CAS No. 3194556*. American Chemistry Council Brominated Flame Retardant Industry Panel (BFRIP) 1300 Wilson Blvd Arlington, Virginia 2001.
- [6] *Risk Assessment Hexabromocyclododecane CAS-No.: 25637-99-4 EINECS-No.: 247-148-4* Final report May 2008. Final approved version, European Union Risk Assessment Report. 2008. Office for Official Publications of the European Communities. R044\_0805\_env\_hh\_final\_ECB.doc
- [7] Janák K., Covaci A., Voorspols S., Becher G., *Hexabromocyclododecane in marine species from the Western Scheldt Estuary: diastereoisomer- and enantiomer-specific accumulation*. Environmental Science & Technology, 39, 2005, 1987–1994.
- [8] Arctic Monitoring and Assessment Programme (AMAP) Report 2007:6 SFT Report TA–2440/2008. Final Report of Phase I of the ACAP Project on Brominated Flame Retardants (BFRs). Phase I: *Inventory of sources and identification of BFR alternatives and management strategies*, Oslo 2007.
- [9] *Data on manufacture, import, export, uses and releases of HBCDD as well as information on potential alternatives to its use*. The technical work on this report has been led by IOM Consulting, supported by BRE, PFA and Entec under framework contract ECHA/2008/02/SR4/ECA.226.

- [10] Exploration of managements options for Hexabromocyclododecane. *Report to the 8<sup>th</sup> meeting of the UNECE Task Force on Persistent Organic Pollutants*, Montreal 2010.
- [11] U.S. Environmental Protection Agency (2012). *Significant New Use Rule for Hexabromocyclododecane and 1,2,5,6,9,10-Hexabromocyclododecane*, 77 FR 17386-17394.
- [12] NICNAS, *National Industrial Chemicals Notification and Assessment Scheme. Priority Existing Chemical Assessment Report No.34. Hexabromocyclododecane*. Sydney 2012.
- [13] Al-Odaini N. A., Shim W. J., Han G. M., Jang M., Hong S. H., *Enrichment of hexabromocyclododecanes in coastal sediments near aquaculture areas and a wastewater treatment plant in a semi-enclosed bay in South Korea*. *Science of the Total Environment*, 505, 2015, 290–298.
- [14] Rani M., Shim W. J., Han G. M., Jang M., Song Y. K., Hong S. H., *Hexabromocyclododecane in polystyrene based consumer products: An evidence of unregulated use*, *Chemosphere*, 110, 2014, 111–119.
- [15] Pieńkowska B., *Spożycie ryb, IERiGŻ: Rynek ryb: Stan perspektywy. Analizy rynkowe*, Wyd IERiGŻ, Warszawa 2008.
- [16] Darnerud P. O., *Toxic effects of brominated flame retardants in man and in wildlife*. *Environment International*, 29, 2003, 841–53.
- [17] Thomann R. V., *Modeling organic chemical fate in aquatic systems: significance of bioaccumulation and relevant time-space scales*, *Environmental Health Perspectives*, 103, 1995, 53–57.
- [18] Elskus A., Collier T. K., Monossone E. Ch., 4: *Interactions between lipids and persistent organic pollutants in fish*, *Biochemistry and Molecular Biology of Fishes*, 6, 2005.
- [19] Organization for Economic Cooperation And Development (OECD). *SIDS Initial Assessment, Profile for Cas. No. 25637-99-4, 3194-55-6, Hexabromocyclododecane (HBCDD)*. 2007. <http://webnet.oecd.org/Hpv/UI/handler.axd?id=ea58ac11-e090-4b24-b281-200ae351686c> (access: january 2015).
- [20] Mackay D., Fraser A., *Bioaccumulation of persistent organic chemicals: mechanisms and models*, *Environ. Pollut.*, 110, 2000, 375–391.
- [21] *CHL report for hexabromocyclododecane. Proposal for Harmonised Classification and Labelling*. Based on the CLP Regulation (EC) No 1272/2008, Annex VI, Part 2 Substance Name: Hexabromocyclododecane, 2009.
- [22] Newman M. C. Ch., 5: *Bioaccumulation from Food and Trophic Transfer w Fundamentals of Ecotoxicology: The Science of Pollution*, CRC Press, Taylor & Francis Group.
- [23] Tomy G. T., Budakowski W., Halldorson T., Whittle D. M., Keir M. J., Marvin C., MacInnis G., Alaei M., *Biomagnification of  $\alpha$ - and  $\gamma$ -hexabromocyclododecane isomers in a Lake Ontario food web*, *Environmental Science & Technology*, 38, 2004, 2298–2303.
- [24] Tomy G., Pleskach K., Oswald T., Halldorson T., Helm P. A., MacInnis G., Marvin C. H., *Enantioselective bioaccumulation of hexabromocyclododecane and congener-specific accumulation of brominated diphenyl ethers in an eastern Canadian Arctic marine food we.* *Environmental Science & Technology*, 42, 2008, 3634–3639.
- [25] Law K., Halldorson T., Danell R., Stern G., Gewurtz S., Alaei M., Marvin C., Whittle M., Tomy G., *Bioaccumulation and trophic transfer of some brominated flame retardants in a Lake Winnipeg (Canada) food web*, *Environmental Toxicology and Chemistry*, 25, 2006, 2177–2186.

- [26] Morris S., Allchin C.R., Zegers B. N., Haftka J.J.H., Boon J. P., Belpaire C., Leonards P. E.G., van Leeuwen S., de Boer J., *Distribution and fate of HBCD and TBBPA brominated flame retardants in North Sea estuaries and aquatic food webs*, Environmental Science & Technology, 38, 2004, 5497–5504.
- [27] Morris S., Bersuder P., Allchin C. R., Zegers B., Boon J. P., Leonards P. E. G., de Boer J., *Determination of the brominated flame retardant, hexabromocyclododecane, in sediments and biota by liquid chromatography-electrospray ionisation mass spectrometry*, Trends in Analytical Chemistry, 25, 2006, 343–349.
- [28] Xu W., Wang X., Cai Z., *Analytical chemistry of the persistent organic pollutants identified in the Stockholm Convention: A review*, Analytica Chimica Acta, 790, 2013, 1–13.
- [29] Zuba D., Parczewski A., *Chemometria w nauce i praktyce*, IES Kraków 2009.
- [30] Konieczka P., Namieśnik J., *Ocena i kontrola jakości wyników pomiarów analitycznych*, Wydawnictwo Naukowo Techniczne, Warszawa 2007.
- [31] Pieniak Z., Kołodziejczyk M., Kowrygo B., Verbeke W., *Consumption patterns and labelling of fish and fishery products in Poland after the EU accession*, Food Control, 22, 2011, 843–850.
- [32] Kuc J., Grochowalski A., Mach S., Placha D., *Level of hexabromocyclododecane isomers in the tissue of selected commonly consumed fish in Central European countries*, Acta Chromatographica, 26, 2014, 575–585.
- [33] Gómara B., Lebrón-Aguilar R., Quintanilla-López J.E., José M., *Development of a new method for the enantiomer specific determination of HBCD using an ion trap mass spectrometer*, Analytica Chimica Acta, 605, 2007, 53–60.
- [34] Covaci A., Voorspoels S., Ramos L., Neels H., Blust R., *Recent developments in the analysis of brominated flame retardants and brominated natural compounds*, Journal of Chromatography A, 1153, 2007, 145–171.
- [35] PN-A-86770:1999, Ryby i przetwory rybne. Terminologia.
- [36] Scientific Opinion on Polybrominated Diphenyl Ethers (PBDEs) in Food. European Food Safety Authority (EFSA) Panel on Contaminants in the Food Chain, EFSA Journal 9, 2011.

BARBARA LARWA, MIKOŁAJ TEPER, KRZYSZTOF KUPIEC\*

## HORIZONTAL GROUND HEAT EXCHANGERS – ANALYTICAL SOLUTIONS AND NUMERICAL SIMULATIONS

---

## GRUNTOWE WYMIENNIKI CIEPŁA – ROZWIĄZANIA ANALITYCZNE I SYMULACJE NUMERYCZNE

### Abstract

This paper concerns the basics of modelling ground heat exchangers. Several specific cases were described, for which computational dependencies and calculation results were presented. Models based on analytical solutions were considered as well as models that use computer applications based on numerical calculations.

*Keywords: transient heat conduction, numerical simulations, ground heat exchangers*

### Streszczenie

Praca dotyczy podstaw modelowania gruntowych wymienników ciepła. Opisano kilka szczególnych przypadków, dla których przedstawiono zależności obliczeniowe oraz wyniki obliczeń. Rozważono zarówno modele oparte na rozwiązaniach analitycznych jak również modele wykorzystujące aplikacje komputerowe bazujące na obliczeniach numerycznych.

*Słowa kluczowe: nieustalone przewodzenie ciepła, symulacje numeryczne, gruntowe wymienniki ciepła*

---

\* Ph.D. Eng. Barbara Larwa, Msc. Eng. Mikołaj Teper, Prof. Ph.D. D.Sc. Eng. Krzysztof Kupiec, Chair of Chemical and Process Engineering, Faculty of Chemical Engineering and Technology, Cracow University of Technology.

### Nomenclature:

- $a$  – thermal diffusivity coefficient,  $\text{m}^2/\text{s}$   
 $B$  – oscillation amplitude around the temperature  $T_b$ , K  
 $k$  – heat conduction coefficient,  $\text{W}/(\text{mK})$   
 $\dot{Q}$  – rate of heat transfer, W  
 $s$  – thickness of the plate, m  
 $t$  – time, days  
 $t_{\max}$  – time since the beginning of the calendar year to the day in which the temperature is the highest, days  
 $T$  – temperature of the ground,  $^{\circ}\text{C}$   
 $T_a$  – average daily ambient air temperature,  $^{\circ}\text{C}$   
 $T_b$  – average annual ambient air temperature,  $^{\circ}\text{C}$   
 $T_i$  – initial temperature of the ground,  $^{\circ}\text{C}$   
 $T_0$  – temperature of the body,  $^{\circ}\text{C}$   
 $x$  – position coordinate in the ground (vertical), m  
 $y$  – position coordinate in the ground (horizontal), m  
 $\omega$  – frequency, 1/day

## 1. Introduction

Internal energy of the ground is used for heat pumps. When heat is received from the ground, usually the so-called closed systems are used, which utilise the diaphragm heat exchangers located in the ground. A liquid, low-temperature heat-carrying agent is circulating in the system.

Often, in modelling, ready applications are used. ANSYS Transient Thermal is frequently used for digital simulations.

Wu et al. [1] investigated the thermal performance of slinky heat exchangers for ground source heat pump systems for the UK climate. The authors presented the results of experimental measurements as well as of a numerical simulation using a three-dimensional CFD code ANSYS Fluent. This application was also used by Benazza et al. [2] to study the influence of the thermal conductivities and geometrical parameters on the heat exchanger efficiency. Condego et al. [3] performed calculations using Fluent for simulations of different configurations of a horizontal ground heat exchanger, in order to evaluate the characteristics of these systems in the most common layouts and under different working conditions. A 3D numerical model was also developed by Chong et al. [4]. The authors presented the thermal performance results for various heat exchanger configurations by comparing the heat transfer rate as well as the amount of pipe material needed.

This paper presents some simple cases concerning heat conduction in the ground. They have a practical significance for the modelling and simulation of ground heat exchangers coupled with heat pumps. The following have been considered:

- Heat conduction in the ground with no heat exchangers installed,
- Heat conduction in the ground with horizontal tubes arranged in parallel, assuming a homogeneous initial ground temperature,
- Steady heat conduction between horizontal pipes arranged in parallel on the ground surface.

None of the mentioned cases correspond precisely to the operating conditions of ground heat exchangers, since in reality, heat is extracted from the ground, the ground temperature varies with the position, and the process of heat transfer is transient. However, when constructing mathematical models, it is advantageous to be able to verify the obtained results for special cases. This work is dedicated to such extreme cases.

## 2. Analysis of climatic data

Parallel to the heat transfer between the ground and the working fluid in an exchanger, the heat is transported between the surface of the ground and the environment. It has a particular significance in the modelling of horizontal exchangers located at a small depth. In order to take this heat flux into consideration, the course of the ambient temperature as a function of time should be known. When examining the average daily temperature, this course can be described using trigonometric functions [5]. In order to elaborate the climatic data to form a mathematical relationship, the following model was applied:

$$T_a = T_b + B \cdot \cos[\omega(t - t_0)] \quad (1)$$

The frequency  $\omega$  is:

$$\omega = \frac{2\pi}{t_c} \quad (2)$$

where  $t_c$  is the number of days in a year ( $\approx 365$ ). Thus,  $\omega = 0.0172 \text{ day}^{-1}$ . Relationship (1) was reduced to linear form:

$$T_a = T_b + b_1 X_1 + b_2 X_2 \quad (3)$$

where:

$$b_1 = B \cdot \cos(\omega t_0) \quad (4)$$

$$b_2 = B \cdot \sin(\omega t_0) \quad (5)$$

$$X_1 = \cos(\omega t) \quad (6)$$

$$X_2 = \sin(\omega t) \quad (7)$$

For calculations, climatic data for Cracow, shown in [6], were used. The coefficients were calculated using the method of least squares:  $T_b = 8.5^\circ\text{C}$ ,  $b_1 = 10.17 \text{ K}$ ,  $b_2 = -2.755 \text{ K}$ . Next, when solving the system of equations (4)–(5), one can evaluate:  $B = -10.4 \text{ K}$ ,  $t_0 = 15.4 \approx 15 \text{ days}$ . Therefore, the relationship, which describes temporal changes of ambient air temperature, takes the form:

$$T_a = 8.5 - 10.4 \cdot \cos[\omega(t - 15)] \quad (8)$$

Value of  $t_0$  concerns the day, when the annual average temperature is the lowest and equals:  $8.5 - 10.4 = -1.9^\circ\text{C}$ . After a period of half a year ( $t_c/2 \approx 183$  days), air temperature reaches a maximum of is  $8.5 + 10.4 = 18.9^\circ\text{C}$ . Thus, the relationship equivalent to (8) is:

$$T_a = 8.5 + 10.4 \cdot \cos[\omega(t - 198)] \quad (8a)$$

The course of this function is shown in Figure 1, including the climatic data used for calculations.

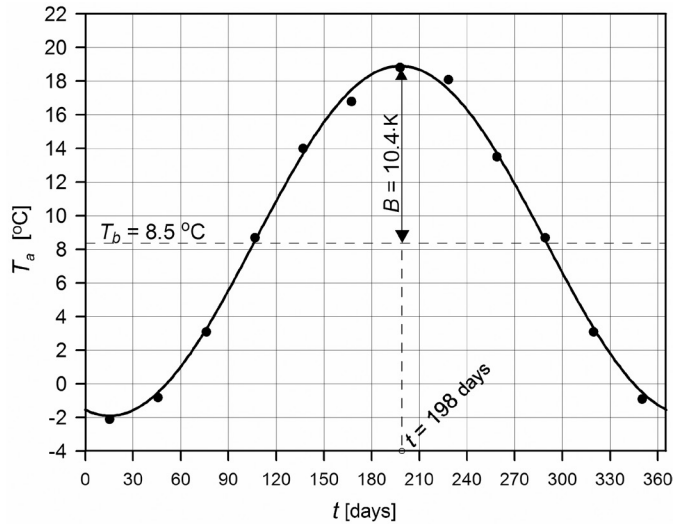


Fig. 1. Approximation of climatic data

### 3. Heat transfer in the ground taking into account an interaction with the ground surface

In order to determine the temperature distribution in the ground under natural conditions, the model of semi-infinite body is generally used. The analytical solution for both cases is known when the thermal resistance occurs only in the ground, as well as when the resistances occur in the ground and during heat transfer between the ground and the environment [7, 8].

Due to the fact that ambient temperature changes cyclically, the atmosphere interaction on the ground is limited. As a result of atmosphere interaction, the ground periodically heats up or cools down. A distant limited range of the climatic conditions' influence on the ground enables the use of an analytical solution for an infinite plate. However, the condition for the applicability of this solution is that the plate thickness exceeds the thickness of the ground zone in which temperature changes occur, caused by climatic conditions.

Below, an analytic solution for heat conduction for an infinite plate is presented, of which one surface ( $x = 0$ ) is at a constant temperature and the second one ( $x = s$ ) is subjected to cyclic temperature changes. The solution concerns a uniform plate temperature at the

beginning of the process. In the presented system, during each time interval, the temperature profiles change until they reach a cyclic steady state. The adequate differential equation and conditions take the form:

$$\frac{\partial T}{\partial t} = a \frac{\partial^2 T}{\partial x^2} \quad (9)$$

The initial condition:

$$t = 0 \quad T = T_i \quad (10)$$

The boundary conditions:

$$x = 0 \quad T = T_b = T_i \quad (11)$$

$$x = s \quad T = T_b + B \cdot \sin[\omega(t - t_{\max})] \quad (12)$$

The solution is [7]:

$$T = T_b + AB \cdot \sin[\omega t + \varepsilon + \phi] + 2\pi \sum_{i=1}^{\infty} \frac{i(-1)^i \cdot (i^2 \mu^2 \cdot \sin \varepsilon - 2R^2 \cdot \cos \varepsilon)}{i^4 \pi^4 + 4R^4} \sin\left(i\pi \frac{x}{s}\right) \cdot \exp\left(-i^2 \pi^2 \frac{at}{s^2}\right) \quad (13)$$

where:

$$A = \sqrt{\frac{\cosh(2R x/s) - \cos(2R x/s)}{\cosh(2R) - \cos(2R)}} \quad (14)$$

$$\varphi = A \cdot \tan \frac{p_1 - p_2}{1 + p_1 p_2} \quad \text{mod } \pi \quad (15)$$

$$p_1 = \frac{\tan(R x/s)}{\tanh(R x/s)} \quad (16a)$$

$$p_2 = \frac{\tan R}{\tanh R} \quad (16b)$$

$$R = \frac{s}{L} \quad (17)$$

$$\varepsilon = -t_{\max} \omega \quad (18)$$

The sum of the first two terms of the solution (13) refers to the cyclic steady state; in this state, the third term (containing the sum of the infinite series) resets.

For calculations, the following data were used:  $T_b = 8.5^\circ\text{C}$ ,  $B = 10.4 \text{ K}$ ,  $t_{\max} = 198 \text{ days}$ ,  $a = 0.384 \cdot 10^{-6} \text{ m}^2/\text{s}$ . The amount  $L$  with linear dimension calculated from formula:

$$L = \sqrt{\frac{2a}{\omega}} \quad (19)$$

equals  $L = 1.96 \text{ m}$ . The thickness of the ground layer, beyond which there are no longer any temperature changes, was assumed as 7-times greater than  $L$  ( $R = 7$ ). Thus,  $s = 7 \cdot 1.96 = 13.75 \text{ m}$ .

In Fig. 2, the ground temperature profiles under natural conditions in a 3-months period (15 Jan – the lowest ambient temperature, 15 Jul – the highest ambient temperature) were presented. The value of  $x = 0$  corresponds to the bottom surface of the plate at a constant temperature  $T = T_b$  and the value of  $x = 1$  refers to the upper surface of the plate, the same as the ground surface. The cyclic steady state was reached after approx. 5 years of process' duration (on the assumption that the initial temperature was uniform). In this state, the temperature course near  $x = 0$  is position independent and the lines are practically vertical.

In Fig. 3, the temporal courses of temperature at several ground depths were presented. The value of  $t = 1 \text{ year}$  corresponds to the value of dimensionless time  $at/s^2 = 0.0641$ . For a depth of 13.75 m (and higher), the temperature does not change with time. For a depth of 8 m, there are slight temperature changes, but they are significantly different in the subsequent years of the process. And for a depth of 2 m, the temperature changes are significant within 1 year, but the differences between successive years are insignificant.

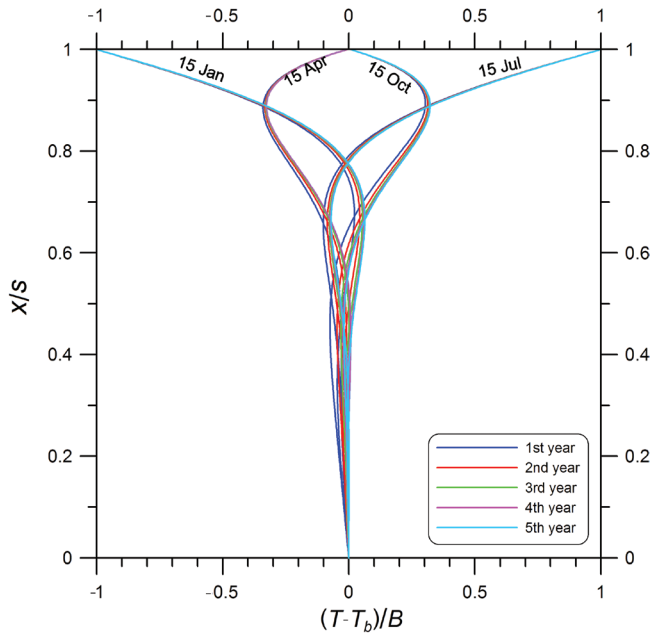


Fig. 2. Temperature profiles in the ground under natural conditions

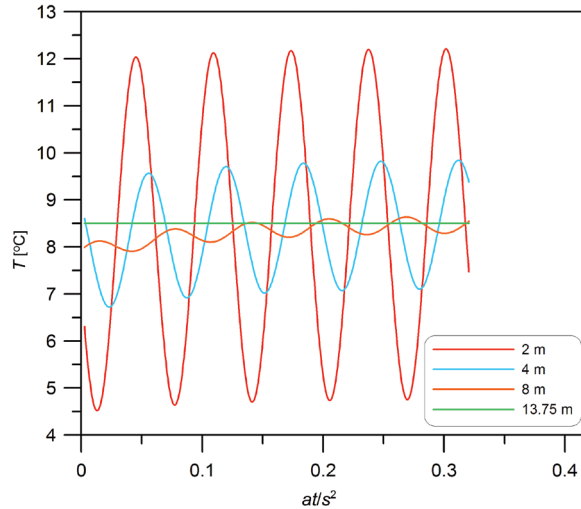


Fig. 3. The temporal courses of temperature of the ground

The analysis has the following practical significance. At numerical calculations relating to heat conduction in the ground, assuming a uniform initial temperature of the ground, the simulations should be carried out for a time value corresponding to at least a few cycles because a numerically determined temperature profile after one cycle (of the year) may differ significantly from the profile reached in the cyclic steady state.

#### 4. Simulation of heat conduction in the ground heated by a horizontal pipe system – using ANSYS application

With slight changes in the temperature of the working fluid between the inlet and the outlet in a horizontal ground heat exchanger, heating or cooling of the ground can be treated as a two-dimensional problem. The flow through 7 horizontal tubes that are coupled in parallel and are located in the ground has been considered. The problem can be described by a two-dimensional equation of transient heat conduction.

$$\frac{\partial T}{\partial t} = a \left( \frac{\partial^2 T}{\partial x^2} + \frac{\partial^2 T}{\partial y^2} \right) \quad (20)$$

The initial condition follows from the assumption of a uniform ground temperature at the beginning of the process, whereas the boundary condition follows from the constant (with time and space) surface temperature value of all of the tubes. For the calculation, the following data was used:  $a = 0.384 \cdot 10^{-6} \text{ m}^2/\text{s}$ ,  $T_0 = 5^\circ\text{C}$ ,  $T_i = 15^\circ\text{C}$ , the dimensions of the analysed ground fragment:  $1.5 \times 0.6 \times 0.4 \text{ m}$ . Furthermore, it was assumed that the outer diameter of the tubes is equal to 38 mm and that the distance between the axes of the pipes is equal to 150 mm. The simulation was carried out using the ANSYS application (number of nodes: 381270). The calculation results were presented in Figs. 4a, b, c.

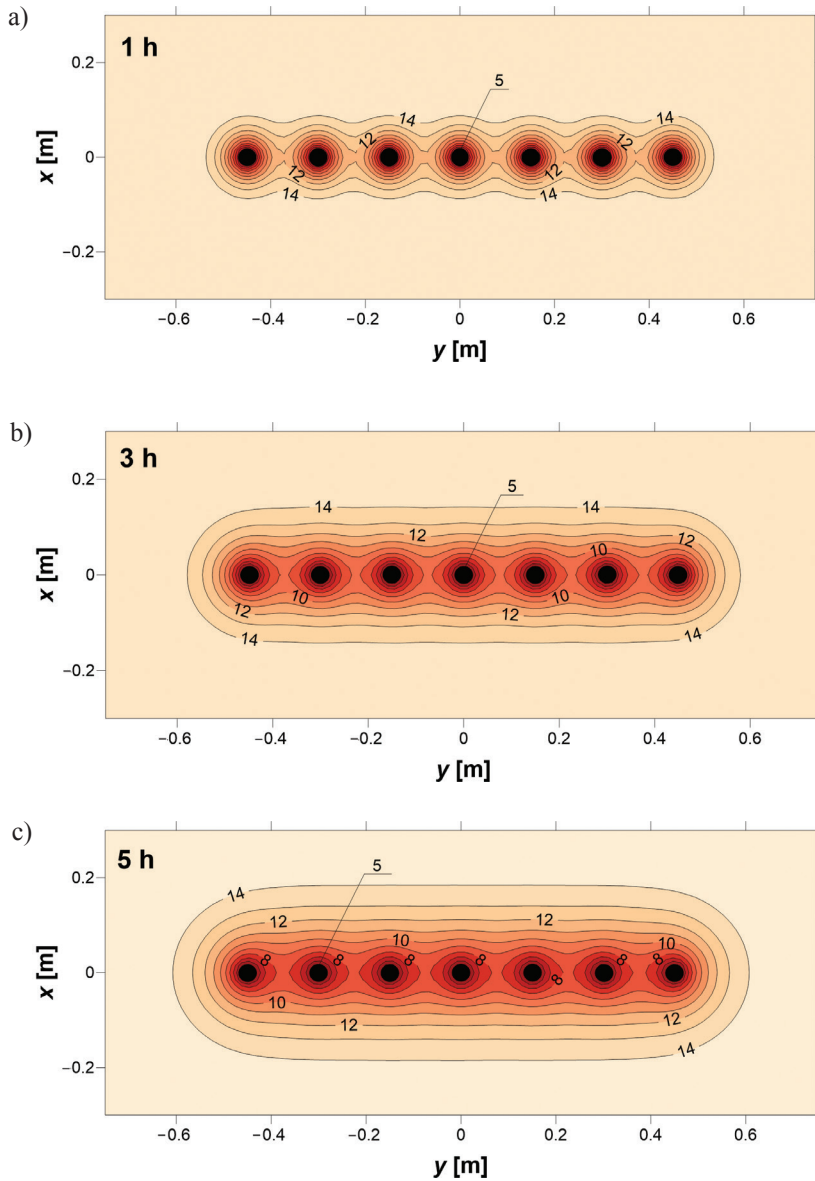


Fig. 4a, b, c. Heat conduction in the ground – digital simulation

The figures are related to the cross section of the pipe system. Lines of a constant temperature of the ground expressed by numbers (in °C) were shown. On the axes, suitable location coordinates are in the ground. Tubes are at a sufficient distance from the ground surface, providing the absence of interactions with external environmental conditions. As one can see, at the beginning, each pipe cools down the ground individually and independently

of the other tubes. However, after some time, the temperature fronts come together and more lines of the constant temperature have a more rectilinear shape and are parallel to the course of the  $y$  axis. Thus, the system behaves similarly to the process of ground cooling by an infinite plate. The similarity is even larger when there are more tubes installed, and when they are more densely arranged side by side.

## 5. Steady heat conduction

When a body with a constant (surface) temperature  $T_0$  (different with  $T_i$ ) is located in the ground at a uniform temperature  $T_p$ , the heat transfer occurs between the body surface and the ground. When  $T_0 < T_p$ , the ground is cooling. Generally, the process has a transient character. However, when there is an object in the ground that can receive the heat, after some time, the heat transfer might become steady. This object can be, for example, the surface of the ground. When the heat flux from the ground to the body surface equals the flux from the environment to the ground surface, the heat transfer is steady. Depending on the configuration of the surfaces involved in heat transfer, there are relationships from which one can calculate the heat flux.

The rate of heat transfer related to single tube is calculated from the formula [9]:

$$\dot{Q} = Sk(T_i - T_0) \quad (21)$$

The case of horizontal pipes arranged in parallel in the ground, at a distance from the ground surface  $z$ , was considered. Coefficient  $S$ , in this case, can be computed from the formula (calculated on a single tube):

$$S = \frac{2\pi L}{\ln\left(\frac{2w}{\pi d} \cdot \sinh \frac{2\pi z}{w}\right)} \quad (22)$$

When there is only one tube in the ground, the coefficient  $S$  is as follows:

$$S = \frac{2\pi L}{\ln \frac{4z}{d}} \quad (23)$$

Relationships are valid for  $z > 1.5d$ .

In Fig. 5, a graphic interpretation of the mentioned dependencies was presented. For the calculation, it was assumed:  $d = 0.038$  m,  $k = 0.9$  W/(m·K) and  $T_i - T_0 = 10$  K. As can be seen, the heat flux related to a single tube (refers to its length) strongly decreases with the depth  $z$ , where pipes are arranged. However, the opposite is the influence of the spacing between pipes: the longer the distances  $w$ , the greater the heat flux. For only one tube located in the ground, an appropriate curve ( $w \rightarrow \infty$ ) is situated the highest.

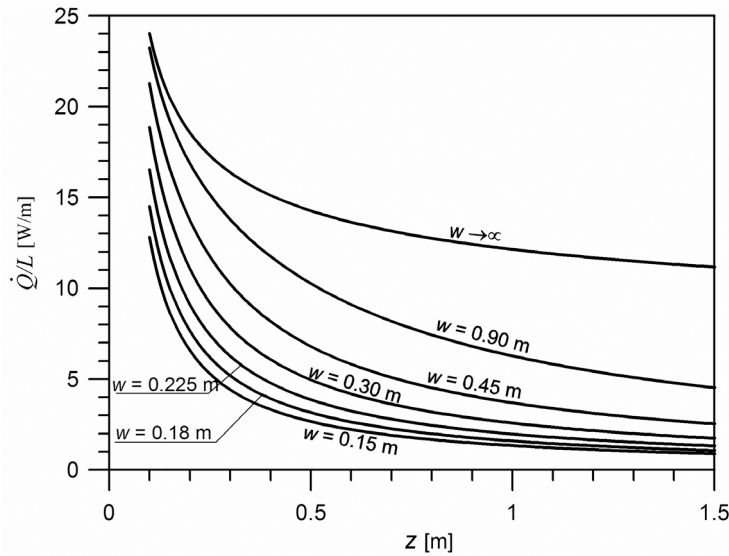


Fig. 5. Steady conduction in the ground

## 6. Conclusions

- With an application of the trigonometric functions used in the model in order to correlate to the climatic temperature data, a very good fitting was obtained.
- In numerical simulations related to heat conduction in the ground, taking into consideration the interaction with the surface, it should be taken into account that due to the existence of the cyclic steady state, it is necessary to carry out the calculations for at least a few annual cycles. For the calculation, one can use relationships for an infinite plate as long as its thickness exceeds the depth of the ground, where there are changes in temperature.
- With a heat conduction simulation of a series of parallel ground heat exchanger tubes, it has been found that the generated constant temperature lines become close to straight lines after a certain period of time. This gives the basis for the simplification of the modelling process of horizontal ground heat exchangers. Reference simulations were performed by using ANSYS codes.
- Calculation relationships for steady heat conduction in the ground can be used as a particular case of heat transfer in the ground, which is helpful for testing models concerning transient heat conduction.

## References

- [1] Wu Y., Gan G., Verhoef A., Vidale P.L., Gonzalez R.G., *Experimental measurement and numerical simulation of horizontal-coupled slinky ground source heat exchangers*, Applied Thermal Engineering, Vol. 30, 2010, 2574–2583.
- [2] Bennazza A., Blanco E., Aichouba M., Rio J.L., Laouedi S., *Numerical investigation of horizontal ground coupled heat exchanger*, Energy Procedia, Vol. 6, 2011, p. 29–35.
- [3] Condego P.M., Colangelo G., Starace G., *CFD simulations of horizontal ground heat exchangers: A comparison among different configurations*, Applied Thermal Engineering, Vol. 33–34, 2012, 24–32.
- [4] Chong C.S.A., Gan G., Verhoef A., Garcia R.G., Vidale P.L., *Simulation of thermal performance of horizontal slinky-loop heat exchangers for ground source heat pumps*, Applied Energy, Vol. 104, 2013, 603–610.
- [5] Adamovsky D., Neuberger P., Adamovsky P., *Changes in energy and temperature in the ground mass with horizontal heat exchangers – The energy source for heat pumps*, Energy and Buildings, Vol. 92, 2015, 107–115.
- [6] [www.pogodynka.pl/polska/daneklimatyczne/](http://www.pogodynka.pl/polska/daneklimatyczne/) (access: 13.09.2013).
- [7] Carslaw H.S., Jaeger J.C., *Conduction of heat in solids*, second ed., Clarendon Press, Oxford 1959.
- [8] Kupiec K., Larwa B., Gwadera M., *Heat transfer in horizontal ground heat exchangers*, Applied Thermal Engineering, Vol. 75C, 2015, 270–276.
- [9] Cengel Y., Ghajar A., *Heat and mass transfer: fundamentals and applications*, McGraw-Hill, 2010.



MAGDALENA MALINOWSKA, KAROLINA ŚLIWA, ELŻBIETA SIKORA,  
JAN OGONOWSKI\*

## QUALITATIVE ANALYSIS OF THE MAIN POLYPHENOLS CONTAINED IN APPLE POMACE EXTRACT

### ANALIZA JAKOŚCIOWA GŁÓWNYCH POLIFENOLI ZAWARTYCH W EKSTRAKCIE Z WYTŁOKÓW Z JABŁEK

#### Abstract

The paper describes chosen methods for the extraction and qualitative analysis of the main polyphenolic compounds contained in apple pomace. Apple pomace is a by-product generated during apple juice production. The extracts were obtained with the Ultrasound Assisted Micelle Mediated Extraction (UAMME) method using a 1% Rocanol B2 water solution, as well as the Ultrasound Assisted Extraction (UAE) method in water. Thin Layer Chromatography (TLC) and UV/VIS spectroscopy were applied as analytical methods in order to identify the main polyphenolic substances in the obtained extracts. The obtained results showed that both UAMME as well as UAE are effective methods for obtaining quercetin, catechin and rutin.

*Keywords: apple-pomace, ultrasound assisted extraction, micelle mediated extraction, polyphenols, TLC, UV/VIS*

#### Streszczenie

Artykuł opisuje wybrane metody pozyskiwania, a także analizę jakościową głównych związków polifenolowych zawartych w wytlókach z jabłek. Wytłoki jabłkowe stanowią produkt uboczny powstający podczas procesu produkcji soku jabłkowego. Ekstrakty uzyskano metodami ekstrakcji micelarnej wspomaganą ultradźwiękami w 1% wodnym roztworze Rokanolu B2 (UAMME) oraz ekstrakcji wspomaganą ultradźwiękami w wodzie (UAE). Do identyfikacji polifenoli w otrzymanych ekstraktach zastosowano metodę chromatografii cienkowarstwowej (TLC) oraz spektroskopię UV/VIS. Zarówno ekstrakcja micelarna wspomaganą ultradźwiękami, jak i ekstrakcja w wodzie, wspomaganą ultradźwiękami, okazały się skuteczne do pozyskiwania kwercetyny, katechiny oraz rutyny.

*Słowa kluczowe: wytłoki z jabłek, ekstrakcja wspomaganą ultradźwiękami, ekstrakcja micelarna, polifenole, TLC, UV/VIS*

\* M.Sc. Eng. Magdalena Malinowska, M.Sc. Eng. Karolina Śliwa, Ph.D. Eng. Elżbieta Sikora, Prof. Ph.D. Eng. Jan Ogonowski, Organic Chemistry and Technology Institute, Faculty of Chemical Engineering and Technology, Cracow University of Technology.

## 1. Introduction

Since 90's Poland is one of World's greatest producers of concentrated apple juice. Over 70% of fruit trees in orchards are apple trees (Fig. 1).

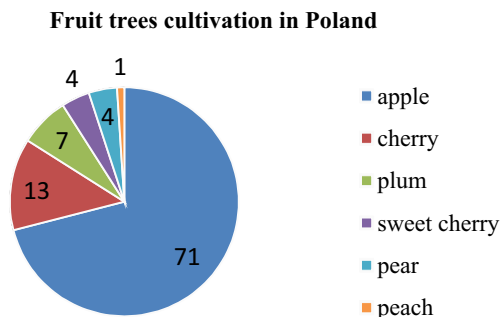


Fig. 1. The structure of fruit tree cultivation in Poland in 2014 [%] [1]

Currently, there are 47 apple processing installations, which operate in Poland, with total productivity of 32 thousand tons of apples a day. It is estimated that about 50–60% of apple fruits are processed in the food industry, mainly for juice concentrate production [1]. During the processing of apple fruits for juice production, large amounts of solid residues, such as peel, core and seeds, are generated [2]. To obtain 200 thousand tons of apple concentrate, about 1.5 million tonnes of apples have to be processed. About 0,3 million tons of residue is treated as a waste [3]. These by-products are called “apple pomace” and are mainly used as feed additives or are disposed of as waste (Fig. 2) [2, 4, 5].



Fig. 2. Dried apple pomace, a by-product of the juice production process

However, many studies show that apple pomace is a rich source of valuable nutraceuticals: carbohydrates, dietary fibres, vitamins, minerals and polyphenols (Fig. 3) [6].

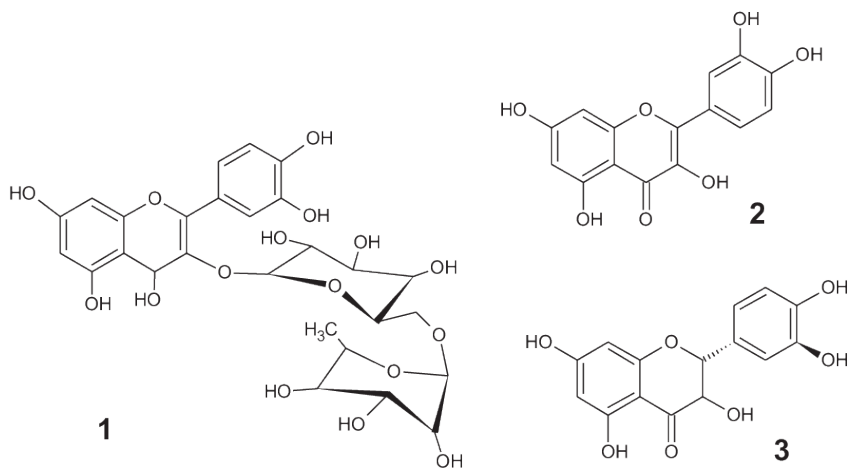


Fig. 3. The structure of the main apple pomace polyphenols: rutin (1), quercetin (2) and catechin (3)

Apple pomace is composed of apple peels, pulp as well as seeds. It is a rich source of valuable biological active compounds, especially with antioxidant activity, e.g. polyphenols, procyanidins or glycosides [7]. After the apple juice extrusion process, only 5% of the pectines, vitamin C and polyphenols contained in a fresh apple remains in the apple juice. Procyanidins are compounds, which remain in the juice at the lowest concentration level. All of the mentioned active substances are bound with apple tissue cells and stays within pomace after the pressing process [8, 9]. Polyphenols are known for their wide range of biological activity [10]. Flavonoids and polyphenolic acids can inhibit the proliferation of cancer cells, which has been proven in many *in vitro* tests. An ethanolic extract from apple pomace, as a rich source of polyphenols, exhibits a very high antioxidant activity, which can be compared to ascorbic acid activity [7]. Because of the presence of triterpene compounds, it can also act as an anti-inflammatory, immune-stimulatory, antiviral, antibacterial and antifungal agent [11]. There are many *in vitro* and *in vivo* experiments confirming the biological and therapeutic activity of apple pomace compounds and the possibility of their application as a valuable source for the pharmaceutical, cosmetic and food industries. In cosmetic products, the apple pomace extracts are used as additives in order to neutralise free radicals and prevent many skin diseases and skin damage [9]. Importantly, in order to obtain a maximum concentration of polyphenols, the apple pomace has to be extracted directly after the extrusion process. The storage of fresh pomace causes changes of its composition and decreases its usability. In order to prevent the fermentation process, apple pomace should be dried-up directly after it is obtained. It can be prepared in the closed technological cycle [12].

## 2. Methodology

Champion apple-pomace was used as the raw material. It was supplied by the Maurer Juice Extraction Plant, Poland. Before extraction, the pomace was dried at 105°C for 90 min. The water content in the pomace was measured using the OHAUS MB25 moisture analyser.

The completely dried apple pomace was ground using a mortar in order to obtain a grounded material with particle sizes below 1 mm.

### 2.1. Extraction process

The extraction processes of dried pomace were conducted according to the following two methods: ultrasound assisted extraction (UAE) and ultrasound assisted micelle-mediated extraction (UAMME). The solvents applied for the extraction processes were: deionised water in the case of UAE method and a 1% water solution of Rokanol B2 (alkoxylated alcohols, C16-18, PCC Exol) in UAMME. The water used was deionised with the Merck Simplicity Milipore water purification system. Dried apple pomaces (10 g each) were extracted in an ultrasonic bath (InterSonic IS-3, frequency 50 Hz, power 300 W) at room temperature for 30 min, using 200 cm<sup>3</sup> of proper solvent.

### 2.2. Qualitative analysis

The identification of polyphenols in the obtained extracts was performed with the TLC analysis. Two different mobile phases, containing chloroform and ethyl acetate (10:1 v/v) – *solution 1* or ethyl acetate, water, formic acid (85:15:0.5 v/v) – *solution 2*, were applied to separate some of the flavonoids occurring in the extracts, i.e. rutin, quercetin and catechin. At the beginning, TLC plates (Polygram Sil G/UV 254, Macherey Nagel) were sprayed with a solution containing anisaldehyde (98%, Sigma Aldrich), acetic acid (99%, POCH), methanol (99.8%, POCH), sulphuric acid (38%, POCH) (0.5:10:85:5 v/v). The extracted ingredients, as well as standards of the flavonoids, triterpenes and polyphenols, become visible after heating the plates at 100°C for 2–3 min. Retention times of the extracted ingredients and standard compounds were compared in order to identify particular spots on the TLC plate. Moreover, UV/VIS spectra were measured for all of the extracts as well as for three standard compounds (catechin, rutin and quercetin). The spectra were prepared in the wavelength range of 200–800 nm, using the Macherey Nagel Nanocolor UV/VIS Spectrophotometer. The obtained absorption spectra for the analysed extracts and standard compounds were compared in order to determine the presence of the polyphenolic compound groups in apple pomace extracts.

## 3. Results

Figure 4 presents the visible spots on TLC plate obtained for two different eluents. Table 1 shows the retention times ( $R_f$ ) of the identified polyphenols. Three of the obtained visible spots on TLC plate: 1, 2 and 3 (Fig. 4), corresponded to the applied standard compounds: rutin, quercetin and catechin. The identified flavonoids are the major polyphenols contained in apple pomace extracts [6, 13].

Figure 5 shows the spectra of the analysed extracts and standard polyphenols. The absorbance maximum, corresponding to the extracts, rutin, quercetin and catechin, is presented in Table 1. The results showed that the extraction procedure influences the concentration of

the analysed polyphenolics. The ultrasound assisted micelle mediated extraction (UAMME) method allowed us to obtain a higher concentration of polyphenols than in the case of the ultrasound-assisted extraction (UAE-E). In case of the extract obtained by UAMME, a higher value of absorption is visible at a wavelength of 210 nm (Fig. 5). The micelles are capable of dissolving organic compounds that are less soluble in the water, such as catechin comparing with rutin, by positioning them inside the micelle structure. Most likely, ingredients that have a slightly lipophilic character are dissolved in water by surface active substance like Rokanol B2 (alkoxylated alcohols C16-18).

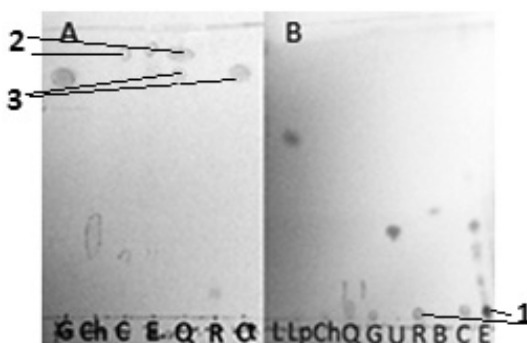


Fig. 4. TLC plates with apple pomace extracts and polyphenolic standard compounds (C, E,-apple pomace extracts, R-rutin, Q-quercetin, G-gallic acid, Ch-chlorogenic acid, L-luteolin, Lp-lupeol, U-ursolic acid, Ct-catechin, B-betulin) – eluent A chloroform : ethyl acetate (10:1 v/v), eluent B – ethyl acetate, water, formic acid (85:15:0,5 v/v)

Table 1

**Polyphenol compounds contained in apple pomace extracts, UAE – Ultrasound Assisted Extraction, UAMME – Ultrasound Micelle Mediated Extraction**

Compound	$R_f$ (solution 1)	$R_f$ (solution 2)	Absorbance max. [nm]
UAE	0.03; 0.06; 0.05	0.08; 0.82; 0.87	212, 250, 260, 360, 370
UAMME	0.03; 0.06; 0.05	0.08; 0.82; 0.90	211, 251, 262, 290, 368
Rutin standard	0.03	0.07	260, 365
Quercetin standard	0.06	0.83	250, 370
Catechin standard	0.05	0.92	210, 290

The obtained results confirmed that both of the applied extraction processes are effective in isolating rutin, quercetin and catechin, but ultrasound-assisted micelle mediated extraction is more efficient for obtaining less hydrophilic substances.

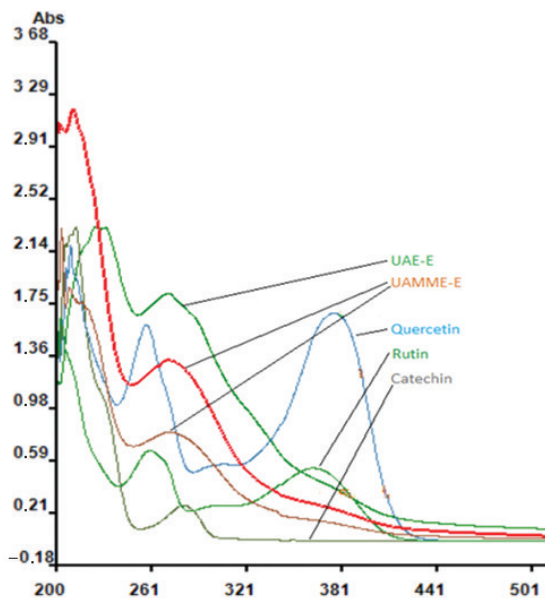


Fig. 5. UV-VIS spectra of apple pomace extracts and polyphenols standards (quercetin, rutin and catechin)

#### 4. Conclusions

The flavonoids (rutin, quercetin and catechin) identified in the obtained extracts are one of the major polyphenols in apple pomace. Both of the applied extraction methods are effective ways for obtaining extracts that are rich in antioxidant polyphenolic compounds. TLC and UV/VIS spectrophotometric methods are useful tools for a qualitative analysis of the extracted polyphenols. Due to presence of antioxidants, the obtained apple pomace extracts can be applied directly as cosmetic raw materials, which are rich in biological active substances.

#### References

- [1] Agencja Rynku Rolnego basing on IERiGZ and GUS data, <http://www.arr.gov.pl> [online 4.05.2015].
- [2] Kołodziejczyk K., *Apple pomace as a source of nutraceutical products*, Pol. J. Food Nutr. Sci., 57, 2001, 291–295.
- [3] Wolfe K., Wu X., Liu R.H., *Antioxidant activity of apple peels*, J. Agric. Food Chem., 51, 2003, 609–661.
- [4] Kennedy M., List L., Lu Y., Foo L.Y., Newman R.H., Sims I. M., Bain P.J.S., Hamilton B., Fenton G., *Apple-pomace and products derived from apple-pomace: Uses, composition and analysis*, in: *Analysis of plant waste materials*, Linskens H. F., Jackson J. F. (eds.) Spriger: Berlin, 1999, 74–119.

- [5] Gullon B., Falque E., Alonso J. L., Parajo J.C., *Evaluation of apple-pomace alternative applications as a raw material for in food industries*. Food Technol. Biotechnol., 45, 2007, 426–433.
- [6] Lu Y., Foo L.Y., *Identification and quantification of major polyphenols in apple pomace*. Food Chem., 59, 1997, 187–194.
- [7] Giomaro et al., *Polyphenols profile and antioxidant activity of skin and pulp of a rare apple from Marche region (Italy)*, Chemistry Central Journal, 8(45), 2014, 1–10.
- [8] Lu Y., Foo L.Y., *Antioxidant and radical scavenging activities of polyphenols from apple pomace*, Food Chem., 68, 2000, 81–85.
- [9] Schieber et al., *Determination of phenolic acids and flavonoids of apple and pear by liquid high-performance chromatography*, J. Chromatography A, 910, 2001, 265–273.
- [10] Eberhardt M.V. et al., *Antioxidant activity of fresh apples*, Nature, 405, 2000, 903–904.
- [11] Grigoros C.G. et al. *Evaluation of apple pomace extracts as a source of bioactive compounds*, Industrial Crops and Products, 49, 2013, 794–804.
- [12] Fronc A., Nawirska A., *Możliwości wykorzystania odpadów z przetwórstwa owoców*, 2(53), 1994, 31–32.
- [13] Denis M.C., Furtos A., Dudonne S., Montoudis A., Garofalo C., Desjardins Y., Delvin E., Levy E., *Apple peel polyphenols and their beneficial actions on oxidative stress and inflammation*, PLOS ONE, 8(1), 2013, e5372.



MARTA MARSZAŁEK, ZYGMUNT KOWALSKI, AGNIESZKA MAKARA\*

## APPLICATION OF PRESSURE-DRIVEN MEMBRANE TECHNIQUES FOR THE RECOVERY OF WATER AND FERTILISING COMPONENTS FROM PIG SLURRY

### ZASTOSOWANIE CIŚNIENIOWYCH PROCESÓW MEMBRANOWYCH DO ODZYSKU WODY ORAZ SKŁADNIKÓW NAWOZOWYCH Z GNOJOWICY TRZODY CHLEWNEJ

#### Abstract

Pig slurry is a by-product of non-bedding pig farming. It is a heterogeneous liquid mixture of faeces, urine, spilt feed and water used for waste removal. As it carries large amounts of organic and biogenic substances, slurry can pose a risk for the natural environment; therefore, it should be properly managed. This paper presents methods for the recovery of water and fertilising components from pig slurry using low-pressure (microfiltration, ultrafiltration) and high-pressure (nanofiltration, reverse osmosis) membrane techniques.

*Keywords: pig slurry, pressure-driven membrane techniques, water recovery, fertilizing components recovery*

#### Streszczenie

Gnojowica świńska jest produktem ubocznym powstającym w warunkach bezściółkowego chowu trzody chlewnej. Stanowi ona niejednorodną płynną mieszaninę kału, moczu, resztek paszy oraz wody używanej do usuwania odchodów. Ze względu na niesiony ładunek substancji organicznych oraz biogennych gnojowica może stwarzać zagrożenie dla środowiska naturalnego, dlatego należy ją właściwie zagospodarować. W artykule przedstawiono metody odzysku wody i składników nawozowych z gnojowicy świńskiej z zastosowaniem nisko- (mikrofiltracja, ultrafiltracja) i wysokociśnieniowych (nanofiltracja, odwrócona osmoza) procesów membranowych.

*Słowa kluczowe: gnojowica świńska, ciśnieniowe procesy membranowe, odzysk wody, odzysk składników nawozowych*

\* M.Sc Eng. Marta Marszałek, Prof. Ph.D Eng. Zygmunt Kowalski, Ph.D Eng. Agnieszka Makara, Institute of Inorganic Chemistry and Technology, Faculty of Chemical Engineering and Technology, Cracow University of Technology.

## 1. Introduction

Pig slurry is a by-product of non-bedding breeding of pigs, both at individual farms and in intensive animal farming. It is a liquid mixture of solid and liquid animal excrement, undigested feed and process water used for maintenance and cleaning purposes in piggeries [1–4]. According to the Polish Act on Fertilisers and Fertilisation [5], slurry is a natural fertiliser and it is recommended to be used as a fertilising material. However, slurry use for fertilisation is characterised by different constraints, mostly attributed to the timing of application (March 1 – November 30) [6] and the recommended doses (170 kg N/ha/year) [5]. As a result, it is almost impossible to effectively use up all of the slurry produced in agriculture. Accordingly, suitable methods have to be employed in order to manage the volume of excess slurry. There are many methods and techniques of separating slurry into solid and liquid fractions [2, 7, 8]. Slurry fractionation is most commonly employed to boost the fertilisation value of slurry and as a pre-treatment measure for composting or anaerobic digestion of slurry. It also helps to limit odour emissions and reduce the costs of slurry storage and handling [7–10]. Sedimentation, pressure filtration, screening, evaporation, flotation, and chemical separation by adding flocculants or coagulants, are the most widely used methods for slurry separation into fractions [7, 8]. As a rule, the liquid fraction produced from either of these processes is further processed using low-pressure (microfiltration, ultrafiltration) and high-pressure (nanofiltration, reverse osmosis) membrane techniques [7–9, 11]. With the rapid technical development in the production of novel generations of membranes, which become increasingly effective and cheaper to produce, the application of membrane techniques for pig slurry processing becomes a technically and economically practicable option [11, 12].

## 2. Composition as well as the physicochemical and microbiological properties of pig slurry

The composition and physicochemical properties of pig slurry may vary significantly depending on the type and age of animals, the used feeding and breeding methods, feed quality, water dilution, and the conditions and period of storage [1–4, 12]. The solid phase of polydisperse slurries is characterised by varied dispersion levels and can be present either as a suspension (coarse-dispersive and colloidal) or as a dispersible form of true solutions. Particle size in solid phase of slurry varies significantly from a few angstroms to 100 millimetres. Roughly 45% of dry mass is made of particles of faeces and undigested feed, 0.2–0.5 mm in size. Over 50% of solid particles are smaller than 50  $\mu$ m, the majority of which are included in the colloidal fraction. The finest colloidal particles account for 9 to 30% of the solid phase. Colloids are the finest particles of faeces, dead and viable microorganisms, mucous substances, humic acids, proteins, and other compounds [1, 3, 4].

A typical pig slurry (Table 1) has a high degree of hydration (6–8% of dry mass on average), is slightly alkaline, contains many suspended solid particles and organic matter, and has a high chemical and biochemical oxygen demand (COD and BOD), as well as high microbial population levels. Pig slurry can include saprophytic bacterial populations, pathogenic bacteria, viruses and fungi, parasite eggs and oocytes. It is also an important

source of fertilising macroelements, most notably nitrogen, phosphorus, potassium, and microelements (iron, boron, zinc, manganese, copper, molybdenum), all of which can be used in agriculture [1–4, 7, 12].

Table 1

**The composition and physicochemical properties of pig slurry acc. to [1–4]**

Parameter	The range of values
pH	7.0–9.5
Dry matter [%]	0.8–11.4
Organic matter [%]	0.6–9.2
COD [mg O <sub>2</sub> /dm <sup>3</sup> ]	10000–26000
BOD <sub>5</sub> [mg O <sub>2</sub> /dm <sup>3</sup> ]	5500–16000
Total nitrogen [mg N <sub>T</sub> /dm <sup>3</sup> ]	1200–5800
Ammonia nitrogen [mg N-NH <sub>4</sub> /dm <sup>3</sup> ]	1600–2700
Phosphorus [mg P/dm <sup>3</sup> ]	460–2000
Potassium [mg K/dm <sup>3</sup> ]	1050–3900
Iron [mg Fe/dm <sup>3</sup> ]	12.0–190.2
Zinc [mg Zn/dm <sup>3</sup> ]	21.9–62.4
Manganese [mg Mn/dm <sup>3</sup> ]	4.55–61.8
Copper [mg Cu/dm <sup>3</sup> ]	3.10–14.0
Boron [mg B/dm <sup>3</sup> ]	1.38–2.23
Molybdenum [mg Mo/dm <sup>3</sup> ]	0.14–0.81

### 3. General characteristics of membrane processes with particular reference to their applicability in the management of pig slurry

With up to a 99% water content, pig slurry can be seen as a valuable source of water. Also, pig slurry is rich in nutrients (mainly nitrogen, phosphorus, potassium) of potential use in the production of fertilisers. In order to recover water and to produce highly concentrated fertilisers using slurry, membrane separation processes need to be combined with other pre-separation processes (sedimentation, screening, centrifugation, filtration with belt, screw or chamber press units, and flotation by addition of flocculants) along the production line [9, 10, 12].

Membrane processes are based on the separation of mixture components, while flowing through a membrane, a thin partition which separates particles and molecules at the molecular or ionic level. The mixture (input stream, feed) is separated into two finished products: a permeate (filtrate – a solution that permeates through the filtration membrane, it contains a solvent with particles that can freely pass through the membrane) and a retentate

(a solution containing substances that did not permeate through the membrane). The flow is driven by the pressure difference on both sides of the membrane. In terms of particle sizes and pressure values, membrane techniques can be classified into low-pressure techniques (microfiltration – MF, ultrafiltration – UF), and high-pressure techniques (nanofiltration – NF, reverse osmosis – RO) [13–17]. Membrane techniques offer a variety of advantages when used for purification purposes, including a continuous separation process at ambient temperature, easy combination of membrane processes and other pre-separation and downstream membrane processes, low energy consumption, absence of chemical agents (and waste streams), a wide choice of highly selective and high-performance membranes, as well as good thermal, chemical and mechanical resistance characteristics. The disadvantages of membrane techniques are the result of the membrane concentration polarisation phenomenon, absorption of macromolecular compounds on the membrane surface, and fouling, i.e. deposition of organic and inorganic pollutants on the surface and in the pores of membranes, thereby limiting membrane permeability [13–17].

In microfiltration, 0.1–10  $\mu\text{m}$  pore size symmetric membranes are used at a 0.1–0.3 MPa trans-membrane pressure, and the separation mechanism is based on the sieve mechanism, where the particle diameter is at play. Microfiltration membranes are made of organic polymers and inorganic materials (ceramic, metals, glass). In the microfiltration process, the solution is purified of colloids, fine suspensions, bacterial cells, spore forms of pathogenic microorganisms, and fine particles of plant materials [7, 11, 13–17]. A trans-membrane pressure within the range of 0.1–0.18 MPa is typically used for slurry purification by microfiltration. Dry mass and phosphorus are largely removed from the obtained permeate (around 75% retention rate), but the permeate still contains dissolved nitrogen and potassium compounds [7].

In ultrafiltration, fractionation and concentration of the selected liquid components are conducted simultaneously by means of porous asymmetrical membranes of 0.005–0.1  $\mu\text{m}$  pore size at 0.3–1 MPa operating pressure. Ultrafiltration membranes allow for passing of monosaccharides, organic acids, and dissociated inorganic ions, while retaining viruses, proteins, polysaccharides, enzymes, vitamins, and some dyes. Similarly to microfiltration, the separation process essentially consists in physical sifting of particles of dissolved or colloidal substances through membranes of suitable porosity characteristics [7, 11, 13–17]. Ultrafiltration membranes are characterised by a molecular weight cut-off value (MWCO), which describes the separation performance and refers to the lowest molecular weight solute in which 90% of the solute is retained by the membrane [13]. In slurry ultrafiltration, the trans-membrane pressure is adapted to the membrane pore size, i.e. the larger the pores, the lower the pressure. As a rule, the maximum trans-membrane pressure is 0.8 MPa. Depending on the ultrafiltration parameters, the process can remove up to 100% of dry mass, and 87% of phosphorus. Still, the permeate may contain a large volume of dissolved ammonium compounds and potassium compounds [7].

The ultrafiltration of selected agricultural waste, including pig slurry, was tested by Reimann and Yeo [18]. Researchers compared inorganic silicon carbide membranes (SiC–0.05 and SiC–0.2) and an organic polyethersulfone membrane (PES-40000) in terms of how the chemical oxygen demand was reduced. The tests were performed under constant pressure (0.2 MPa) and temperature conditions, and with a constant COD concentration in the feed stream. The experiment demonstrated a higher reduction of COD through ultrafiltration of

pig slurry using inorganic membranes (SiC-0.05 and SiC-0.2, by 79 and 33%, respectively) as compared to the PES-40 000 organic membrane (COD reduction by 28%) [18].

Fugere et al. [19] used ultrafiltration to purify pre-treated pig slurry. The study focused on the elimination of bacteria, suspended solids, and phosphorus from the tested samples of pre-treated slurry. The following feed materials were used: supernatant liquid from a storage tank, post-sieving (500  $\mu\text{m}$  pore size) and post-settling manure supernatant, and manure supernatant following sieving, biotreatment, and settling. Polyvinylidene fluoride (PVDF) membranes of 0.01  $\mu\text{m}$  pore size were used for ultrafiltration. Over 99% of suspended solids and *E. coli* bacteria were found to be removed from the pre-treated slurry in the ultrafiltration process. Potassium content and COD were demonstrated to be lower, but the reduction was not fully satisfactory [19].

Lopez-Fernandez et al. [20] used ultrafiltration membranes to remove organic matter from the liquid fraction of pig slurry following anaerobic digestion. Two membrane systems were tested: an external mono-tubular unit (polyethersulfone membrane, 100 kDa cut off) and a submerged hollow fibre membrane module (polyvinylidene fluoride membrane, 0.04  $\mu\text{m}$  pore size). The pig slurry used for tests was filtered (using 0.5 mm screen) and anaerobically digested in an expanded granular sludge bed (EGSB) reactor. The submerged hollow fibre membrane was demonstrated to have higher performance and selectivity in slurry purification. The permeate produced through integrated filtration, anaerobic digestion, and ultrafiltration contained no solid substances, and only negligible amounts of organic matter, achieving a chemical oxygen demand (COD) removal of 90% [20].

Nanofiltration is where univalent ions (sodium or potassium ions) pass through the membrane to a major extent. Nanofiltration membranes have a greater ability to selectively retain divalent and polyvalent ions, and organic compounds larger than 200–400 Da (monosaccharides, enzymes, amino acids). The trans-membrane pressures used in nanofiltration vary from 0.5 to 3 MPa, and the separation process is a combination of sieve mechanisms typical for micro- and ultrafiltration, and dissolution and diffusion typical for reverse osmosis. As a rule, nanofiltration membranes are made of composite materials. The membrane surface is usually negatively charged due to the presence of carboxylic or sulfonic groups. Pore diameters in nanofiltration membranes vary from 0.001 to 0.005  $\mu\text{m}$  [7, 11, 13–17]. Nanofiltration used in slurry management produces a retentate rich in minerals, and a permeate that is essentially free of ammonium ions (rejection rate of 52%) and potassium ions (rejection rate of 78%) [7].

Reverse osmosis is designed to separate low molecular weight compounds from the solvent, using membranes with the pore size of 0.0001–0.001  $\mu\text{m}$  (such dense membranes basically only allow solvents to permeate). The solvent is transmitted in a direction counter to the osmotic pressure, which means high working pressures are used in reverse osmosis, ranging from 1 to 10 MPa. Reverse osmosis membranes operate selectively through the solution–diffusion model, essentially based on the affinity between the membrane and the solution components, and the speed with which they are transferred in the membrane. Reverse osmosis membranes are asymmetrical membranes made of a single polymer (cellulose esters, aromatic polyamides) and composite membranes (polysulfone support, active layer made of polyimides, polybenzimidazole, polybenzimidazolane, polyamide-hydrazide) [7, 11, 13–17]. Reverse osmosis recovers relatively high quality water from the processed slurry, since the large majority of ammonium and potassium ions are retained in the retentate [7].

In order to avoid fouling, the slurry must first be pre-purified before the pressure-driven membrane processes are performed, especially prior to nanofiltration and reverse osmosis. If non-purified slurry is introduced into the process, the used membranes would be clogged very quickly [9, 11, 12, 21].

Lee et al. [21] tested microfiltration (membranes were made of mixed esters of cellulose with the pore size of 0.5  $\mu\text{m}$ ) of digested pig slurry pre-filtered by a stainless steel net with 63  $\mu\text{m}$  pore size (membrane system had a specially designed prefilter made of stainless-steel net). The experiments were intended to determine the causes of fouling and to select the most appropriate fouling prevention in a two-phase anaerobic reactor equipped with a submerged membrane. It was concluded that membrane fouling was caused by sediments of bacterial cells, biological material, and inorganic compounds, mainly calcium and magnesium (e.g. struvite) and sulphates. A stainless steel pre-filter, air backwashing (every 10 minutes for 5 seconds), and chemical cleaning of membranes (every 50 working days), using at first an alkaline solution (1 N NaOH), and after that, an acidic solution (1 N HCl) was introduced to limit fouling. After chemical cleaning, the permeate flux increased greatly, the flux recovery was enhanced up to 89% of a new membrane. Microfiltration tests on pig slurry also demonstrated an 80% COD retention rates of organic impurities [21].

#### **4. Examples of water and fertilising components recovery from pig slurry using low- and high-pressure membrane techniques**

Effective and comprehensive management of excess pig slurry through multi-stage technologies appears to be a viable and reasonable solution. Water recovered in the process can be reused for field irrigation or for the cleaning of farm facilities, which is seen as a particular advantage of this approach. Water reuse would be especially beneficial in areas where water shortage is likely to occur [10, 12, 22–25].

The process of water recovery from pig slurry has been examined in studies by Konieczny and Kwiecińska. In a series of experiments, a number of different separation systems were tested [12, 22–24]. In one of the experiments, the researchers combined centrifugation, two-step ultrafiltration, and nanofiltration. A polyvinylidene fluoride membrane with 100 kDa cut-off at  $p = 0.3$  MPa, and a polyethersulphone membrane with the cut off value of 5 kDa at 0.45 MPa were used in the first-stage and second-stage ultrafiltration, respectively. Nanofiltration was carried out with a hydrophilic composite membrane with 200 Da cut-off at  $p = 3.0$  MPa. The tests demonstrated a 100% and 99% retention rate of organic matter expressed as COD and TOC (total organic carbon), respectively, a 100% reduction of phosphate, sulphate, magnesium and calcium ions, and a 90% reduction of ammonia nitrogen, in the final filtrate. Process water of useable quality was obtained in the process [22].

Konieczny and Kwiecińska [23] also tested water recovery from pig slurry by integrating cloth filtration, two-step ultrafiltration, and nanofiltration. A polyvinylidene fluoride membrane with 100 kDa cut-off, and a polyethersulphone membrane with the cut off value of 10 kDa were used in the first-stage and second stage of the filtration process, respectively. A nanofiltration polyamide membrane with a 30-50% retention ratio of chlorides was used for post-purification. It was demonstrated that the content of organic impurities expressed as

COD and TOC was progressively reduced by 99%, which makes it clear that the designed system may be applied in water recovery from pig slurry. A significant reduction in the content of total nitrogen (by 90%) and ammonium ions (by 89%) was confirmed following nanofiltration [23].

Konieczny and Kwiecińska [24] also employed an integrated slurry processing system consisting of ultrafiltration and two-step reverse osmosis. The feed for the low-pressure membrane treatment was obtained through the natural processes of sedimentation and floatation. A pilot system was designed for ultrafiltration, fitted with ceramic tubular membranes (with the pore size of 5 nm) at 0.3 MPa. Polyamide reverse osmosis membranes were used for two-stage purification at 2.0 MPa. The recovered water was eligible for reuse in cooling and heating systems, or for cleaning and housekeeping work at the farm. The content of phosphate and sulphate ions was reduced by 100%, total nitrogen – by 95%, and organic impurities expressed as COD and TOC – by 99% [24].

Pieters et al. [25] used membrane techniques to process sow slurry with a dry mass content of 1.5–2%. At first, the slurry was separated into solid and liquid fractions by sedimentation. The obtained liquid fraction was purified by bag filtration (100 µm pore size), followed by microfiltration on ceramic membranes (0.1 µm pore size). The obtained microfiltrate was injected onto a system of osmotic membranes made of polysulfone support and polyamide active layer, covering an area of 6.5 m<sup>2</sup>. To reinforce the effectiveness of pig slurry purification, microfiltration and reverse osmosis were rerun. Purified liquid fraction did not contain any dry mass and suspended solids and only very little minerals and COD (5 mg/dm<sup>3</sup>). The recovered water may be used for field irrigation and drained into the sewerage network [25].

Zhang et al. [10] tested water recovery from pig slurry using a laboratory-scale wastewater treatment system. The system consisted of the following elements: an anaerobic sequencing batch reactor (ASBR), two aerobic sequencing batch reactors (SBR), a sludge settling tank, a sand filter, and a reverse osmosis unit (two types of spiral-wound membranes with 99.4% and 98.5% NaCl retention rates). Two types of pre-treated pig slurry were introduced into the system: the first one processed by anaerobic digestion, single-stage aerobic digestion, and filtration, and the second one processed by anaerobic digestion, two-stage aerobic digestion, and filtration. Osmotic membranes proved to be very effective in separating nutrients and dissolved salts from water, and the obtained permeate was demonstrated to be of high quality. The results of the study indicate markedly that both types of membranes tested retain over 70% of ammonia nitrogen, nitrates and nitrites, and over 90% of potassium, phosphorus, calcium, magnesium, sodium, iron, zinc, and copper ions. The obtained retentate accounts for 10% of the baseline volume of the feed material and may be used as a liquid fertiliser [10].

Table 2 presents the characteristics of water recovery from pig slurry. The research results (water quality, costs of process, applicability of process) are difficult to compare because of the differences in the composition of the slurry used for experiments, the pre-treatment of slurry samples, and the type and conditions of the membrane process. Moreover, sometimes the data are not complete or different analyses were performed. However, in all experiments, the resulting water is suitable for re-use and its contaminant indicator values are significantly reduced compared to the feed material.

Characteristics of processes of water recovery from pig slurry

References	Characteristics of the membrane process	Preparation of the feed material	Characteristics of the feed material	Permeate characteristics
Zhang et al. 2004 [10]	RO, two types of spiral-wound membranes with 99.4% and 98.5% NaCl retention rates, and the total membrane area of 2.51 [m <sup>2</sup> ] and 1.77 [m <sup>2</sup> ], respectively	Pre-processed slurry (filtrated, diluted, with an addition of urea) is subjected to the following processes: a) anaerobic digestion, aerobic digestion, sand filter purification b) anaerobic digestion, two-step aerobic digestion, sand filter purification	unavailable data	unavailable data
Kwiecińska and Konieczny 2011 [22]	UF, polyvinylidene fluoride (PVDF) membrane with the cut off value of 100 [kDa], $p = 0.3$ [MPa]	Centrifuged pig slurry (10 minutes, 15 000 [rpm])	COD = 3785 [mg/dm <sup>3</sup> ] $N_T = 2950$ [mg/dm <sup>3</sup> ] $PO_4^{3-} = 34.6$ [mg/dm <sup>3</sup> ]	COD = 2990 [mg/dm <sup>3</sup> ] $N_T = 2950$ [mg/dm <sup>3</sup> ] $PO_4^{3-} = 32.2$ [mg/dm <sup>3</sup> ]
	UF, polyethersulphone membrane with the cut off value of 5 kDa, $p = 0.45$ [MPa]	Permeate following first-step ultrafiltration	COD = 2990 [mg/dm <sup>3</sup> ] $N_T = 2950$ [mg/dm <sup>3</sup> ] $PO_4^{3-} = 32.2$ [mg/dm <sup>3</sup> ]	COD = 2285 [mg/dm <sup>3</sup> ] $N_T = 2950$ [mg/dm <sup>3</sup> ] $PO_4^{3-} = 24.7$ [mg/dm <sup>3</sup> ]
	NF, hydrophilic composite membranes with the cut off value of 200[Da], $p = 3.0$ [MPa]	Permeate following second-step ultrafiltration	COD = 2285 [mg/dm <sup>3</sup> ] $N_T = 2950$ [mg/dm <sup>3</sup> ] $PO_4^{3-} = 24.7$ [mg/dm <sup>3</sup> ]	COD = 13.9 [mg/dm <sup>3</sup> ] $N_T = 148$ [mg/dm <sup>3</sup> ] $PO_4^{3-} = 0$ [mg/dm <sup>3</sup> ]
Konieczny and Kwiecińska 2011 [23]	UF, polyvinylidene fluoride (PVDF) membrane with the cut off value of 100 [kDa], $p = 0.3$ [MPa]	Pig slurry following cloth filtration (laboratory filter press)	COD=20 400 [mg/dm <sup>3</sup> ] $N_T = 3130$ [mg/dm <sup>3</sup> ]	COD = 5120 [mg/dm <sup>3</sup> ] $N_T = 3130$ [mg/dm <sup>3</sup> ]
	UF, polyethersulphone membrane with the cut off value of 10 [kDa], $p = 0.5$ [MPa]	Permeate following first-step ultrafiltration	COD = 5120 [mg/dm <sup>3</sup> ] $N_T = 31300$ mg/dm <sup>3</sup> ]	COD = 3615 [mg/dm <sup>3</sup> ] $N_T = 2450$ [mg/dm <sup>3</sup> ]
	NF, polyamide membrane, chloride retention ratio of 30-50%, $p = 3.0$ [MPa]	Permeate following second-step ultrafiltration	COD = 3615 [mg/dm <sup>3</sup> ] $N_T = 2450$ [mg/dm <sup>3</sup> ]	COD = 150 [mg/dm <sup>3</sup> ] $N_T = 320$ [mg/dm <sup>3</sup> ]

Kwiecińska and Koniczny 2013 [24]	UF, ceramic tubular membrane, 5 [mm] pore size, $p = 0.3$ [MPa]	Pig slurry following natural sedimentation and flotation	COD=29 000 [mg/dm <sup>3</sup> ] $N_T = 2367$ [mg/dm <sup>3</sup> ] $PO_4^{3-} = 1894$ [mg/dm <sup>3</sup> ]	COD = 18 000 [mg/dm <sup>3</sup> ] $N_T = 1560$ [mg/dm <sup>3</sup> ] $PO_4^{3-} = 1217$ [mg/dm <sup>3</sup> ]
	RO, polyamide flat-sheet membranes, $p = 2.0$ [MPa]	Permeate following first-stage ultrafiltration	COD = 18 000 [mg/dm <sup>3</sup> ] $N_T = 1560$ [mg/dm <sup>3</sup> ] $PO_4^{3-} = 1217$ [mg/dm <sup>3</sup> ]	COD = 953 [mg/dm <sup>3</sup> ] $N_T = 178$ [mg/dm <sup>3</sup> ] $PO_4^{3-} = 15$ [mg/dm <sup>3</sup> ]
	RO, polyamide flat-sheet membranes, $p = 2.0$ [MPa]	Permeate following reserve osmosis	COD = 953 [mg/dm <sup>3</sup> ] $N_T = 178$ [mg/dm <sup>3</sup> ] $PO_4^{3-} = 15$ [mg/dm <sup>3</sup> ]	COD < 5 [mg/dm <sup>3</sup> ] $N_T = 9$ [mg/dm <sup>3</sup> ] $PO_4^{3-} = 0$ [mg/dm <sup>3</sup> ]
Pieters et al. 1999 [25]	MF, ceramic membranes made of Al <sub>2</sub> O <sub>3</sub> (0.1 μm pore size), with a specific membrane surface area of 3 [m <sup>2</sup> ]	Sow slurry, 1.5–2% dry mass content, subject to sedimentation and bag filtration (100 [μm] pore size)	COD = 4700 [mg/dm <sup>3</sup> ] $N_{Kjeldahl} = 1585$ [mg/dm <sup>3</sup> ] $P_2O_5 = 240$ [mg/dm <sup>3</sup> ]	COD = 3800 [mg/dm <sup>3</sup> ] $N_{Kjeldahl} = 1415$ [mg/dm <sup>3</sup> ] $P_2O_5 = 200$ [mg/dm <sup>3</sup> ]
	RO, composite membrane including polysulfone support and polyamide top layer (0.1–0.2 [μm] pore size) with a specific membrane surface area of 6.5 [m <sup>2</sup> ]	Permeate obtained by microfiltration	COD = 3800 [mg/dm <sup>3</sup> ] $N_{Kjeldahl} = 1415$ [mg/dm <sup>3</sup> ] $P_2O_5 = 200$ [mg/dm <sup>3</sup> ]	COD = 5 [mg/dm <sup>3</sup> ] $N_{Kjeldahl} = 240$ [mg/dm <sup>3</sup> ] $P_2O_5 = 9$ [mg/dm <sup>3</sup> ]

The recovery of nutrients in the form of concentrates from pig slurry is no less interesting, as it can produce a valuable fertilising material, which is much more convenient to transport and store than slurry. This can be achieved by designing processing lines made of low- and high-pressure membrane processes [9, 26–28].

Mondor et al. [26] attempted to obtain concentrated nitrogen fertilisers from pig slurry using electrodialysis and reverse osmosis. In the first phase of the research, the slurry was processed by vacuum filtration. The obtained filtrate was introduced to an electrodialysis unit (made of a dimensionally stable anode and a stainless steel cathode). At a subsequent stage of the investigation, following electrodialysis, the concentrate was fed into a membrane unit with reverse osmosis membranes (polyamide membranes of 99.6% NaCl retention rates). Following reverse osmosis, the concentrate accounted for around 46% of the baseline volume of the feed material, and contained 92% dry mass and 67% ammonia nitrogen. The maximum ammonia nitrogen concentration was 13 g/dm<sup>3</sup>. The permeate accounted for around 50% of the baseline volume of the feed material and contained 3% dry mass and 9% ammonia nitrogen. Throughout the experiment (both in the course of electrodialysis and reverse osmosis), researchers observed losses of ammonia nitrogen, which means the production techniques of concentrated nitrogen fertilisers from pig slurry using electrodialysis and reverse osmosis need to be further improved [26].

Hoeksma et al. [27] monitored five full-scale manure processing plants, where mineral concentrates from pig slurry were produced. Reverse osmosis was the final processing stage. The observation lasted for 2 years. The production process included slurry separation into fractions by the addition of a coagulant (Fe<sub>2</sub>(SO<sub>4</sub>)<sub>3</sub>) and a flocculant (polyacrylamide), a filtration unit with a belt or screw press, suspended solids and colloidal particles removal unit from the liquid fraction of slurry using dissolved air floatation, and a reverse osmosis unit (with membranes designed for seawater desalination). The mass of concentrates obtained by reverse osmosis, and of permeates, ranged from 30 to 50%, and from 25 to 56% of that of raw pig slurry at baseline, respectively. The concentrates contained 50% of total nitrogen, 78% of potassium, and 5% of phosphorus contained in the slurry at baseline, on average. Permeates contained 2% of total nitrogen and 3% of potassium originally contained in the slurry, on average, and were eligible to be disposed to the drainage system. If further purified, they can be disposed into surface water. The mineral concentrates can be classified as nitrogen-potassium fertilisers as they contain 7.1 g/kg of nitrogen, and 7.8 g/kg of potassium, on average [27].

Thorneby et al. [9] used reverse osmosis to concentrate slurry from fattening pigs. Liquid fraction obtained by slurry sedimentation and filtration with a 100 µm pore size was used in the experiment. It was processed on a pilot system fitted with a tubular unit (a composite polyamide membrane of 99% NaCl retention rate). Through reverse osmosis, the volume of the liquid fraction was reduced by around 60% of the original volume of slurry. 98% phosphorus and COD, and 93–97% ammonia nitrogen retention rates were demonstrated. The permeate was eligible for use in cleaning and housekeeping or, when neutralised and disinfected, for watering animals [9].

N-Free® system [28] is an example how pig slurry can be comprehensively managed. It recovers water and nutrients, most notably nitrogen, from pre-digested slurry. N-Free® consists of several stages of physicochemical treatment (slurry separation using screw press separator, polyamide-based flocculants, and decanter centrifuge, ultrafiltration, reverse

Table 3

Characteristics of processes of fertilising components recovery from pig slurry

References	Characteristics of the membrane process	Preparation of the feed material	Characteristics of the feed material	Retentate characteristics
Thorneby et al. 1999 [9]	RO, polyamide tubular membranes, 99% NaCl retention ratio, membrane area of 0.9 [m <sup>2</sup> ]	Slurry from fattening pigs subjected to sedimentation and filtration (100 [µm] pore size)	unavailable data	unavailable data
Mondor et al. 2008 [26]	RO, polyamide filtration, 99,6% NaCl retention ratio, $p = 5.5$ [MPa]	Pig slurry subjected to vacuum filtration and electro dialysis	N-NH <sub>3</sub> = 8.74 [g/dm <sup>3</sup> ]	N-NH <sub>3</sub> = 12.84 [mg/dm <sup>3</sup> ]
Hoeksma et al. 2012 [27]	RO, membranes designed for seawater desalination	Fattener and sow slurries and their mixtures subjected to coagulation (Fe <sub>2</sub> (SO <sub>4</sub> ) <sub>3</sub> )/flocculation (polyacrylamide), filtration on belt/screw filter press, and dissolved air flotation	$P = 0.04-0.14$ [g/kg] $K = 2.25-3.86$ [g/kg] $N_T = 1.94-4.27$ [g/kg]	$P = 0.01-0.34$ [g/kg] $K = 5.53-8.44$ [g/kg] $N_T = 4.16-8.92$ [g/kg]
Ledda et al. 2013 [28]	UF, polyacrylonitrile membrane with the cut off value of 40 [kDa]	Digested pig slurry separated on a screw press, flocculated (polyacrylamide), and centrifuged (decanter centrifuge)	$P = 0.05$ [g/kg] $K = 2.24$ [g/kg] $N_{Kjeldahl} = 2.19$ [g/kg]	$P = 0.26$ [g/kg] $K = 2.23$ [g/kg] $N_{Kjeldahl} = 2.94$ [g/kg]
	RO	Permeate following first-step ultrafiltration	$P = 0.04$ [g/kg] $K = 2.34$ [g/kg] $N_{Kjeldahl} = 1.88$ [g/kg]	$P = 0.15$ [g/kg] $K = 7.69$ [g/kg] $N_{Kjeldahl} = 7.41$ [g/kg]

osmosis, permeate post-purification on a zeolite bed, ammonia removal from the retentate using a cold stripping unit, and ammonia converting into sulphate salt) and is intended to produce clean water, liquid ammonium sulphate, solid fraction, and liquid concentrates rich in minerals. Ledda et al. [28] monitored the process on a full technical scale. Around 49% of the baseline pre-digested slurry can be recovered as clean water, 12% of it can be recovered as a solid fraction rich in organic matter, phosphorus, and nitrogen, and the remaining 37% is a liquid concentrate rich in ammonia nitrogen, phosphorus and potassium. A liquid fraction of centrifuged pig slurry was used for ultrafiltration on a grafted polyacrylonitrile membrane with a cut-off value of 40 kDa. The content of phosphorus, total solids, and Kjeldahl nitrogen was significantly reduced by 43%, 37% and 31%, respectively. The obtained filtrate underwent reverse osmosis treatment to obtain a permeate, which was free of phosphorus and potassium. 97% retention rates of ammonia nitrogen and Kjeldahl nitrogen as well as total solids were demonstrated [28].

Table 3 presents the characteristics of fertilising components recovery from pig slurry. It is not possible, however, to fully compare data from these studies (quality and hazard of obtained fertiliser material, possibility of using of concentrated fraction, cost-effectiveness of process) because of the differences in the physicochemical properties of pig slurry used for experiments, and in the pre-treatment of the feed material, membrane type, and process conditions. Moreover, sometimes the data are not complete or different analyses were performed. However, similar average concentrations of phosphorus, potassium and nitrogen in retentates after the reverse osmosis process were reported by Ledda et al. [28] and by Hoeksma et al. [27].

## 5. Conclusions

Pig slurry produced in non-bedding farming of pigs requires proper management. Membrane filtration is an important element of slurry separation and purification. Low-pressure membrane techniques (microfiltration and ultrafiltration) eliminate macromolecular organic compounds, suspensions, colloids, as well as bacteria and viruses, to produce a microbiologically safe filtrate. High-pressure membrane techniques (nanofiltration and reverse osmosis) retain impurities at the ion level, in order to produce high-quality water. When membrane techniques are used for post-purification of liquid fraction of pig slurry, the values of COD and BOD<sub>5</sub> as well as the contents of carbon, ammonia nitrogen, Kjeldahl nitrogen, and phosphorus were shown to be significantly reduced. Water recovered from slurry by membrane filtration may be used for field irrigation, for cleaning and housekeeping works at the farm, and in cooling and heating systems. When neutralised and disinfected, this water can be disposed into surface water or used for watering the animals. The concepts of excess slurry management featuring membrane techniques (reverse osmosis in particular) also offer the opportunity to recover and concentrate fertilising components, mainly nitrogen and potassium. By producing liquid concentrates of minerals, a fertilising material can be produced that is eligible for use in agriculture, thereby, limiting the consumption of mineral fertilisers. Another advantage of this process is that the final products, occupying much less space than the original slurry, are much easier to store and transport.

## References

- [1] Kutera J., *Gospodarka gnojowicą*, Wydawnictwo Akademii Rolniczej we Wrocławiu, 1994.
- [2] Gorlach E., Mazur T., *Chemia rolna*, PWN, 2001.
- [3] Kutera J., Hus S., *Rolnicze oczyszczanie i wykorzystanie ścieków i gnojowicy*, Wydawnictwo Akademii Rolniczej we Wrocławiu, 1998.
- [4] Hus S., *Chemia wody, ścieków i gnojowicy*, Wydawnictwo Akademii Rolniczej we Wrocławiu, 1995.
- [5] Ustawa z dnia 10 lipca 2007 r. o nawozach i nawożeniu, Dz.U. 2007 nr 147 poz. 1033.
- [6] Załącznik do rozporządzenia Rady Ministrów z dnia 14 kwietnia 2004, Dz. U. Nr 73, poz. 657.
- [7] Hjorth M., Christensen K.V., Christensen M.L., Sommer S.G., *Solid-liquid separation of animal slurry in theory and practice. A review*. *Agronomy for Sustainable Development*, 30, 2010, 153–180.
- [8] Burton, C.H., *The potential contribution of separation technologies to the management of livestock manure*, *Livestock Science*, 112, 2007, 208–216.
- [9] Thorneby L., Persson K., Tragardh G., *Treatment of liquid effluents from dairy cattle and pigs using reverse osmosis*, *Journal of Agricultural Engineering Research*, 73, 1999, 159–170.
- [10] Zhang R.H., Yang P., Pan Z., Wolf T.D., Turnbull J.H., *Treatment of swine wastewater with biological conversion, filtration, and reverse osmosis: A laboratory study*, *American Society of Agricultural Engineers*, vol. 47(1), 2004, 243–250.
- [11] Masse L., Masse D.I., Pellerin Y., *The use of membranes for the treatment of manure: a critical literature review*, 98, 2007, 371–380.
- [12] Konieczny K., Kwiecińska A., Gworek B., *The recovery of water from slurry produced in high density livestock farming with the use of membrane processes*, *Separation and Purification Technology*, 80, 2011, 490-498.
- [13] Bodzek M., Bohdziewicz J., Konieczny K., *Techniki membranowe w ochronie środowiska*, Wydawnictwo Politechniki Śląskiej, 1997.
- [14] Biernacka E., Suchecka T., *Techniki membranowe w ochronie środowiska*, Wydawnictwo SGGW, 2004.
- [15] Kowal A.P., Świdarska-Bróz M., *Oczyszczanie wody*, PWN, 2003.
- [16] Anielak A.M., *Chemiczne i fizykochemiczne oczyszczanie ścieków*, PWN, 2002.
- [17] Łomotowski J., Szpindor A., *Nowoczesne systemy oczyszczania ścieków*, Wydawnictwo Arkady, 2002.
- [18] Reimann W., Yeo I., *Ultrafiltration of agricultural waste waters with organic and inorganic membranes*, *Desalination*, 109, 1997, 263-267.
- [19] Fugere R., Mameri N., Gallot J.E., Comeau Y., *Treatment of pig farm effluents by ultrafiltration*, *Journal of Membrane Science*, 255, 2005, 225–231.
- [20] Lopez-Fernandez R., Aristizabal C., Irusta R., *Ultrafiltration as an advanced tertiary treatment of anaerobically digested swine manure liquid fraction: A practical and theoretical study*, *Journal of Membrane Science*, 375, 2011, 268–275.

- [21] Lee S.M., Jung J.Y., Chung Y.C., *Novel method for enhancing permeate flux of submerged membrane system in two-phase anaerobic reactor*, Water Research, 35, 2001, 471–477.
- [22] Kwiecińska A., Konieczny K., *Recovery of industrial water from pig liquid manure by means of membrane techniques*, Ecological Chemistry and Engineering A, Vol. 18, No. 12, 2011, 1743–1750.
- [23] Konieczny K., Kwiecińska A., *Odzysk wody z gnojowicy trzody chlewnej – wyniki badań laboratoryjnych*, Inżynieria Ekologiczna, 24, 2011, 81–88.
- [24] Kwiecińska A., Konieczny K., *Application of membrane processes in treatment of slurry from high-density pig farming*, Ecological Chemistry Engineering A, Vol. 20, No. 2, 2013, 239–249.
- [25] Pieters J.G., Neukermans G.G.J., Colanbeen M.B.A., *Farm-scale membrane filtration of sow slurry*, Journal of Agricultural Engineering Research, 73, 1999, 403–409.
- [26] Mondor M., Masse L., Ippersiel D., Lamarche F., Masse D.I., *Use of electrodialysis and reverse osmosis for the recovery and concentration of ammonia from swine manure*, Bioresource Technology, 99, 2008, 7363–7368.
- [27] Hoeksma P., de Buissonje F.E., Aarnink A.A., *Full-scale production of mineral concentrates from pig slurry using reverse osmosis*, Vol. 4489, 2007, 726–734.
- [28] Ledda C., Schievano A., Salati S., Adani F. u M.K., *Nitrogen and water recovery from animal slurries by a new integrated ultrafiltration, reverse osmosis and cold stripping process: A case study*, 47, 2013, 6157–6166.

MAŁGORZATA MIASTKOWSKA, ELŻBIETA SIKORA,  
JAN OGONOWSKI\*

## NANOEMULSIONS BASED ON SELECTED BERRY SEED OILS

### NANOEMULSJE NA BAZIE WYBRANYCH OLEJÓW Z NASION OWOCÓW JAGODOWYCH

#### Abstract

The aim of this work was the preparation of O/W nanoemulsions based on supercritical CO<sub>2</sub> extracted (SC-CO<sub>2</sub>) oils from seeds of strawberry and blackcurrant. The emulsion systems were obtained by the phase inversion composition method, at  $T = 25^{\circ}\text{C}$ . Polysorbate 80 and Natragem S150 were used as the surfactant and co-surfactant, respectively. Kinetic stability of the prepared formulations with varying surfactant: oil (S:O) and surfactant/co-surfactant (S/CoS) weight ratio, was analysed by measuring the droplet size (DLS method) in time. The obtained results show that a nanoemulsion based on blackcurrant seed oil was characterised by the smallest droplet size ( $r = 15$  nm), a low polydispersity index (PDI = 0.246) and the longest kinetic stability (S:CoS = 8:2, S/CoS:O = 9:1).

*Keywords: nanoemulsions, blackcurrant seed oil, strawberry seed oil supercritical CO<sub>2</sub> extraction*

#### Streszczenie

Celem pracy było otrzymanie nanoemulsji O/W, w których rolę fazy olejowej pełnił ekstrakt z nasion truskawki lub czarnej porzeczki otrzymany w warunkach nadkrytycznego CO<sub>2</sub> (SC-CO<sub>2</sub>). Układy emulsyjne otrzymano metodą składnikowej inwersji faz, w  $T = 25^{\circ}\text{C}$ . Jako surfaktant zastosowano Polisorbat 80, rolę kosurfaktantu pełnił Natragem S150. Kinetyczną stabilność otrzymanych formułacji badano poprzez pomiar wielkości cząstek nanoemulsji (technika DLS) w czasie, dla układów o różnym stosunku wagowym surfaktant: olej (S:O) oraz surfaktant/kosurfaktant (S/CoS). Otrzymane rezultaty wykazały, że najmniejszym rozmiarem cząstek fazy wewnętrznej ( $r = 15$  nm), niskim indeksem polidispersyjności (PDI = 0.246) oraz najdłuższą kinetyczną stabilnością charakteryzowała się nanoemulsja na bazie oleju z nasion czarnej porzeczki (S:CoS = 8:2, S/CoS:O = 9:1).

*Słowa kluczowe: nanoemulsje, olej z nasion czarnej porzeczki, olej z nasion truskawki, ekstrakcja nadkrytycznym CO<sub>2</sub>*

\* Ph.D. Eng. Małgorzata Miastkowska, Ph.D. Eng. Elżbieta Sikora, Prof. Ph.D. Eng. Jan Ogonowski, Institute of Inorganic Chemistry and Technology, Faculty of Chemical Engineering and Technology, Cracow University of Technology.

## Abbreviations

W	– water
O	– oil
S	– surfactant
CoS	– co-surfactant
S/CoS	– surfactant/co-surfactant
oil–S/CoS:O	– surfactant/co-surfactant
oil–S:O	– surfactant
O/W	– oil/water
W/O	– water/oil
NE	– nanoemulsion
SC–CO <sub>2</sub>	– supercritical carbon dioxide
PIC	– phase inversion composition
DLS	– Dynamic Light Scattering
OP	– blackcurrant seed oil
OT	– strawberry seed oil
OO	– olive oil
PDI	– polydispersity index

## 1. Introduction

Natural oils are a valuable source of active substances, e.g. unsaturated fatty acids and tocopherols. Unsaturated fatty acids are responsible for the proper construction of the intercellular cement of the *stratum corneum*. They reduce transepidermal water loss (TEWL), and thereby, assure the proper functioning of the epidermis. Tocopherols are natural antioxidative agents and intercellular membrane structures [1].

Nanoemulsions can be defined as ‘ultrafine’ or ‘submicron emulsions’ because of the small droplet size, in the range of 20 to 500 nm. They are used in personal care products as potential vehicles for the controlled delivery of active agents. The nanoemulsions are valued forms in skin care because of their good sensorial properties, i.e. rapid penetration, fluid textures and their biophysical properties [2, 3].

In studies concerning nanoemulsions, most authors used the following as an oil phase: mineral oil [4], decan [5], hexadecane [6], isopropyl mirystate [7, 8] or medium chain triglycerides [9–12]. Recently, there has been increasing interest in natural oils, such as castor oil [13], soybean oil [14, 15], canola oil [16], rice brain oil [17], grape seed oil [18] and olive oil [19].

As it appears from the literature review, there is no information about nanoemulsions containing strawberry seed oil or blackcurrant seed oil as the oil phase. From the cosmetic point of view, they are very valuable raw materials. Strawberry seed oil is a natural active ingredient, which is characterised by good oxidative stability, high biological activity and a gentle anti-wrinkle active. It consists mainly of C18:1 (15%), C18:2 (45%), C18:3 (35%) [20–22].

Blackcurrant seed oil is a valuable nutritional oil and a rich source of GLA. It is composed of C18:0 (3%), C18:1 (40%), C18:2 (45%) and C18:3 (12%) [21]. Due to its special features, it can promote healthier-looking skin and act as a moisturiser [20].

The studies on obtaining oil from the seeds of berries (including strawberry, blackcurrant, blackberry), through the extraction with supercritical carbon dioxide (SC-CO<sub>2</sub>), have been conducted for several years. Carbon dioxide is non-toxic, non-explosive, readily available and easily removed from the extracted products. Supercritical CO<sub>2</sub> extraction is often carried out at a mild temperature, in the absence of oxygen. Due to this fact, it is possible to avoid thermal and oxidative damage of the bioactive compounds in the extract. Moreover, SC-CO<sub>2</sub> extraction is an environment-friendly process. The advantages of oils obtained under supercritical fluids over oils separated by other methods are: reproducible and stable quality of the oils, and high process efficiency [23, 24].

The aim of this work was to prepare (by low energy emulsification method) and characterise highly dispersed emulsion systems, containing oil phase supercritical CO<sub>2</sub> (SC-CO<sub>2</sub>) extracted from the seeds of strawberry and blackcurrant, for a potential cosmetic application.

## 2. Materials and methods

### 2.1. Materials

The raw materials used in the studies are shown at Table 1. Distilled water was used as the aqueous phase of the emulsions. The applied surfactants Polysorbate 80 (P80) and Natragem S150 (N150) were selected for the studies because of their high HLB value (HLB = 15.0). Ostertag and co-workers [25] found that, in the case of nanoemulsions based on natural oils, the smallest particle size was achieved when the surfactant had an intermediate HLB value of around 15,0 [25]. Additionally, both of the used emulsifiers are non-ionic surfactants known from their good dermatological characteristics, and in the case of Natragem S150, for its natural origin.

Berry seed oils were applied as the oil phase in the prepared systems; similarly to olive oil, which was used for comparison purposes.

Table 1

Raw materials used in the studies

Raw material	INCI name	Role	Producer
Polysorbate 80	Polysorbate 20	Emulsifier (HLB = 15.0)	Caesar&Loretz GmbH
Natragem S150	Polyglyceryl-4 Laurate/Sebacate (and) Polyglyceryl-4 Caprylate/Caprata (and) Water	Emulsifier (HLB = 15.0)	Croda Poland
Blackcurrant seed oil	Ribes Nigrum (Blackcurrant) Seed Oil	Oil phase	INS Puławy
Strawberry seed oil	Fragaria Ananassa (Strawberry) Seed Oil	Oil phase	INS Puławy
Olive oil	Olea Europaea (Olive) Fruit Oil	Oil phase	Ol'Vita

## 2.2. Formation of emulsion systems

Nanoemulsions were prepared using the phase inversion composition (PIC) method, by the gradual addition of water (W) into the mixture of oil (O) and surfactant (S)/co-surfactant (CoS) or to the mixture of oil and surfactant (S), at ambient temperature (25°C). The weight ratios of surfactant or the blends of surfactants to oils were varied as 9:1, 8:2, 7:3, 6:4 and 5:5. Also, the weight ratios of S surfactant to co-surfactant S/CoS used in the compositions were different as 9:1, 8:2 and 7:3.

## 2.3. Construction of a phase diagrams

Pseudo-ternary phase diagrams were constructed in the following way: mixtures of surfactant:oil (S:O) or surfactant/co-surfactant:oil (S/CoS:O) were titrated by water, at 25°C. The compositions were considered as nanoemulsions, when they were transparent and translucent, showing a bluish shine. It was confirmed that they were not microemulsions, as their properties depended on the preparation method and the storage temperature.

## 2.4. Droplet size determination

The average internal phase droplet size of the emulsions was measured by the Dynamic Light Scattering (DLS) method, using Malvern Zetasizer Nano ZS device. The measurements of particle size, which ranged from 0.3 nm to 10 µm, were based on scattering photons from a sample and determined by the change in the diffracted light intensity. The scattering angle was 173°.

## 2.5. Kinetic stability measurement

The emulsions stability was assessed by measuring droplet size as a function of time at a constant temperature (25°C). Moreover, the samples were stored at ambient temperature for 48 hours, for one week and for one month. The stability of the formulations was also assessed visually.

## 3. Results and discussion

In the first stage of the studies, blackcurrant (OP) and strawberry seed (OT) oils, obtained by the supercritical CO<sub>2</sub> extraction method, were tested in order to obtain stable nanoemulsion systems. The olive oil (OO) was also used at the studies as the reference attempt. All formulations were prepared by low energy emulsification method, by dropwise addition of water to the mixture of surfactant:oil or surfactant/co-surfactant:oil. The ratios of surfactant to oil (S:O) or surfactant/co-surfactant to oil (S/CoS:O) were varied as 9:1, 8:2, 7:3, 6:4 and 5:5. Surfactant and co-surfactant (S/CoS) were also blended at different weight ratio (9:1, 8:2, 7:3). The compositions and characteristics of some of the obtained systems are shown at Table 2.

Table 2

**Composition and characteristic of the natural oil-based formulations with the constant water concentration (90%)**

Sample name	S:O	S:CoS	S/CoS:O	Z-Ave d [nm]	PDI
Olive oil nanoemulsions					
NE/P80/OO/9:1	9:1	–	–	16 ± 1	0.308
NE/P80/OO/8:2	8:2	–	–	–	–
NE/P80/N150/9:1/OO/9:1	–	9:1	9:1	264 ± 66	0.595
NE/P80/N150/8:2/OO/9:1	–	8:2	9:1	133 ± 7	0.643
NE/P80/N150/7:3/OO/9:1	–	7:3	9:1	–	–
Strawberry seed oil nanoemulsions					
NE/P80/OT/9:1	9:1	–	–	43 ± 11	0.371
NE/P80/OT/8:2	8:2	–	–	77 ± 15	0.654
NE/P80/N150/9:1/OT/9:1	–	9:1	9:1	27 ± 10	0.273
NE/P80/N150/8:2/OT/9:1	–	8:2	9:1	128 ± 18	0.576
NE/P80/N150/7:3/OT/9:1	–	7:3	9:1	201 ± 3	0.251
NE/P80/N150/9:1/OT/8:2	–	9:1	8:2	201 ± 1,5	0.484
NE/P80/N150/8:2/OT/8:2	–	8:2	8:2	1455 ± 294	0.966
Blackcurrant seed oil nanoemulsions					
NE/P80/OP/9:1	9:1	–	–	11 ± 1	0.111
NE/P80/OP/8:2	8:2	–	–	18 ± 1	0.259
NE/P80/N150/9:1/OP/9:1	–	9:1	9:1	16 ± 1	0.341
NE/P80/N150/8:2/OP/9:1	–	8:2	9:1	15 ± 3	0.246
NE/P80/N150/7:3/OP/9:1	–	7:3	9:1	35 ± 3	0.277

As it is shown in table 2, the increase of oil content in the formulations causes the increase of droplet size of the internal phase. In other words, when the surfactant:oil ratio decreased, the particle droplet size became larger. This observation is compatible with the results of other research groups [19, 26, 27]. Li and co-workers [26] investigated the composition and stability of natural oils based nanoemulsions containing D-limonene as an active. They used Tween 80 as a surfactant, deionised water as the aqueous phase and a number of different oils (olive oil, corn oil, sunflower oil and soybean oil), used separately as an oily phase. Researchers

found that, with an increase in the concentration of olive oil, the mean particle diameter of the emulsions increased as well. The nanoemulsions were obtained only when the concentration of olive oil was less than 15% w/w, however, the droplet size distribution was bimodal for the entire range of oil concentrations. Comparable results were obtained for the rest of plant oils.

Komaiko and McClement [27] tested four main variables: surfactant-to-oil ratio (SOR), type of surfactant, type of oil and the surfactant location. Researchers used various oil phases to prepare the emulsions: medium chain triglycerides, orange oil, mineral oil, lemon oil, fish oil, grapeseed oil, canola oil, sesame oil, peanut oil and virgin olive oil. The formulations were stabilised by non-ionic surfactants: Tween 20, 40, 60, 80, 85 and Span 20. They have observed that, at lower surfactant-oil-ratios (SORs), larger droplets of the oil phase were formed and smaller droplets were formed at higher SORs. The emulsions appeared less turbid with the increase of SORs. The nanoemulsions at higher SORs were monomodal, with a narrow particle size distribution. Similar results were obtained by Ostertag and co-workers [25]. They rely on the discovery of Anton and Vandame [28] that if there is insufficient surfactant concentration to stabilise the droplets and to cover all of the droplet surfaces formed, then coalescence will occur. Moreover, they pointed out that, if the surfactant concentration is too high, the particle size may increase due to the formation of liquid crystals. Davidov-Pardo and McClements [18] supposed that a decrease in the droplet size is related to a reduction in the interfacial tension caused by an increase of the surfactant concentration. On the other hand, an increase in the polydispersity of the sample at high surfactant level can be due to the formation of bimodal distribution.

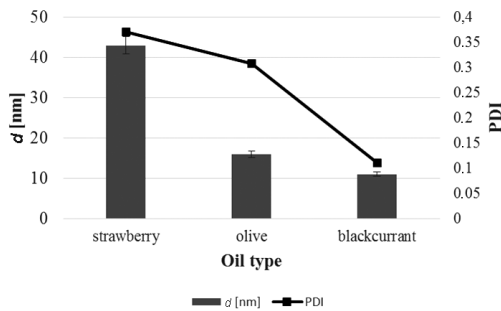


Fig. 1. Mean particle droplet size of nanoemulsions stabilised by Polysorbate 80 with constant S:O ratio (9:1) based on three tested oils

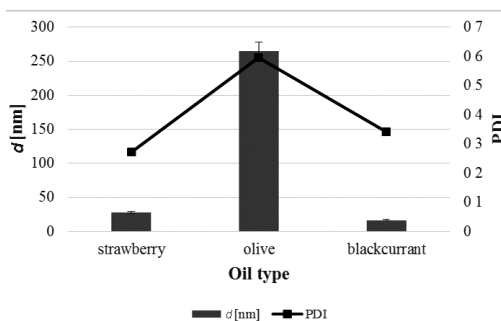


Fig. 2. Mean particle droplet size of nanoemulsions stabilised by the mixture of Polysorbate 80/Natragem S 150 (S/CoS = 9:1) based on three tested oils

Figure 1 shows that nanoemulsions stabilised by Polysorbate 80, based on blackcurrant seed oil, are characterised by the smallest droplet size ( $d = 11$  nm). Olive oil-based nanoemulsions have an average droplet size. In the case of emulsion systems stabilised by the mixture of surfactants (Polysorbate 80 and Natragem S150), olive oil-based nanoemulsion is characterised by the lowest dispersion degree (Fig. 2). According to the results of other research groups [25, 27], which also used polyethoxylated esters of sorbitan and fatty acid as emulsifiers and low-energy emulsification method, particle size of the prepared nanoemulsions depended on kind of oil used. Ostertag et al. [25] obtained the smallest particles for olive oil systems and the largest ones for canola oil. On the other hand, Kamaiko&McClements [27] found that the smallest particles was had by the grapeseed oil-emulsion, and the largest ones by the olive oil-based emulsion. These results confirmed that there is no simple correlation between the mean droplet diameter of nanoemulsions and the physicochemical properties of the used oils (such as: refractive index, density, interfacial tension and viscosity) [27]. The nature of the surfactant used in the studies had a major impact on the size of the obtained formulations [25].

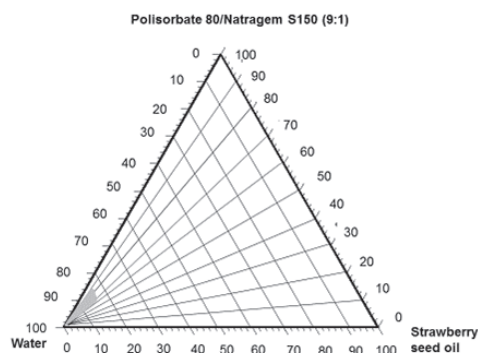


Fig. 3. Pseudo-ternary phase diagram for the Strawberry seed oil/Polysorbate 80/Natragem S150/Water system, at  $T = 25^{\circ}\text{C}$

For each studied oil, the area of nanoemulsion occurrence was very narrow, despite the co-surfactant addition. Only for strawberry seed oil (Fig. 3), transparent or transparent-bluish liquid dispersions appeared after addition of approximately 85 wt. % of water to the surfactant/co-surfactant:oil (S/CoS:O) mixture of weight ratio 9:1 and 8:2. In the case of other oils, the region of nanoemulsion formation could not be extended at a S/CoS:O ratio higher than 9:1 (Table 2).

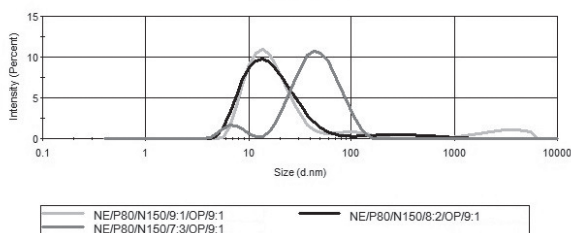


Fig. 4. Particle size distribution of blackcurrant seed oil nanoemulsion with different surfactant-to-co-surfactant (S/CoS) ratio

An addition of co-surfactant to the strawberry and blackcurrant oil-based systems resulted in an increase of their particle droplet size (Fig. 4). However, nanoemulsion based on blackcurrant seed oil, which was stabilised by both surfactants (Polysorbate 80 and Natragem S150), was characterised by a very small droplets size, (around 15 nm), and narrow distribution (PDI around 0.25).

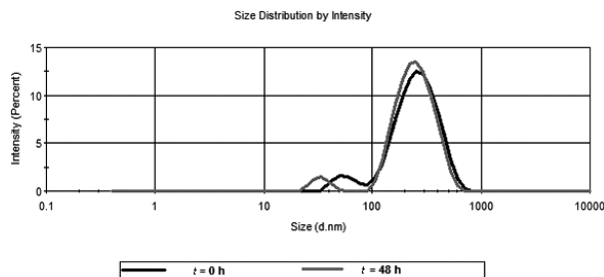


Fig. 5. Comparison of particle size distribution of nanoemulsion NE/P80/N150/7:3/OT/9:1 after preparation and after 48 hours,  $T = 25^{\circ}\text{C}$

Moreover, formulations with co-surfactant were kinetically stable during 48 hours of storage. The average droplet size and polydispersity of index remained almost unchanged (Fig. 5).

#### 4. Conclusions

The obtained results confirmed that an increase of natural oil content in the nanoemulsion formulations causes an increase of the droplet size of the internal phase. However, there is no simple correlation between the mean droplet diameter of the nanoemulsions and the physicochemical properties of the oils used. A major impact on the size of the obtained formulations is had by the nature of the applied surfactants. In the case of strawberry and blackcurrant oil-based systems, the addition of co-surfactant resulted in an increase of their droplets size, but a decrease of their kinetic stability. The nanoemulsions with the smallest droplets size ( $d = 15$  nm), low polydispersity index ( $\text{PDI} = 0.25$ ) and high kinetic stability, were obtained using blackcurrant seed oil and a mixture of surfactant/co-surfactant (Polysorbate 80/Natragem 150).

#### References

- [1] Malinowska O., Szeląg H., *The investigation of application possibilities and rheological behavior of crude fruit seed oil in emulsion system*, International Journal of Research in Cosmetic Science, Vol. 3(1), 2013, 7–13.
- [2] Jaworska M., Sikora E., Ogonowski J., *Nanoemulsje – charakterystyka i metody otrzymania*, Przemysł Chemiczny, Vol. 93(7), 2014, 1000–1005.

- [3] Sharma A., Kumar. S.M, Mahadevan N., *Nanotechnology: A Promising Approach For Cosmetics*, International Journal of Recent Advances in Pharmaceutical Research, Vol. 2(2), 2012, 54–61.
- [4] Fernandez P., Andre V., Rieger J., Kühnle A., *Nano-emulsion formation by emulsion phase inversion*, Colloids and Surfaces A: Physicochem. Eng. Aspects, Vol. 251, 2004, 53–58.
- [5] Porras M., Solans C., Gonzalez C., Gutierrez J.M., *Properties of water-in-oil (W/O) nano-emulsions prepared by a low-energy emulsification method*, Colloids and Surfaces A: Physicochem. Eng. Aspects, Vol. 324, 2008, 181–188.
- [6] Tadros T., Izquierdo P., Esquena J., Solans C., *Formation and stability of nano-emulsions*, Advances in Colloid and Interface Science, Vol. 108–109, 2004, 303–318.
- [7] Yang H., Cho W., Park S., *Stability of oil-in-water nano-emulsions prepared using the phase inversion composition method*, Journal of Industrial and Engineering Chemistry, Vol. 15, 2009, 331–335.
- [8] Usón N., Garcia M.J., Solans C., *Formation of water-in-oil (W/O) nanoemulsions in a water/mixed nonionic surfactant/oil systems prepared by low energy methods*, Colloids and Surfaces A: Physicochem. Eng. Aspects, Vol. 250, 2004, 415–421.
- [9] Sadurni N., Solans C., Azemar N., Garcia-Celma M.J., *Studies on the formation of O/W nano-emulsions, by low-energy emulsification methods, suitable for pharmaceutical applications*, European Journal of Pharmaceutical Sciences Vol. 26, 2005, 438–445.
- [10] Kelmann R., Kuminek G., Teixeira H., Koester L., *Carbamazepine parenteral nanoemulsions prepared by spontaneous emulsification process*, International Journal of Pharmaceutics, Vol. 342, 2007, 231–239.
- [11] Saberi A., Fang Y., McClements F.D., *Fabrication of vitamin E-enriched nanoemulsions: Factors affecting particle size using spontaneous emulsification*, Journal of Colloid and Interface Science, Vol. 391, 2013, 95–102.
- [12] Alayoubi A.Y., Anderson J.F., Satyanarayanajois S.D., Sylvester P.W., Nazzal S., *Concurrent delivery of tocotrienols and simvastatin by lipid nanoemulsions potentiates their antitumor activity against human mammary adenocarcinoma cells*, European Journal of Pharmaceutical Sciences, Vol. 48(3), 2013, 385–392.
- [13] Araujo F.A., Kelmann B.V., Araujo B.V., Finatto R.B., Teixeira H.F., Koester L.S., *Development and characterization of parenteral nanoemulsions containing thalidomide*, European Journal of Pharmaceutical Science, Vol. 42(3), 2011, 238–245.
- [14] Kuo F., Subramanian B., Kotyla T., Wilson T., Yoganathanb S., Nicolosi R., *Nanoemulsions of an antioxidant synergy formulation containing tocopherol have enhanced bioavailability and anti-inflammatory properties*, International Journal of Pharmaceutics, Vol. 363, 2008, 206–213.
- [15] Mou D., Chen H., Du D., Mao C., Wan J., Xu H., Yang X., *Hydrogel-thickened nanoemulsion system for topical delivery of lipophilic drugs*, International Journal of Pharmaceutics International Journal of Pharmaceutics, 2008, 353, 270–276.
- [16] Kotyla T., Kuo F., Moolchandani V., Wilson T., Nicolosi R., *Increased bioavailability of a transdermal application of a nano-sized emulsion preparation*, International Journal of Pharmaceutics, Vol. 347, 2008, 144–148.
- [17] Bernardi D., Pereira T., Maciel N., Bortoloto J., Viera G., Oliveira G., Rocha-Filho P., *Formation and stability of oil-in-water nanoemulsions containing rice bran oil: in vitro and in vivo assessments*, Journal of nanobiotechnology, 2011, 9–44.

- [18] Davidov-Pardo G., McClements D.J., *Nutraceutical delivery systems: Resveratrol encapsulation in grape seed oil nanoemulsions formed by spontaneous emulsification*, Food Chemistry, Vol. 167, 2015, 205–2012.
- [19] Eid A.M.M., Baie S.H., Arafat O.M., *The Effect of Surfactant Blends on the Production of SelfEmulsifying System*, Vol. 2(2), 2012, 21–31.
- [20] Dweck A.C., *Formulating Natural Cosmetics*, Allured Books, 2011 .
- [21] Hoed V., De Clercq N., Echim C., Andjelkovic M., Leber E., Dewettinck K., Verhé R., *Berry seeds: a source of specialty oils with high content of bioactives and nutritionalvalue*, Journal of Food Lipids, Vol. 16, 2009, 33–49.
- [22] Sikora E., Michorczyk P., Olszańska M., Ogonowski J., *Supercritical CO<sub>2</sub> extract from strawberry seeds as a valuable, component of mild cleansing compositions*, International Journal of Cosmetic Science, Vol. 37, 2015, 574–578.
- [23] Rój E., Dobrzyńska-Inger A., Kostrzewa D., Kołodziejczyk K., Sój M., Król B., Miszcza A., Markowski J., *Extraction of berry seed oils with supercritical CO<sub>2</sub>*, Przemysł Chemiczny, Vol. 88 (12), 2009, 1325–1330.
- [24] Sovilj M., *Critical review of supercritical carbon dioxide extraction of selected oil seeds*, APTEFF, Vol. 41, 2010, 105–120.
- [25] Ostertag F., Weiss J., McClements D.J., *Low–energy formation of edible nanoemulsions: Factors influencing droplet size produced by emulsion phase inversion*, Journal of Colloid and Interface Science, Vol. 388, 2012, 95–102.
- [26] Li Y., Zhang Z., Yuan Q., Liang H., Vriesekoop F., *Process optimization and stability of D–limonene nanoemulsions preapred by catastrophic phase inversion method*, Journal of Food Engineering, Vol. 119, 2013, 419–424.
- [27] Komaiko J., McClements D.J., *Low–energy formation of edible nanoemulsions by spontaneous emulsification: Factors influencing particle size*, Journal of Food Engineering, Vol. 146, 2015, 122–128.
- [28] Anton N., Vandamme T., *The universality of low–energy nano–emulsification*, International Journal of Pharmaceutics, Vol. 377, 2009, 142–147.

KRZYSZTOF NEUPAUER, TADEUSZ KOMOROWICZ, KRZYSZTOF KUPIEC\*

## COOLING OF HOT WATER WITH NON-UNIFORM INITIAL TEMPERATURE

### CHŁODZENIE GORAĄCEJ WODY O NIEJEDNORODNEJ TEMPERATURZE POCZĄTKOWEJ

#### Abstract

A mathematical model of water cooling in a vertical tank with non-uniform initial temperature has been presented in this paper. This kind of process is important in solar installations. Calculation results for various cases comprising, among others, two or three layers of water with different initial process temperatures as well as various combinations of heat resistance of the side wall, the tank bottom and the tank cover, have been given as well.

*Keywords: thermal destratification, heat conduction equation, renewable energy sources*

#### Streszczenie

Przedstawiono model matematyczny chłodzenia wody o niejednorodnej temperaturze początkowej w zbiorniku o osi pionowej. Taki proces ma praktycznie znaczenie w instalacjach solar-nych. Przedstawiono wyniki obliczeń dla różnych przypadków obejmujących m.in. dwie lub trzy warstwy wody o różnych temperaturach na początku procesu oraz rozmaite kombinacje pomiędzy wielkościami oporów cieplnych ściany bocznej oraz dna i pokrywy zbiornika.

*Słowa kluczowe: destratyfikacja termiczna, równanie przewodzenia ciepła, odnawialne źródła energii*

\* Ph.D. Eng. Krzysztof Neupauer, Ph.D. Eng. Tadeusz Komorowicz, Prof. Ph.D. D.Sc. Eng. Krzysztof Kupiec, Faculty of Chemical Engineering and Technology, Cracow University of Technology.

## 1. Introduction

A temporary, a twenty-four-hour, as well as a seasonal periodical operation of renewable energy sources require the employment of heat storage systems [1, 2]. The storage of thermal energy in solar systems considerably improves their power efficiency – the energy delivery can be continuous and proportional to the energy demand. Both the collection of heat from the water and the delivery of heat to the water in a tank cause a differentiation of water temperatures called “thermal stratification”: the hot water is located in the top space of tank, while the cooler in the bottom. The thermal stratification is a desired phenomenon, which improves the power efficiency of the installation. A phenomenon opposite to thermal stratification is spontaneous equalisation of temperatures (destratification). The intensity of this process depends on the vertical temperature gradient: the greater the vertical temperature gradient, the greater the intensity. Destratification appears when a break in the delivery and collection of heat occurs in a tank with different water temperature layers. A destratification process usually is overlapped by a heat transfer process through the tank wall. The process of thermal stratification was the subject of many experimental works. An overview of issues related to the thermal stratification in water storage tanks was presented recently in [3].

In this paper, a mathematical model and the results of simulation calculations of the temperature equalisation process in a tank with several different water temperature layers has been presented. The model also takes into account heat losses to the surroundings through the side wall, the tank bottom and the tank cover. A simplified form of this model, only taking into account heat losses through the side wall and its experimental verification, was given in [4].

## 2. Calculational relations

A vertical axis tank full of different water temperature layers has been considered. The temperature of each layer is higher than the temperature of the surroundings. As a result of both the heat conduction and convection, equalisation of temperatures in the tank appears. At the same time, the tank contents are cooled as a result of simultaneous heat losses to the surroundings through the side wall, the bottom and the cover.

Heat transport in water has been described with the use of the heat conduction equation with an effective heat conduction coefficient also taking into account the convection.

For high values of the tank height to the tank diameter ratio, the radial water temperature changes can be neglected. Heat losses through the tank side wall can be described with a source term (not with the boundary conditions). This allows for a mathematical description of both the heat transfer inside the tank and the heat transfer through the side wall with the source term, simultaneous to heat transfer through the tank bottom and the tank cover with boundary conditions. For this reason, the  $s$  height tank has been assumed in the model as an  $s$  thick infinite plate.

For transient heat conduction in an infinite plate with a heat source, the following relation is valid [5, 6]:

$$\frac{\partial T}{\partial t} = a \frac{\partial^2 T}{\partial x^2} + \frac{q_v}{\rho c} \quad (1)$$

where:

$T$  – temperature, K,

$t$  – time, s,

- $a = k/(\rho c)$  – thermal diffusivity coefficient,  $\text{m}^2/\text{s}$ ,  
 $x$  – position coordinate,  $\text{m}$ ,  
 $k$  – effective heat conduction coefficient,  $\text{W}/(\text{m}\cdot\text{K})$ ,  
 $q_v$  – capacity of heat source,  $\text{W}/\text{m}^3$ ,  
 $c$  – specific heat,  $\text{J}/(\text{kg}\cdot\text{K})$ ,  
 $\rho$  – density,  $\text{kg}/\text{m}^3$ .

Heat losses through the side wall can be calculated using the following relation:

$$d\dot{Q} = U(T - T_a)dA \quad (2)$$

where:

- $U$  – overall heat transfer coefficient between water and surroundings,  $\text{W}/(\text{m}^2\cdot\text{K})$ ,  
 $T_a$  – temperature of the surroundings,  $\text{K}$ ,  
 $A$  – heat transfer surface area,  $\text{m}^2$ .

In the presented model,  $q_v$  describes heat transport through the side wall. The heat source capacity is thermal power generated in a unitary volume of solid. In the case of heat loss,  $q_v$  is negative. Because  $q_v = -d\dot{Q}/dV$ , one can obtain:

$$q_v = \frac{dA}{dV}U(T_a - T) \quad (3)$$

The quantity of  $q_v$  is a function of the position in tank,  $q_v(x)$ , because of the temperature variability in the tank. When  $T > T_a$ , the contents of tank lose the heat: the greater the  $T$ , the greater the heat losses. But the ratio  $dA/dV$  is constant. For a vertical axis and  $D$  diameter cylindrical tank, the following relation is valid:

$$\frac{dA}{dV} = \frac{4}{D} \quad (4)$$

therefore:

$$q_v = \frac{4U}{D}(T_a - T) \quad (5)$$

There are two different temperature water layers in the simplest case of the equalisation of temperatures. Let's assume that, at the beginning, the water temperature  $T_0$  is in the range of height  $(0, s_m)$ , whereas  $T_1$  (usually  $T_1 > T_0$ ) is in the range of height  $(s_m, s)$ .

Then, the initial condition is as follows (Fig. 1):

$$t = 0 \quad \begin{cases} \text{for } 0 < x \leq s_m & T = T_0 \\ \text{for } s_m < x \leq s & T = T_1 \end{cases} \quad (6)$$

The mean water temperature in the tank at the beginning of the process can be calculated as a weighted average:

$$T_m = \frac{s_m}{s}T_0 + \left(1 - \frac{s_m}{s}\right)T_1 \quad (7)$$

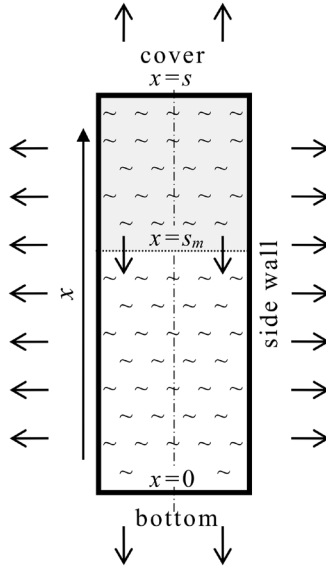


Fig. 1. Vertical axis tank

The boundary conditions concern the tank bottom and the tank cover. For the tank bottom:

$$x = 0 \quad k \frac{\partial T}{\partial x} = \frac{T - T_s}{R_0} \quad (8)$$

For the tank cover:

$$x = s \quad -k \frac{\partial T}{\partial x} = \frac{T - T_s}{R_1} \quad (9)$$

$R_0$  and  $R_1$  are the thermal resistances of the tank bottom and the tank cover, respectively, while  $T_s$  is the external temperature of the surroundings near the tank bottom/the tank cover. The temperature  $T_s$  can be different to  $T_a$ .

In the case of a high thermal resistance of the tank bottom and the tank cover,  $R$  depends mainly on the insulation conduction resistance  $s_i/k_i$ . Generally, the resistances depend also on the partial heat transfer coefficients  $h_0$  and  $h_1$  outside the tank:

$$R_0 = \frac{1}{h_0} + \frac{s_{0i}}{k_{0i}} \quad R_1 = \frac{1}{h_1} + \frac{s_{1i}}{k_{1i}} \quad (10)$$

If the tank bottom and the tank cover are perfectly insulated ( $R \rightarrow \infty$ ), the boundary conditions are as follows:

$$x = 0 \quad \frac{\partial T}{\partial x} = 0 \quad (11)$$

$$x = s \quad \frac{\partial T}{\partial x} = 0 \quad (12)$$

Relations (11) and (12) denote non-permeability of heat flux through the tank bottom and the tank cover, respectively.

The model equations can be solved easily with the method of finite differences.

### 3. Results of calculations

In all of the calculations, the initial temperature in the top tank space is equal to 90°C, whereas in the bottom, it is 70°C. The total tank height equals 1.8 m. The upper layer ranges from 1.1 m upwards. The assumption  $T_a = T_s = 20^\circ\text{C}$  has been made.

Fig. 2 presents the temperature profiles in a totally insulated tank. The value of effective heat conduction coefficient equal to  $k = 0.5 \text{ W}/(\text{m}\cdot\text{K})$ , approximate to the water conductivity, has been assumed in the calculations. Each individual course concerns a specific process time length. It can be observed that the equalisation of temperatures is slow and the system temperature tends to be a value of  $T_m = 77.8^\circ\text{C}$ , calculated according to the relation (7).

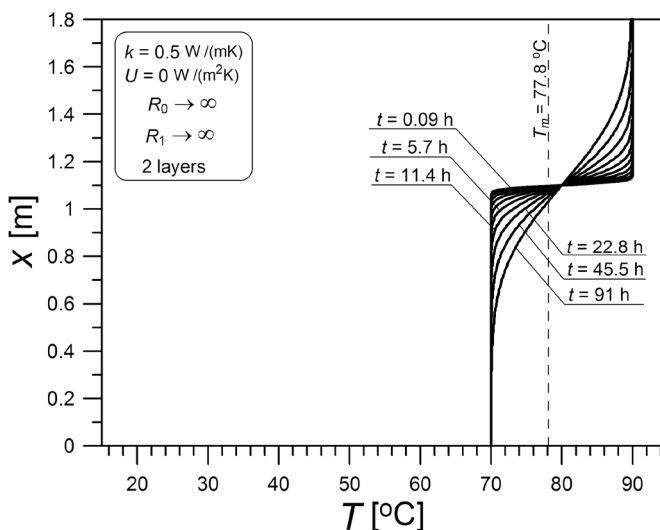


Fig. 2. Temperature profiles in tank filled with water; side wall, bottom and cover perfectly insulated; two water layers;  $k = 0.5 \text{ W}/(\text{m}\cdot\text{K})$

The temperature profiles in a tank initially containing three different water temperature layers – upper (90°C), intermediate (80°C) and bottom (70°C) – have been also determined. The height of the intermediate layer ranges from 0.9 to 1.1 m. As it was previously, the tank is totally insulated and the effective heat conduction coefficient equals  $0.5 \text{ W}/(\text{m}\cdot\text{K})$ .

The courses of temperature profiles, presented in Fig. 3, result from the existence of three different water temperature layers at the beginning of the process. The system tends to reach a temperature of  $T_m$ , resulting from the following calculation:

$$T_m = \frac{0.9}{1.8} \cdot 70 + \frac{0.2}{1.8} \cdot 80 + \frac{0.7}{1.8} \cdot 90 = 78.9^\circ\text{C} \quad (13)$$

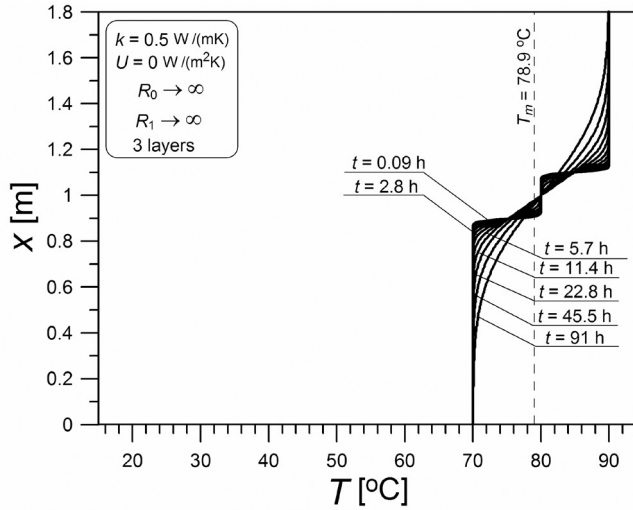


Fig. 3. Temperature profiles in tank filled with water; side wall, bottom and cover perfectly insulated; three water layers;  $k = 0.5 \text{ W}/(\text{m}\cdot\text{K})$

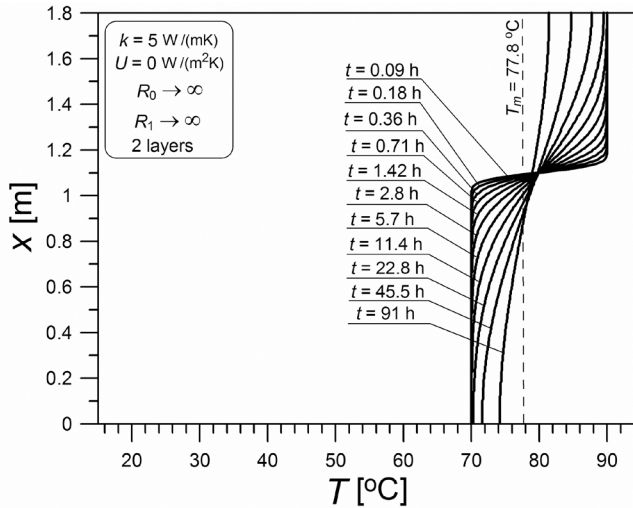


Fig. 4. Temperature profiles in tank filled with water; side wall, bottom and cover perfectly insulated; two water layers;  $k = 5 \text{ W}/(\text{m}\cdot\text{K})$

More realistic shapes of temperature profiles have been obtained under the assumption of a value of the effective heat conduction coefficient equal to  $k = 5 \text{ W}/(\text{m}\cdot\text{K})$ , i.e. as much as 10 times greater than a value of the ordinary coefficient, independent of the convection. The profiles are presented in Fig. 4. An assumption of the total tank insulation also has been made. The system tends to reach an equilibrium temperature of  $T_m = 77.8^\circ\text{C}$  faster. In real conditions of the destratification process, a considerable amount of heat is transferred by the convection accelerating the equalisation process of temperatures in relation to the conduction, which practically does not take place in pure form within fluids.

The actual temperature profiles in a tank generally have a different shapes resulting from heat losses to the surroundings. If heat losses exist, a cooling process of the tank contents overlaps the process of the equalisation of temperatures. It should be taken into account that the rate of the cooling process varies both in time and along the tank height. The higher the water temperature, the greater the cooling rate. Figs. 5, 6 and 7 present profiles of various combinations of thermal resistances values of different tank elements: the side wall, the bottom and the cover.

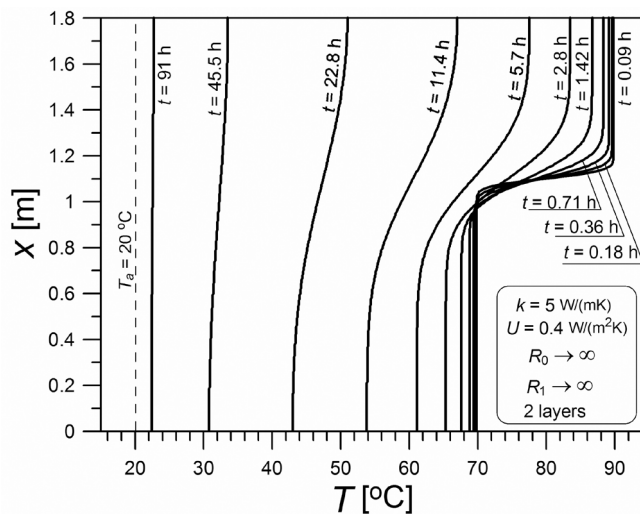


Fig. 5. Temperature profiles in tank filled with water; bottom and cover perfectly insulated; two water layers;  $k = 5 \text{ W}/(\text{m}\cdot\text{K})$

Fig. 5 depicts the temperature profiles in the process of the equalisation of temperatures as well as the process of the cooling of the tank content, if the tank bottom and the tank cover are perfectly insulated. The value of the overall heat transfer coefficient of  $U = 0.4 \text{ W}/(\text{m}^2\cdot\text{K})$  has been assumed. Because of the non-permeability of heat through the tank bottom and the tank cover, the temperature profiles near  $x = 0$  and  $x = s$  are vertical, in accordance with the boundary conditions (11) and (12). The longer the process time, the more flat the temperature profiles. The system tends to reach a temperature of  $20^\circ\text{C}$ , i.e. the temperature of the surroundings.

The presented model gives the possibility to take into account both the heat losses through the side wall as well as the heat losses through the tank bottom and the tank cover (it is possible to assume that the temperature of the surroundings near the tank cover and near the tank bottom  $T_s$  is different than the temperature near the side wall  $T_a$ ). Fig. 6 depicts the temperature profiles in the case of a perfectly insulated tank cover only. A difference in courses in Figs. 5 and 6 can be observable in the bottom figure part: near  $x = 0$  the profiles are vertical (Fig. 5) or are deflected (Fig. 6).

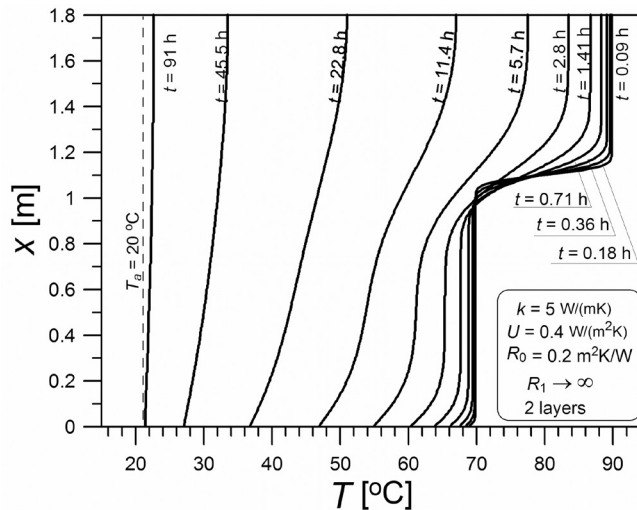


Fig. 6. Temperature profiles in tank filled with water; tank cover perfectly insulated; two water layers;  $k = 5 \text{ W}/(\text{m} \cdot \text{K})$

Fig. 7 presents all of the possible directions of heat loss from water: a horizontal direction through the tank side wall, and a vertical direction downwards through the tank bottom, and upwards through the tank cover. The heat resistance of the tank cover has been assumed to be considerably lower than the heat resistance of the tank bottom. This assumption causes a strong deflection of temperature profiles in the upper tank space.

A comparison of profiles in Figs. 5, 6 and 7 leads to a conclusion about the rate of heat losses in the considered cases. Under the conditions described in Fig. 5, the heat losses are the lowest, whereas under conditions described in Fig. 7 – the highest. This situation is reflected by the water temperature ranges in the tank. By way of example, for the process time length  $t = 22.8 \text{ hr}$  and for the existence of heat losses only in the side wall (Fig. 5), the water temperature in the tank ranges from  $43^\circ\text{C}$  to  $51^\circ\text{C}$ . If the heat losses exist also in the tank bottom, the water temperature in the tank ranges from  $37^\circ\text{C}$  to  $50^\circ\text{C}$  (Fig. 6). However, if the heat losses exist also in the tank bottom, the water temperature in the tank after  $22.8 \text{ hr}$  ranges from  $31^\circ\text{C}$  to  $37^\circ\text{C}$  (Fig. 7). In the last case, the water temperature near the tank cover is lower than the temperature near the tank bottom (in spite of an opposite relation at initial conditions) because of a small value of the tank cover heat resistance causing a considerable heat loss in this location.

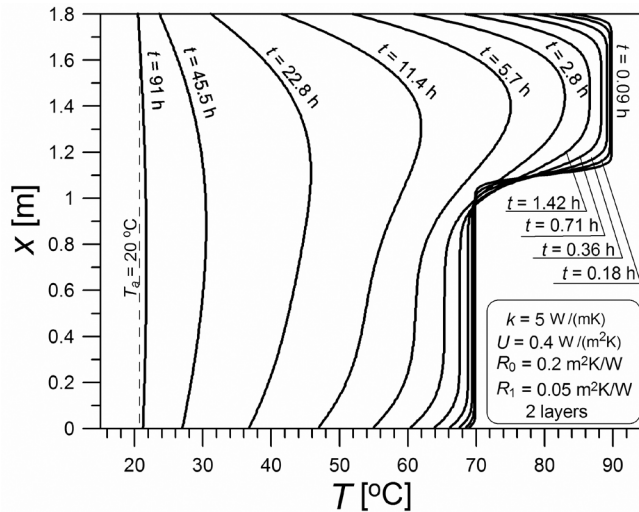


Fig. 7. Temperature profiles in tank filled with water; two water layers;  $k = 5 \text{ W}/(\text{m}\cdot\text{K})$

#### 4. Conclusions

The presented mathematical model is based on a one-dimensional equation of heat conduction, describing simultaneous heat transfer inside of a vertical axis tank and heat losses through the side wall, the tank bottom, and the tank cover, to surroundings.

The model has been verified experimentally and can be applied for the simulation of thermal processes in storage tanks filled with hot water.

The model is valid for both the heat transfer resulting from the internal temperature gradients as well as for the heat transfer resulting from the temperature differences between the tank interior and the surroundings.

Model parameter values can be determined on the basis of a comparison between the values obtained in the calculations and in the measurements. The model parameters are: an effective heat conduction coefficient and the thermal resistances through the side wall, the bottom and the cover of the tank.

## References

- [1] Duffie J.A., Beckman W.A., *Solar Engineering of Thermal Processes*, Wiley Inc., New York 2006.
- [2] Pluta Z., *Słoneczne instalacje energetyczne*, Oficyna Wydawnicza Politechniki Warszawskiej, Warszawa 2008.
- [3] Njoku H.O., Ekechukwu O.V., Onyegegbu S.O., *Analysis of stratified thermal storage systems: An overview*, Heat Mass Transfer 2014, 50, 1017–1030.
- [4] Kupiec K., Neupauer K., Larwa B., *Thermal destratification in an insulated vessel filled with water*, Heat and Mass Transfer 2016, 52, 163–167.
- [5] Staniszewski B., *Wymiana ciepła – podstawy teoretyczne*, WNT Warszawa 1979.
- [6] Cengel Y., Ghajar A., *Heat and Mass Transfer: Fundamentals and Applications*, McGrawHill 2010.

ANNA SIENKIEWICZ, PIOTR CZUB\*

## SYNTHESIS AND MECHANICAL PROPERTIES OF NOVEL EPOXY-POLYURETHANE MATERIALS BASED ON MODIFIED SOYBEAN OIL

### SYNTEZA I WŁAŚCIWOŚCI MECHANICZNE NOWYCH EPOKSYDOWO-POLIURETANOWYCH MATERIAŁÓW NA BAZIE MODYFIKOWANEGO OLEJU SOJOWEGO

#### Abstract

The paper presents the results of studies on the synthesis and mechanical properties of the fusion product of epoxidized soybean oil with bisphenol A, which are a part of the current research on environmentally friendly raw materials for the preparation and modification of modern polymeric materials. It has been shown that the use of 4,4'-methylene diphenyl diisocyanate in the cross-linking process of the fusion product in the presence of Dabco 33-LV and BYK-A530 or BYK-A525 gives hard materials with interesting mechanical properties.

*Keywords: bisphenol A, diisocyanates, epoxidized soybean oil, epoxy fusion process*

#### Streszczenie

W pracy przedstawiono wyniki badań nad syntezą i właściwościami mechanicznymi produktu stapiania epoksydowanego oleju sojowego z bisfenolem A, które wpisują się w nurt poszukiwań proekologicznych surowców do otrzymywania i modyfikacji nowoczesnych materiałów polimerowych. Wykazano, że użycie 4,4'-diizocyjanianu difenylometanu w procesie sieciowania produktu stapiania w obecności Dabco 33-LV oraz BYK-A530 lub BYK-A525 prowadzi do otrzymania twardych materiałów o ciekawych właściwościach mechanicznych.

*Słowa kluczowe: bisfenol A, diizocyjaniany, epoksydowany olej sojowy, reakcje stapiania,*

\* M.Sc. Anna Sienkiewicz, Prof. Ph.D. D.Sc. Eng. Piotr Czub, Department of Chemistry and Technology of Polymers, Faculty of Chemical Engineering and Technology, Cracow University of Technology.

## 1. Introduction

The big challenge for modern chemistry and chemical technology is, first of all, the need to seek new sources of raw materials, which would become the alternative to petroleum-derived feedstocks. Another very important challenge is the necessity to protect our natural environment; hence, the drive to meet the requirements of the so-called 'green chemistry'. The use of modified vegetable oils gathers these principles. Vegetable oils are substances of natural origin and from renewable sources. They are non-toxic, cheap and biodegradable. What is also important is that oils are materials differing in composition (depending on their origin, vegetable oils contain in their triglyceride molecules residues of various fatty acids in different amounts), but also in the chemical structure (fatty acid residues generally contain unsaturated bonds, however, in oils obtained from some plants, hydroxyl or epoxy groups are present naturally). Therefore, after suitable modification, for many years, vegetable oils have been used as plasticisers for thermoplastics (epoxide derivatives) [1], as well as natural components of polyol mixtures (hydroxyl derivatives) for the production of polyurethane materials [2–4]. Currently, around the world, studies on the application of vegetable oils as a source of many valuable derivatives, which could be used either for modification of other polymers [5] or as raw materials for their synthesis [6], are undertaken. Hence, on an industrial scale, vegetable oils are used, for example, for bio-polyamides production [7], for which, by modifying selected vegetable oils, both essential fatty acids and amines [8] could be obtained. From scientific and patent literature, there are known proposals for the use of derivatives of plant triglycerides as raw materials for the synthesis of the other polymers, such as: poly(hydroxyalcanoates) [9], polyesteramides [10], polyetheramides [11] and alkyds [12]. At the same time, efforts are also put on studies on the use of modified vegetable oils in epoxy resin technology, such as: reactive diluents [13], modifiers for increasing toughness and flexibility [14] or even raw materials in the synthesis of high-molecular-weight resins by polyaddition carried out in bulk by the fusion process [15–16].

In our group, numerous experiments have been performed on the application of a novel pro-ecological method of the synthesis of epoxy materials. This new and interesting reaction is based on a conventional method of the synthesis of high-molecular-weight (1,500–10,000 g/mol) epoxy resins in the epoxy fusion process involving low- and average-molecular-weight epoxies and bisphenols [17] (Fig. 1).

Our method, which meets the requirements of 'green chemistry', not only eliminates the necessity for the application of solvents that are harmful for environment, strong acids and alkali [18], which is particularly important for ecological awareness, but also is proposing partially replacing petrochemical raw materials by introducing modified vegetable oils in the form of epoxidized or hydroxylised derivatives. The elaborated process is simple and gives the opportunity of obtaining a product of the design properties and molecular weight, which is much higher than *via* the conventional solvent method. The introduction of vegetable oils in the process of synthesis of epoxy resins results in obtaining a pro-ecological product with better applicable characteristics (e.g. lower viscosity [13], [19–20] and higher resilience) than *via* the conventional method using petrochemical raw materials.

The developed method of the synthesis allows to obtain new and very interesting epoxy material, containing free epoxy and hydroxyl groups in their structure. It is possible to cross-link products of the epoxy fusion process with, e.g. diisocyanates, obtaining novel epoxy-

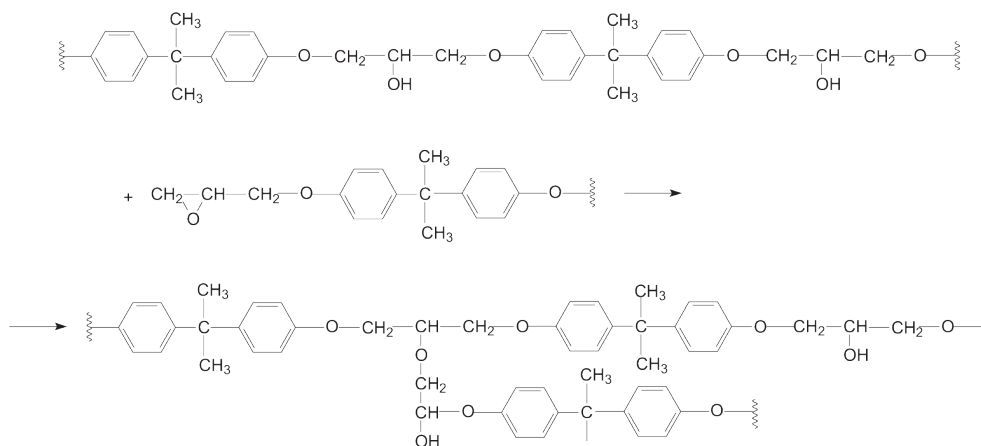


Fig. 1. The conventional method of the high-molecular-weight epoxy resins synthesis

polyurethane materials of which characteristics depend on the choice of the cross-linking method [21]. Therefore, the aim of this study was to obtain a product of fusion reaction of epoxidized soybean oil with bisphenol A, then cross-link it with 4,4'-methylene diphenyl diisocyanate under different conditions and to investigate the properties of the materials as well as to determine the relationship between the selected curing estate and mechanical strength of the cured compositions. In the presented part of the research, we concentrate on obtaining materials with good mechanical properties.

## 2. Materials and methods

### 2.1. Materials

In the performed epoxy fusion process, epoxidized soybean oil (ESBO, Ergoplast EG, Boryszew, EV = 0.363mol/100g), bisphenol A (BPA, GE Cartagenie, 99.93%) and LiCl (Merck, pure; in amount of 0.002 mol per 1 mol of bisphenol A) were used.

Cross-linking of synthesised epoxy fusion product was made with the use of:

- Desmodur VL (Bayer Material Science, Germany), used as a curing agent, an aromatic polyisocyanate based on 4,4'-methylene diphenyl diisocyanate [MDI] and containing 31.5 wt.% of free -NCO groups, viscosity of 90 mPa·s (at 25°C) and density of 1.24 g/cm<sup>3</sup>.
- Dabco 33-LV (Air Products and Chemicals, Inc., USA), a mixture of 33 wt.% of triethylene diamine and 67 wt.% of dipropylene glycol, used as catalyst.
- BYK A 530 and BYK 525 (BYK – Chemie GmbH, Germany), deaerators on the silicone basis, used for facilitation of vent and skimming of cured compositions.

## 2.2. Fusion process

Epoxidized product (ESBO), bisphenol A (BPA, GE Cartagenie, 99.93%) and LiCl (Merck, pure; in amount of 0.002 mol per 1 mol of bisphenol A) have been involved in the fusion reactions. The process was carried out in a nitrogen atmosphere. In the first step, epoxidized soybean oil was heated to 110°C and a calculated amount of the BPA was added. The reaction mixture was homogenised. Then, LiCl was added and the temperature was raised to 160°C. The progress of the epoxy fusion process was monitored in time by evaluating the epoxy group contents of the obtained samples.

## 2.3. Cross-linking of the composition and samples for mechanical testing preparation

Cross-linking of epoxy fusion product was conducted with the use of selected isocyanate – Desmodur VL at a stoichiometric amount with the respect of hydroxyl groups in hardened the material. Each composition contained 1% of BYK A530 (BYK A525) deaerator. Additionally, the influence of different amounts of catalyst Dabco 33-LV on the cross-linking process and mechanical properties of cured compositions was observed. After intensive mixing, followed by venting in a vacuum dryer at 25°C, the prepared compositions were poured into forms made of PTFE and left for hardening at room temperature for 24 hours. Then, the samples were removed from forms and annealed at 80°C for another 24h.

## 2.4. Measurement methods

### 2.4.1. Spectroscopic measurements

The analysis of transmittance FT-IR spectroscopy was achieved using the FT-IR Perkin-Elmer precise system spectrophotometer (SPECTRUM 65 FT-IR, Perkin Elmer, UK). The measurements of liquid samples were performed in a form of liquid films between KBr cell windows. A drop of oil samples was placed between two KBr windows, and then it was spread evenly on their surface. Subsequently, oil samples absorbance spectra were obtained in the range of 4000–400  $\text{cm}^{-1}$  at ambient temperature of 20–22°C, using the FT-IR spectrophotometer. Composition samples were analysed using a same spectrometer equipped with ZnSe crystal attenuated total reflectance unit. Spectra were recorded with a resolution of 4  $\text{cm}^{-1}$ , from 4000 to 400  $\text{cm}^{-1}$ , with an average of 32 scans. The obtained spectra are presented in the dependence of transmittance  $T$  [%] and wave number  $\nu$  [ $\text{cm}^{-1}$ ].

### 2.4.2. Epoxy and hydroxyl values determination

The epoxy and hydroxyl values were evaluated by the titration methods. The content of epoxy groups (epoxy value, EV) in the investigated products was evaluated according to the PN-87/C-89085/13 standard: samples were dissolved in HCl/1,4-dioxane solution and titrated by NaOH/methanol in the presence of cresol red as the indicator to the visual change of the tint to purple. In order to defined the hydroxyl value (HV), respectively, samples of soybean oil, its epoxidized and fusion products were dissolved in the solution of catalyst

[4-(dimethylamine) pyridine in DMF] and acetic anhydride in DMF, followed by intensive stirring for another 15 minutes and titration with KOH aqueous solution in a presence of thymolphthalein, until the tint changed from colourless to blue.

### 2.4.3. Mechanical properties

The mechanical properties of the prepared composition samples in the form of paddles, beams and rollers, were tested. Tensile strength, elongation at break, modulus elasticity, flexural strength, elasticity flexural modulus, deflection, compressive strength and compression set, were tested using the Zwick 1445 apparatus. However, specifically tensile strength, elongation at break, modulus elasticity, were determined according to the PN-EN ISO 527-1:2012 standard on samples in the form of paddles (type B) [section measurement with dimensions: 4×10 (at cross-section) and 50 mm (length)] and the use of the Zwick apparatus equipped with an extensometer. Measurements were conducted with a 5 mm/min testing speed. Flexural strength, elasticity flexural modulus, deflection were tested according to the PN-EN ISO 178:2011 standard, using samples in the form of cuboid beams with a cross-section of 4×10 mm, with 64 mm spacing between supports and a testing speed of 10 mm/min. Compressive strength and compression set were tested according to the PN-EN ISO 604:2006 standard, using samples prepared in the form of rollers with 10 mm diameter and 25 mm height, with a testing speed of 0.8 mm/min.

Hardness in the Shore's A scale was tested according to the PN-EN ISO 868:2005 standard with the use of the InSize apparatus.

Impact toughness by the Charpy's method (PN-EN ISO 179-2:2001) was tested on the ZORN PSW 4J Digital apparatus.

## 3. Results and discussion

The basic epoxy product, which was then used as a reactant in the fusion process, was synthesised using commercially manufactured soybean oil, wherein its modification was performed in the typical process of epoxidation of natural oil. In general, this reaction is carried out in a system of hydrogen peroxide and an aliphatic carboxylic acid, in the presence of an acid catalyst (Fig. 2, reaction 1: A – soybean oil, B – epoxidized soybean oil, C – epoxy fusion dimer, D – epoxy fusion product), although, the actual oxidising agent is created *in situ* by reaction of the acid with hydrogen peroxide and the formation of an organic peracid, which then reacts with unsaturated bonds of oil macromolecules [22]. In the performed epoxy fusion process (Fig. 2, reaction 2), reagents were applied in a 1:1 molar ratio with the calculation of the amount of BPA based on the change of quantity of functional groups in substrates and products of the reaction as well with an assumption that the obtained product should contain epoxy groups on the level of 0.100 mol/100g [15–16]. Epoxy fusion process was conducted for a period of 18 h at a temperature of 160°C (the time of conducted process was established experimentally, by monitoring the epoxy value of the reacting mixture) in the presence of LiCl (0.002 mol per 1 mol of bisphenol) [23], which favours reactions of phenol groups of bisphenol A with epoxy groups over possible reaction of secondary hydroxyl groups (obtained by oxirane ring opening) with epoxy groups, as well as inhibits branching reaction and, at the same time, prevents gelling of the reacting mixture. In general, the first stage of

the bio-synthesis of novel epoxy resin involves the formation of a dimer (C) (Fig. 2, reaction 2), due to the reaction of one epoxy group of epoxidized vegetable oil with one hydroxyl group of bisphenol A. In the next stage, reactions involving subsequent molecules of either epoxidized vegetable oil (B) (with the utilisation of free hydroxyl group of bisphenol A) or BPA (reaction with the use of remaining epoxy groups) are possible, leading to the formation of linear (D1) or branched structure (D2) of epoxy fusion product (D).

After 18 h of conducting the process, it was possible to obtain decrease of epoxy group content to the level of 0.204 mol/100 g, while the hydroxyl value was 130 mgKOH/g. The structure of epoxy product was characterised by FT-IR (Fig. 4), GPC and functional group determination (epoxy and hydroxyl group contents).

On the FT-IR image of the epoxidized soybean oil, signals with little intensity, characteristic for epoxy group, are visible at  $\nu = 1240 \text{ cm}^{-1}$  and  $\nu = 832 \text{ cm}^{-1}$ , respectively. They are still

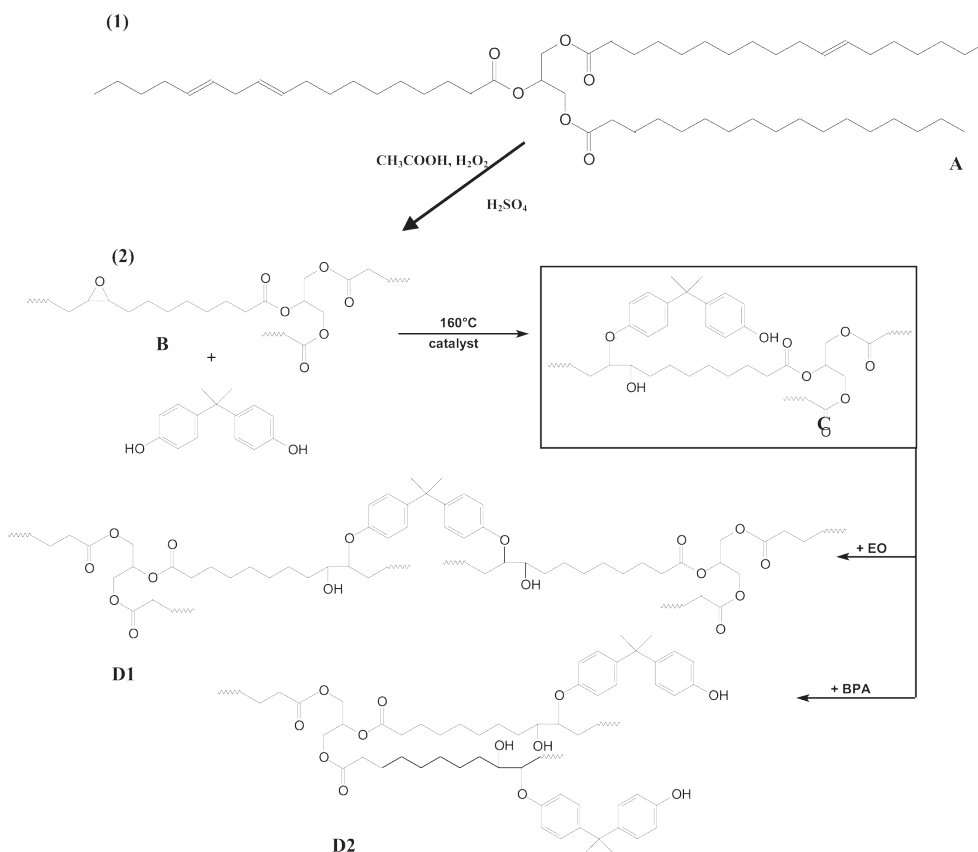


Fig. 2. Scheme of the innovative, pro-ecological method of the bio-based epoxy-polyurethane materials' synthesis – PART I: 1 – epoxidation, 2 – epoxy fusion process; A – soybean oil (SO), B – epoxidized soybean oil (ESBO), C – epoxy fusion dimer, D1 – linear epoxy fusion product formation, D2 – branched epoxy fusion product formation

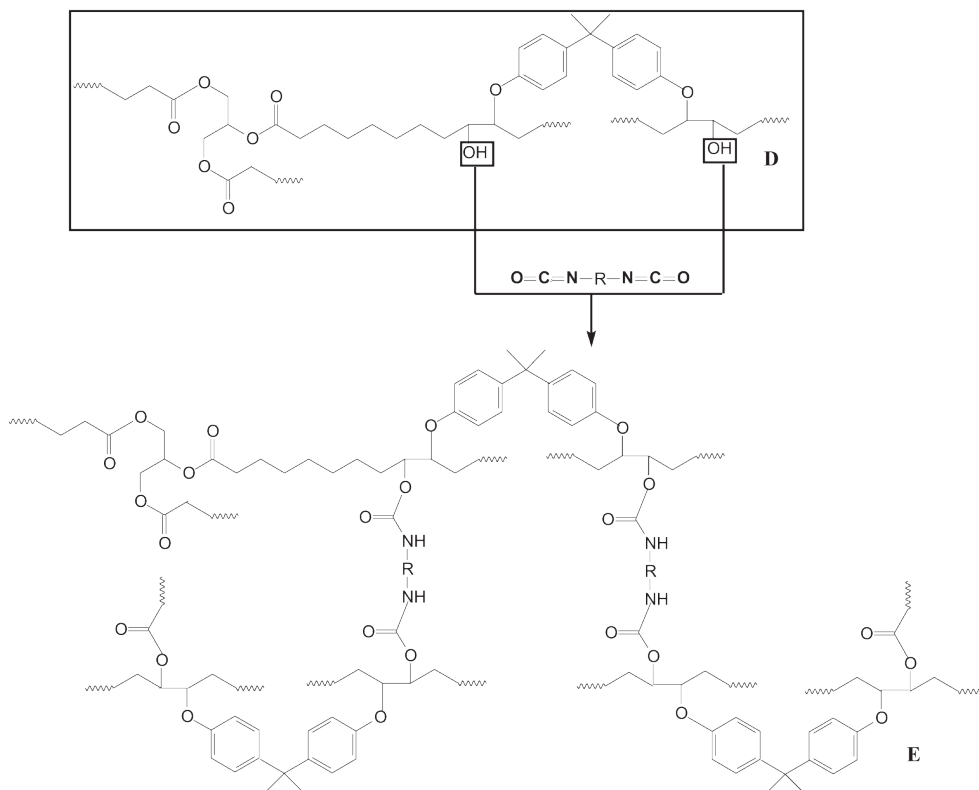


Fig. 3. Scheme of the innovative, pro-ecological method of the bio-based epoxy-polyurethane materials' synthesis – PART II: cross-linking process, D – epoxy fusion product, E – bio-based epoxy-polyurethane material

present on the spectrum of ESBO\_BPA, however, their intensities decreased and they are just visible at  $\nu = 1238 \text{ cm}^{-1}$ . The absorption signal at  $\nu = 832 \text{ cm}^{-1}$ , due to its very little intensity, is not visible and might be covered by the signal from the covalent bond of *t*-butyl group ( $\nu = 842 \text{ cm}^{-1}$ ) from bisphenol A, which has relatively high intensity. Additionally, there is a wide signal at  $\nu = 3412 \text{ cm}^{-1}$ , which can be assign to hydroxyl groups. Comparison of spectrogram images of ESBO and ESBO\_BPA confirms that the reaction between epoxidized soybean oil and bisphenol A took place, and the obtained product consists of both the epoxy and hydroxyl group. The above observations were additionally proven by titration designation of the functional group's contents. Both epoxy and hydroxyl groups might be successfully utilised for the cross-linking process, wherein the selection of cross-linking agent and the condition of the cross-linking reaction are crucial for the mechanical properties of the obtained epoxy materials. In the technology of epoxies, different curing agents might be used, including: aliphatic amines and polyamines, aromatic amines and acidic anhydrides. The research presented here not only shows the application of an innovative method of the synthesis of novel bio-based epoxy fusion products,

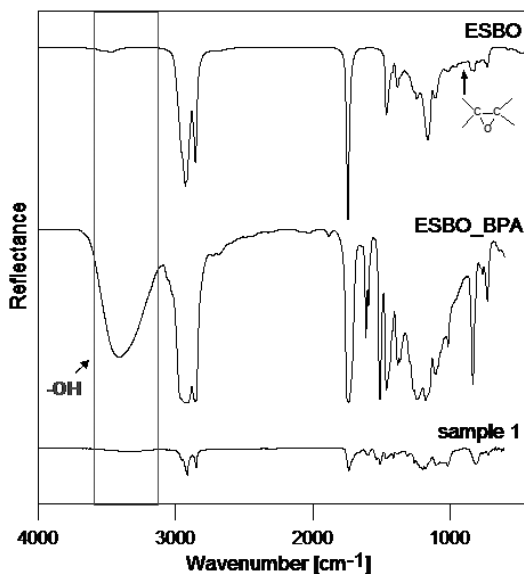


Fig. 4. FT-IR spectra of the soybean oil: epoxidized soybean oil (a) and epoxy fusion product of epoxidized soybean oil and bisphenol A (b), cross-linked epoxy-polyurethane material (c)

but also introduces diisocyanate as a curing agent for this type of materials, leading to obtaining novel materials with interesting mechanical properties. 4,4'-methylene diphenyl diisocyanate is commonly used in the technology of PU for materials, both in the form of rigid foams and elastomers. The selection of particular (aliphatic or aromatic) structure of isocyanate for the cross-linking process significantly influences the mechanical properties of the final product. As it was observed, for aliphatic isocyanates, the products are characterised by low mechanical strength and high elongation at break, while these obtained with the use of aromatic hardeners have better mechanical properties. In the part of the research presented here, we concentrate on obtaining materials with good mechanical properties. Application of 4,4'-methylene diphenyl diisocyanate for the cross-linking process is based on the reaction of hydroxyl groups of epoxy fusion product (D) and -NCO groups of diisocyanate (Fig. 3), leading to formation of hybrid epoxy-polyurethane material (E). In other words, the performed reaction utilises hydroxyl groups in the networking process, which is clearly visible on the comparison FT-IR spectrogram (Fig. 4: b-c), where the signal from hydroxyl groups present at  $\nu = 3412 \text{ cm}^{-1}$  for ESBO\_BPA is not visible for cured product.

Based on the performed cross-linking tests, five compositions were prepared and their mechanical properties were tested. Individual samples consisted of epoxy fusion product ESBO\_BPA, MDI, the catalyst (Dabco 33-LV, in about 0.00, 0.15 or 0.30 wt.%) and 1 wt.% of the deaerator (BYK A530 or BYK A525) (Table 1). Dabco 33-LV (commonly used in the polyurethane technology) has a strong influence on promoting the urethane reaction (polyol with isocyanate) in a variety of both flexible and rigid foams as well as elastomer applications.

Table 1

**List of the cured compositions submitted to mechanical properties testing**

Sample	Epoxy fusion product	Isocyanate	Catalyst	Deaerator
1	<b>ESBO_BPA</b> EV = 0.204 mol/100g HV = 130 mgKOH/g	<b>MDI</b> -NCO =31.5 wt.%	No catalyst added	BYK A530
2			Dabco 33-LV (0.3%)	
3			Dabco 33-LV (0.15%)	
4			No catalyst added	BYK A525
5			Dabco 33-LV (0.15%)	

The amount of cross-linking agent was calculated with the respect to the hydroxyl group content in the epoxy fusion product. The process was performed in open forms at room temperature for 24 h, followed by final post-curing at a temperature of 80°C for another 24 h. During both the preparation and the casting, there were no significant differences observed between the compositions. After 24 h, the cured samples were easy to remove from their forms. All of them maintained rigidity and non-transparency.

The prepared samples were subjected to mechanical tests, determining their tensile strength, elongation at break, modulus elasticity, flexural strength, elasticity flexural modulus, deflection, compressive strength, compression, hardness on the Shore'a A scale and toughness by the Charpy's method (Fig. 5–7, Table 2).

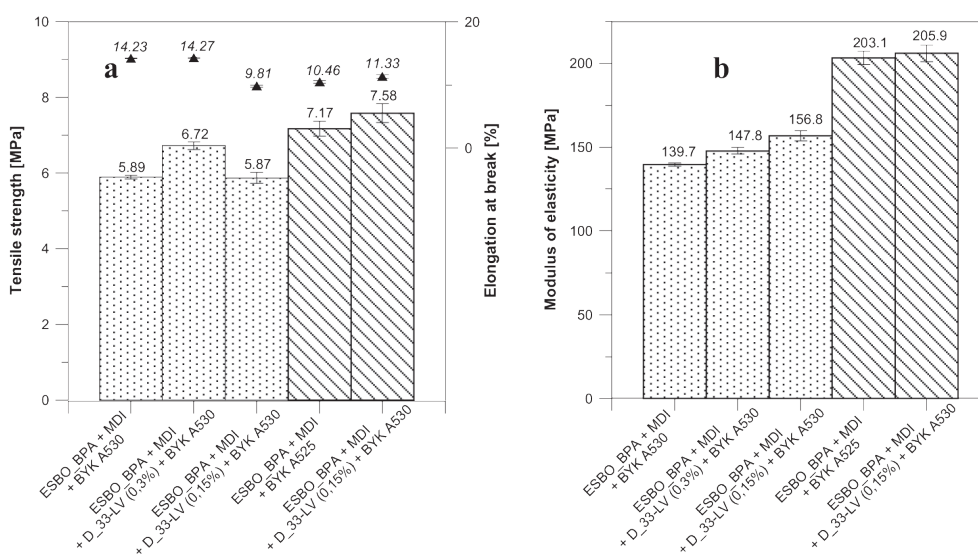


Fig. 5. Mechanical properties of epoxy fusion product, ESBO\_BPA, cross-linked with the isocyanate: tensile strength and elongation at break (a), modulus of elasticity (b)

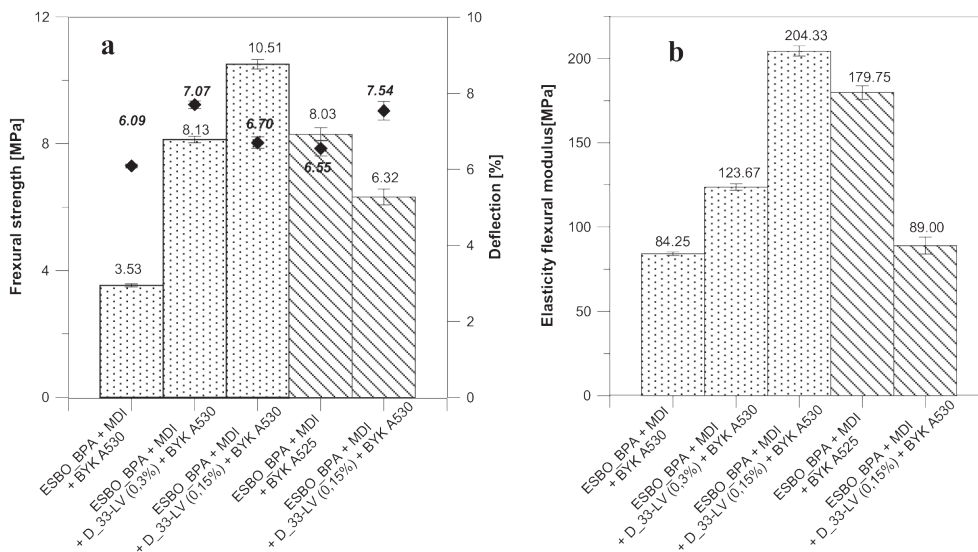


Fig. 6. Mechanical properties of epoxy fusion product, ESBO\_BPA, cross-linked with the isocyanate: flexural strength and deflection (a), elasticity flexural modulus (b)

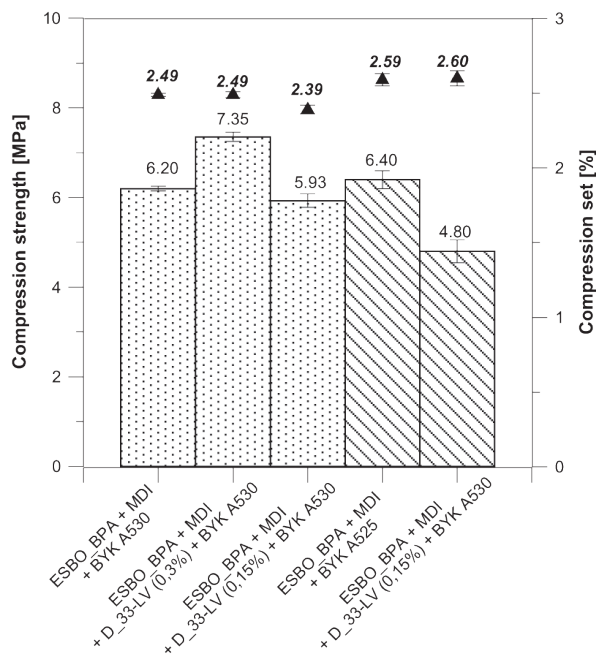


Fig. 7. Mechanical properties of epoxy fusion product, ESBO\_BPA, cross-linked with the isocyanate: compressive strength and compression set

**Mechanical properties of cross-linked epoxy-polyurethane material based on epoxy fusion product of epoxidized soybean oil and bisphenol A**

Mechanical property	Composition				
	1	2	3	4	5
Impact toughness [kJ/m <sup>2</sup> ]	11.96 ± 1.50	9.04 ± 1.34	6.93 ± 0.81	6.75 ± 0.82	13.40 ± 1.46
Shore Hardness [Sh°A]	90 ± 1.5	91 ± 1.2	92 ± 0.9	92 ± 0.8	93 ± 1.5
Resilience [%]	14.2 ± 0.6	18.4 ± 0.5	18.2 ± 0.8	8.8 ± 0.6	13.2 ± 0.6

The analysis of the obtained mechanical test results might be divided into two groups upon the use of different deaerators. In the first group, obtained with BYK 530 application, a comparison between compositions 1–3 shows that the cured product containing 0.3 wt.% of catalyst Dabco 33-LV (composition 2) presents the highest tensile strength and elongation at break. At the same time, this material has the highest, from all prepared samples, resilience and compression strength. On the other hand, composition 3 presents the highest flexural strength and elasticity flexural modulus. Similarly, within the group of BYK A525 deaerator, application of the catalyst leads to an increase of the tensile strength, elongation at break, impact strength and resilience, simultaneous decrease of the flexural strength and elasticity flexural modulus. All of the obtained compositions have a comparable hardness on the Shore A scale. Additionally, it had been observed that the application of the deaerator BYK A525 leads to an increase of the tensile strength and elongation at break of the obtained material. It is worth to mention here that supplementary mechanical properties are closely related to the amount as well as the type (according to results of different experiments performed in our research group) of applied catalyst. Comparison of hybrid epoxy-polyurethane materials cured with 4,4'-methylene diphenyl diisocyanate with other polymeric materials indicates that mechanical resistance of obtained compositions is higher not only than commercial low molecular weight epoxy resin Ruetapox 162 cured with methyltetrahydrophthalic anhydride, but also elastic polyurethane materials based on hydroxyl soybean oil [24–25]. On the other hand, our materials have worse mechanical strength than epoxy resin cross-linked with isophoronediamine [21].

#### 4. Conclusions

Our research presented in above paper is closely related to the latest environmental concerns, paying special attention to bio- and renewable resources as feedstock for the chemical industry. Application of vegetable oils gives the opportunity to obtain novel epoxy materials with various interesting properties, which may be designed by the proper selection of hardener, catalyst and deaerator of the curing process. The above-discussed investigations describe the synthesis and selected mechanical properties of compositions based on the product of the fusion reaction of the modified soybean oil and bisphenol A, subsequently cross-linked with MDI in the presence of various amounts of catalyst Dabco 33-LV and

two different deaerators on silicone basis (BYK A530 and BYK 525). It has been found that an application of the deaerator BYK A525 leads to an increase of the tensile strength and elongation at break of the obtained material without significant differences in the sample's appearance. Additionally, compositions prepared in the presence of catalyst Dabco 33-LV show a higher value of tensile strength, elongation at break, impact strength and resilience, when compared with samples without the use of catalyst.

## References

- [1] Czub P., *Modified natural oils and the products of chemical degradation of waste poly(ethylene terephthalate) as environmentally friendly raw materials for epoxy resins*, Publishing House of the Cracow University of Technology, Cracow 2008, 21.
- [2] Zhang L., Jeon H.K., Malsam J., Herrington R., Macosko C.W., *Substituting soybean oil-based polyol into polyurethane flexible foams*, Polymer, 48, 2007, 6656–6667.
- [3] Głowińska, E., Datta J., *Możliwości wykorzystania modyfikowanych olejów sojowego i palmowego w syntezie biopoliuretanów*, Przemysł Chemiczny, 91.6, 2012, 1234–1236.
- [4] Pietrzak K., Kirpluks M., Cabulis U., Ryszkowska J., *Effect of the addition of tall oil-based polyols on the thermal and mechanical properties of ureaurethane elastomers*, Polymer Degradation and Stability, 108, 2014, 201–211.
- [5] Sharma V., Kundu P.P., *Addition polymers from natural oils-A review*, Progress in Polymer Science, 31, 2006, 983–1008.
- [6] Hatti-Kaul R., Tornvall U., Gustafsson L., Borjesson P., *Industrial biotechnology for the production of bio-based chemicals – a cradle-to-grave perspective*, Trends in Biotechnology, 25.3, 2007, 119–124.
- [7] Belgacem M. N., Gandini, A., *Materials from vegetable oils: major sources, properties and applications, Monomers, polymers and composites from renewable resources*, 1 ed., Elsevier, ch.3, Great Britain 2008.
- [8] Kuciel S., Kuźniar P., Liber-Kneć A., *Polyamides from renewable sources as matrices of short fiber reinforced biocomposites*, Polimery, 57.9, 2012, 627–634.
- [9] Eggink G., Waard P.D., Huijberts, G.N., *Formation of novel poly (hydroxyalkanoates) from long-chain fatty acids*, Canadian Journal of Microbiology, 41.13, 1995, 14–21.
- [10] Clatty J.L., *Condensation polymerization of polyisocyanate, polyol, and vegetable or fish oil; catalysis, crosslinking, chain extension*, U.S. Patent No. 6 649 667, 2003.
- [11] Alam, M., Akram, D., Sharmin, E., Zafar, F., Ahmad, S., *Vegetable oil based eco-friendly coating materials: A review article*, Arabian Journal of Chemistry, 7.4, 2014, 469–479.
- [12] Hintze-Brüning, H., *Utilization of vegetable oils in coatings*, Industrial Crops and Products, 1.2, 1992, 89–99.
- [13] Czub P., *Application of Natural Oils as Reactive Diluents for Epoxy Resins*, Macromolecular Symposia, 242, 2006, 60–64.
- [14] Czub P., *Kompozycje epoksydowe z wykorzystaniem modyfikowanych olejów roślinnych*, Polimery, 53.3, 2008, 182–189.

- [15] Czub P., *Synthesis of high-molecular-weight epoxy resins from modified natural oils and Bisphenol A or Bisphenol A-based epoxy resins*, *Polymers for Advanced Technology*, 20.3, 2009, 194–208.
- [16] Czub P., *A comparison of the syntheses of high-molecular-weight epoxy resins using two groups of modified vegetable oils*, *Macromolecular Symposia*, 277, 2009, 162–170.
- [17] Czub P., Bończa-Tomaszewski Z., Penczek P., Pielichowski J., *Chemistry and technology of epoxy resins*, IV ed., WNT, Warszawa 2002, 60.
- [18] Górczyk J., Bogdał D., Pielichowski J., Penczek P., *Żywice epoksydowe o zwiększonym ciężarze cząsteczkowym: synteza i charakterystyka termiczna*, *Polimery*, 51, 2006, 781–786.
- [19] Czub P., *Zastosowanie epoksydowanego oleju sojowego do regulowania lepkości kompozycji epoksydowych*, *Polimery*, 51.11–12, 2006, 821–828.
- [20] Czub P., *Characterization of an epoxy resin modified with natural oil-based reactive diluents*, *Macromolecular Symposia*, 245–246, 2006, 533–538.
- [21] Czub P., Kasza P., *Właściwości mechaniczne usieciowanego izocyjanianami produktu reakcji modyfikowanego oleju sojowego i żywicy epoksydowej*, *Polimery*, 59.6, 2014, 466–476.
- [22] Chua S.-C., Xu X., Guo Z., *Emerging sustainable technology for epoxidation directed toward plant oil-based plasticizers*, *Process Biochemistry*, 47, 2012, 1439–1451.
- [23] Jackson R.J. (Shell Oil Company), *Epoxy Fusion Catalyst and Process*, U.S. Patent 4 829 141, 1989.
- [24] Suharto R.E., Kristianingrum S., Partana C.F., *Synthesis of Polyurethane Elastomer from Vegetable Oil and Methylene-4,4'-Diphenyldiisocyanate (MDI) as Surface Coating for Roller*, *International Conference on Mathematics and Natural Sciences (ICMNS)*, Bandung-Indonesia, 29–30.11.2006, 639–642.
- [25] Wang S., Yang L., Ni B., Shi G., *Polyurethane Networks from Different Soy-Based Polyols by the Ring Opening of Epoxidized Soybean Oil with Methanol, Glycol, and 1,2-Propanediol*, *Journal of Applied Polymer Science*, 114(1), 2009, 125–131.



ADAM ŻABA, SVITLANA SOVINSKA, WIKTOR KASPRZYK,  
DARIUSZ BOGDAŁ, KATARZYNA MATRAS-POSTOLEK\*

## ZINC SULPHIDE (ZnS) NANPARTICLES FOR ADVANCED APPLICATION

### NANOCZĄSTKI SIARCZKU CYNKU (ZnS) DO ZAAWANSOWANYCH APLIKACJI

#### Abstract

Zinc sulphide (ZnS) is one of the first discovered semiconducting materials, which due to their unique properties can be applied in optoelectronic devices, such as ultraviolet-light-emitting diodes, flat-panel displays, electroluminescent and sensors. As we present in this short review, the properties of ZnS are highly dependent on their size, structural form and morphology. Nowadays, one-dimensional (1D) structures of ZnS have been of great interest, mainly due to their luminescent and electrical properties.

*Keywords: zinc sulphide, nanoparticles, optoelectronic devices*

#### Streszczenie

Siarczek cynku (ZnS) jest jednym z pierwszych poznanych półprzewodnikowych materiałów, który dzięki swoim unikalnym właściwościom znalazł zastosowanie w optoelektronice m.in. do budowy diod świecących w zakresie ultrafioletu, płaskich monitorów, diod elektroluminescencyjnych i czujników. Jak zostanie to pokazane w tym krótkim artykule przeglądowym, właściwości ZnS silnie zależą od rozmiaru, morfologii i struktury krystalicznej. Obecnie szczególnym zainteresowaniem cieszą się jednowymiarowe kryształy (1D) ze względu na swoje właściwości luminescencyjne i elektryczne.

*Słowa kluczowe: siarczek cynku, nanocząstki, urządzenia optoelektroniczne*

\* M.Sc. Adam Żaba, M.Sc. Svitlana Sovinska, M.Sc. Wiktor Kasprzyk, Prof. Dariusz Bogdał, Ph.D. Katarzyna Matras-Postolek, Department of Biotechnology and Physical Chemistry, Faculty of Chemical Engineering and Technology, Cracow University of Technology.

## 1. Introduction

The properties and applications of zinc sulphide (ZnS) nanoparticles (NPs) and related materials have been the fields of research over the last decade [1]. The nanostructures of ZnS, according to Siegel's classification, can be divided into zero-dimensional (0D), one-dimensional (1D) and two-dimensional (2D) structures [2, 3]. Different forms of one-dimensional ZnS nanostructures have been fabricated, for example: nanowires, nanotowers and nanotubes [1]. ZnS nanocrystals can be synthesised via several types of methods, including the microwave-assisted reaction, the micro-emulsion processes, the vapour-liquid-solid growth method, electrospinning and solvothermal methods [4]. Zinc sulphide is a semiconductor with very unique properties, which can be found in one of the two structural forms – cubic sphalerite or hexagonal wurtzite. This nontoxic material, which is chemically more stable than other semiconductors, is characterised with a wide band-gap energy of ~3.7 eV [5]. Because of these properties, ZnS nanoparticles can be used in both biomedical and optoelectronic applications, such as biosensors, biocomposites [6] light-emitting diode (LED), screens, sensors or lasers [5] or nanocomposites [7].

This short review is concentrated especially on the optoelectronic applications of materials based on 1D ZnS nanocrystals. The selected methods of synthesis, as well properties and applications of these materials, will be presented.

## 2. One-dimensional nanostructures

Nanomaterials are a group of materials, which have at least one size between 1 to 100 nm. Siegel classified nanostructured materials into four categories according to their dimensionality: zero dimensional, one dimensional, two dimensional and three dimensional [3]. In the first category, the atomic clusters, filaments and cluster assemblies are classified. The multilayers are classified as one dimensional nanomaterial. The third category contains ultrafine-grained overlayers or buried layers. The nano-phase materials consisting of equiaxed nanometre-sized grains are classified as three dimensional. According to the above information, 1D nanostructures possessed two dimensions on the nanoscale range, i.e. the diameter of the tube is below 100 nm and its length could be much greater. It is believed that 1D nanostructures are the best systems for exploring a large number of novel phenomena at the nanoscale, and investigating the size and dimensionality dependence of functional properties. 1D crystals also play an important role as interconnects or the key units in the fabricating electronic, optoelectronic, electrochemical and electromechanical devices [1, 3, 7].

One-dimensional nanostructures are characterised with two nanoscale dimensions, so the movement of electrons is limited in these dimension. The free flow of electrons is possible only in one direction – along the nanoparticles. For a nanostructure with a square cross-section, the total energy can be described by the below equation (1):

$$E_{n,m,k_x} = \frac{h^2 n^2}{8m^* L_z^2} + \frac{h^2 m^2}{8m^* L_y^2} + \frac{h^2 k_x^2}{8m^*} \quad (1)$$

where:

$$\begin{aligned} E_{n,m,k_x} & - \text{total energy,} \\ h & - \text{Planck constant} \end{aligned}$$

$m^*$  – mass of the electron,  
 $L_z, L_y$  – nanoscale dimensions in 1D structure,  
 $n, m, = 1, 2, 3.$

Total energy depends on two quantum numbers and the wave vector for electron's movement along the  $k_x$  dimension. The real nanostructures have more complicated shapes than the above example. In order to compute the total energy, numerical solving of an appropriate Schrödinger equation is necessary [8].

One-dimensional nanocrystals can form a variety of shapes (Fig. 1). In the recent years, the preparation of such morphologies of 1D nanocrystals as nanotubes, nanobelts, nanocombs, nanoawls, nanotowers, and the most important nanorods and nanowires, have been reported. The classification of morphologies of 1D nanostructures is not entirely clear. It is believed that nanowires are long, flexible and have a circular cross-section in contrast to nanorods, which are shorter, stiffer and have a hexagonal cross-section [1]. All of the various morphologies of one-dimensional nanostructures are presented in Fig. 1.

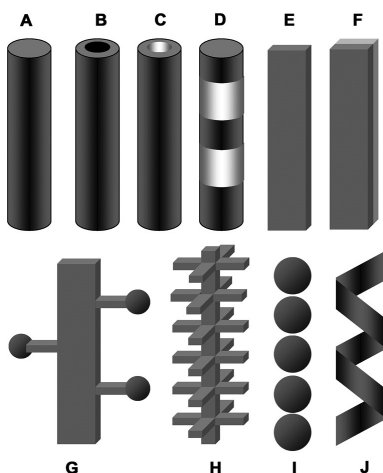


Fig. 1. Different morphologies of 1D nanostructures: nanowire (A), core-shell structure (B), nanotube (C), heterostructure (D), nanobelt (E), nanotape (F), dendrite (G), hierarchical nanostructure (H), nanosphere assembly (I) and nanosprings (J) [9]

There are several methods by which one-dimensional nanostructures can be obtained: spontaneous growth from the liquid or the vapour phase; synthesis based on templates; solvothermal methods with the electrospinning method and with lithography [1, 4].

### 3. Zinc sulphide – crystallographic forms

ZnS has two available allotropic forms. One is with the hexagonal crystallographic form and it is named wurtzite. The second, more common and stable form has a cubic crystallographic structure and it is named zinc blende. The wurtzite and the zinc blende forms have band gaps of about 3.77 and 3.72 eV, respectively. The zinc blende transforms

into wurtzite at temperatures over 1052°C [1, 10]. The crystal structures of zinc sulphide are presented in Fig. 2. The nanoparticles of ZnS can change their crystallographic form easier than particles in the macroscale. The zinc sulphide nanocrystals can transform from zinc the blende to wurtzite at about 400°C [1].

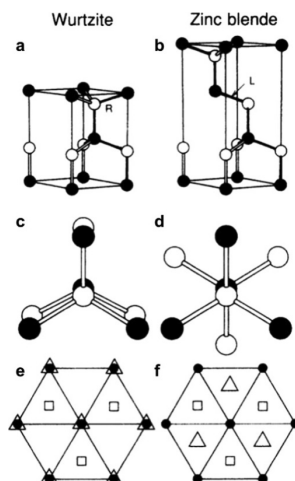


Fig. 2. Crystal forms of zinc sulphide. Difference in the hardness of the fourth interatomic bond along the right (R) for wurtzite and along the left (L) for zinc blende (a, b). The respective eclipsed and staggered dihedral conformations (c, d). Atomic arrangement along the close packing axis (e, f) [1]

The crystal structure has an impact on the bonds energy. Between the cubic and the hexagonal form, the difference in the bond energy is about 5.6 meV/atom. For one-dimensional nanoparticles, the diameter has an influence on the bond's energy. The energy bond decreases with the increase of the nanoparticle's diameter. This phenomenon is observed only for the material that is in the nanoscale. For the bulk material, the diameter has no impact to the value of the bond's energy [11]. In Fig. 3, the influence of diameter on the bond's energy is depicted. For the bulk material, the bonds energy is stable for different diameters in contrast to ZnS nanowires. For the lower values of crystal diameters, the bond's energy is higher. The difference in the bond energy between cubic and hexagonal forms is also depicted.

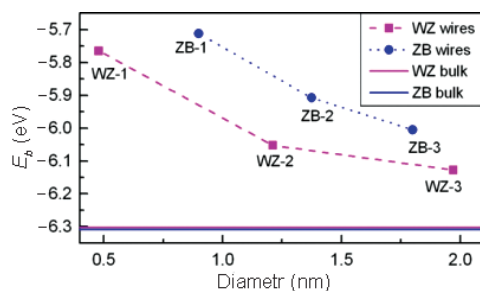


Fig. 3. The influence of diameters ZnS nanowires on bonds energy [11]

#### 4. Photo- and electroluminescence of ZnS

ZnS is well known for its photoluminescence (PL) and electroluminescence (EL). ZnS-based phosphors exhibit excellent conversion efficiencies for fast electrons into electron-hole pairs [12]. The PL properties of ZnS (1D) nanocrystals in most cases depend on their shape or size, but for example for nanowires and nanoribbons, they are very similar. The PL measurement of both structures of ZnS at room temperature shows strong and broad emission spectra with the maximum centred at 398 nm [13]. Generally, the 1D ZnS nanoparticles have a strong green emission band, centred at about 530–540 nm, and a weaker blue emission band, centred at about 440 nm [1].

The electroluminescence process is defined as non-thermal generation of light through the application of an electric field to the sample. Zinc sulphide is one of the best semiconducting functional materials for EL devices [14]. The temperature has a strong influence on the electroluminescence in ZnS. With an increase in the temperature, the EL brightness increases. The nanoparticles of ZnS also have a promising electroluminescence properties. They are used in semiconductor-based light emitting diodes (LEDs), which are described in section 6. The highly saturated colour emission could be obtained in such devices based on ZnS nanoparticles [1]. The ZnS nanoparticles are often doped with another metal in order to improve their EL properties. Doped ZnS nanocrystals have a high quantum efficiency with narrow emission and broad excitation spectra [15].

#### 5. Solvothermal synthesis of ZnS nanoparticles

The pioneers of the synthesis of ZnS nanocrystals were Brus and co-workers. They successfully synthesised it first time via a colloidal reaction of ZnS colloidal nanoparticles in the 1980's. Sodium sulphide and zinc perchlorate in the methanol and water were used as the sources of sulphide and zinc [1]. Nowadays 1D ZnS nanocrystals can be fabricated by many different methods. The synthesis can be carry in gas or liquid phase. The following belong to the most common methods of receiving ZnS nanoparticles: synthesis with microwave irradiation [16]; micro-emulsion techniques [17]; the vapour-liquid-solid growth method [18]; the solution-liquid-solid growth [2]; synthesis with template; electrospinning [19]; and the most common solvothermal methods [2, 5].

Originally, the solvothermal synthesis was called hydrothermal because of the use of water as a solvent. The reactions were kept in a sealed reaction container with a temperature of above 100 °C. The pressure in the container was determined by the temperature and the volume of the solvent in the vessel. Usually, the hydrothermal reactions were kept at a temperature of about 300 °C. At that temperature, the water is in the supercritical regime. Nowadays, the water is replaced with nonaqueous solvents, such as alcohols, benzene, polyamines or hydrazine. The reaction temperature is kept above the boiling point of the solvent. The most popular container is a Teflon vessel, so that the reaction can be kept at about 270°C under a pressure nearing to 150 bar [2].

Solvothermal synthesis has a few advantages over the other methods of synthesis of nanoparticles. With the solvothermal methods, it is possible to remove diffusion control by the use of a suitable solvent under mild condition. Due to the use of various precursors and reaction environments, it is possible to control the physicochemical and morphological

properties of the obtained product, and the time of synthesis is usually shorter than that of other methods. The influence of parameters on the reaction is not exactly known, due to the possible synergistic effects. It is known that the temperature, pressure, percentage fill of the vessel or used reagents have an influence on the final product [2], 20]. At lower temperatures, the substrates could not react fully, but the higher temperature could cause the formation of bigger nanoparticles. The longer time of reaction mostly caused an increase of the average diameter of nanocrystals [20]. The percentage fill of the vessel has an influence on the reaction pressure. An increase of pressure could lead to the formation of smaller nanoparticles [21]. For the ZnS 1D nanoparticles, various temperatures (130–200°C) and reaction times (for few minutes to 20 hours) are used [10, 22, 23].

## 6. Applications of ZnS nanocrystals – optoelectronic devices

ZnS nanocrystal semiconductors are one of the most interesting and important groups of compounds used in electronic and optoelectronic devices. The development of these materials is one of the most important trends in this field [24].

1D nanocrystals can be used in Field-Effect Transistors (FETs). He et al. fabricated FET based on ZnS/SiO<sub>2</sub> core/shell nanocables. For the fabrication of FETs, the synthesised ZnS/silica nanocables were transferred from the Si substrate to Au/Ti electrodes. In order to firmly contact the Au/Ti metal electrodes and ZnS core of the nanocable, focused ion beam microscopy was used to cut the nanocable at the two ends of exposed ZnS core. Then, a Pt mixture was deposited at the ends in order to make contacts between the ZnS core and Au/Ti electrodes [25]. The typical FET is a three terminal device. The names of terminals refer to their function and they are called: gate, drain and source. The gate terminal controls the opening and closing of the physical gate with permits or blocks of electron flow by creating or eliminating conductive the channel between drain and source [24]. An example of FET is presented in figure 4. The grey balls in Figure 4 illustrate the crystals of the semiconductor.

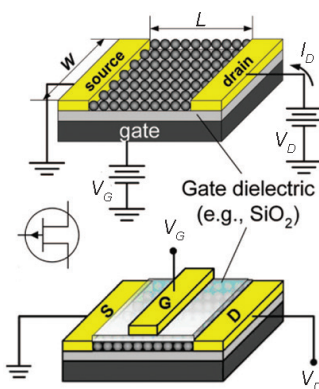


Fig. 4. Typical bottom-gated (a) and top-gated (b) of Field-Effect Transistors [24]

The connecting source with a drain is called the semiconductor channel. For the isolator, the most commonly used materials are silicon or aluminium oxides in the polymer matrix [24].

The other devices, where the one-dimensional ZnS nanocrystals are very useful, are Light-Emitting Diodes. In a typical LED, a thin layer of light emitting nanocrystals is placed between the hole and the electron transporting layers. The recombination of the electron-hole pairs in the nanocrystals generates photons with energy corresponding to the gap between the highest occupied (1Sh) and the lowest unoccupied (1Se) states in the nanocrystal [24]. A typical thin film LED with semiconductor nanocrystals is presented in Fig. 5.

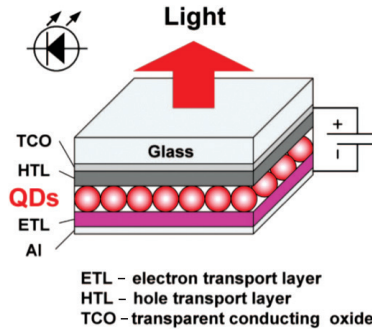


Fig. 5. Schematic picture of a thin film LED with semiconductor nanocrystals [24]

The LEDs are characterised by External Quantum Efficiency, which is the ratio of the number of photons emitted into free space to the number of injected carriers.  $\eta_{ext}$  can be defined as (2):

$$\eta_{ext} = \frac{\text{(number of emitted photons per second)}}{\text{(number of electrons injected into LED per second)}} = \frac{P/h\nu}{I/e}$$

where:

- $h$  – Planck constant,
- $e$  – electron charge,
- $P$  – optical power emitted into free space,
- $I$  – injection current,
- $\nu$  – frequency.

The most important properties of LEDs are:

- the high purity of the emitted light,
- the light emission proportional to the current,
- unordered spontaneous emission,
- fairly broad continuous spectrum of emission,
- low power emission signal – below 100 mW,
- much lower cost in comparison with the semiconductor laser [12, 24].

Lu et al. fabricated Organic LED (OLED) with a ZnS nanocolumn. The ZnS nanocolumn was grown on the indium tin oxide (ITO) substrates by the glancing angle deposition technology. The inorganic ZnS material was evaporated onto ITO by the electron beam deposition method. The electroluminescence of OLED with ZnS 1D nanocrystals was about 1.2 times bigger than that of devices with a continuous layer or without a layer of ZnS [26].

The last important devices based on one-dimensional nanocrystals are photodetectors and solar cells. There is a large variety of sensitive photon detection devices operating in the visible spectral range, but in the infrared, the available detection systems are insensitive or very expensive. The last studies focus on the photodetectors with semiconductor nanocrystals or the blend of the nanocrystals connecting with the semiconducting organic materials [24]. The typical photodetector based on the nanocrystals is presented in Fig. 6.

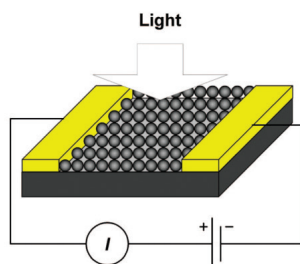


Fig. 6. Schematic picture of a typical NCs-based photodetector [24]

The progress in NC-based photoconductors allow to produce the near-IR detectors with device characteristics comparable to commercial devices [24].

The demand for renewable sources of energy implies the development of efficient and inexpensive photovoltaic materials. Due to the optical and electronic properties of semiconductor nanocrystals, these materials are promising candidates for producing new and inexpensive photovoltaic devices. Photovoltaic cells based on materials that absorb light and separate photogenerated electrons and holes, and replace the light energy with the electrical energy [24]. The schematic solar cell with n- and p- conductivity is presented in Fig. 7.

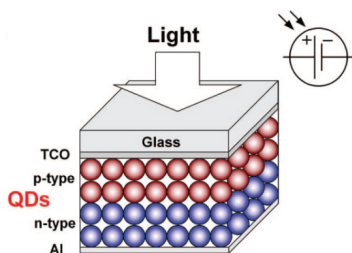


Fig. 7. The schematic solar cell with n- and p- conductivity [24]

The current polymer solar cell with single nanocrystals can achieve a power conversion efficiency of about 5%. For the tandem solar cell with different band gaps, it is possible to achieve about 7%. The outdoor lifetime of such materials is more than 1 year [24]. Huang et al. improved the efficiency of Si-based solar cell with ZnS nanoparticles. The obtained efficiency increased from 6.57 to 7.20% [27].

## 7. Conclusion

The one-dimensional nanocrystals of zinc sulphide have very interesting electrical and optoelectrical properties. There are several methods to obtain this material. The most popular are the solvothermal methods. The optoelectronic industries focus on producing new devices, which are based on the semiconductor nanoparticles. The one-dimensional nanocrystals of ZnS are a promising material for electric and optoelectronic devices due to their low production cost and good optical and electrical properties.

*This work was financially supported by the Foundation for Polish Science within the VI edition of the Homing Plus program, project number HOMING PLUS/2012-6/5 and National Centre for Research and Development under Lider Program, contract no. LIDER/009/185/L-5/13/NCBR/2014.*

## References

- [1] Fang X., Zhai T., Gautam U.K., Li L., Wu L., Bando Y., Golberg D., *ZnS nanostructures: From synthesis to applications*, Prog. Mater. Sci., Vol. 56(2), 2011, 175–287.
- [2] Adachi M., Lockwood D.J., *Self-Organized Nanoscale Materials*, Springer Science+Business Media, 2006.
- [3] Siegel R.W., *Characterization of nanoparticle and nanophase materials*, <http://www.osti.gov/scitech/biblio/10133547> (online: 25.06.2016).
- [4] Cao G., *Nanostructures & Nanomaterials*. Imperial College Press, 2004.
- [5] Ali H., Karim S., Rafiq M.A., Maaz K., Rahman A.U., Nisar A., Ahmad M., *Electrical conduction mechanism in ZnS nanoparticles*, J. Alloys Compd., Vol. 612, 2014, 64–68.
- [6] Wu P., He Y., Wang H.F., Yan X.P., *Conjugation of glucose oxidase onto Mn-doped ZnS quantum dots for phosphorescent sensing of glucose in biological fluids*, Anal. Chem., Vol. 82(4), 2010, 1427–1433.
- [7] Dutta K., Manna S., De S.K., *Optical and electrical characterizations of ZnS nanoparticles embedded in conducting polymer*, Synth. Met., Vol. 159(3–4), 2009, 315–319.
- [8] Kelsall R.W., Hamley I.W., Geoghegan M., *Nanotechnologie*, Wydawnictwo Naukowe PWN, Warsaw 2008.
- [9] Kuchibhatla S.V.N.T., Karakoti A.S., Bera D., Seal S., *One dimensional nanostructured materials*, Prog. Mater. Sci., Vol. 52(5), 2007, 699–913.
- [10] Biswas S., Kar S., *Fabrication of ZnS nanoparticles and nanorods with cubic and hexagonal crystal structures: a simple solvothermal approach*, Nanotechnology, Vol. 19(4), 2008.
- [11] Chen H., Shi D., Qi J., Jia J., Wang B., *The stability and electronic properties of wurtzite and zinc-blende ZnS nanowires*, Phys. Lett. A, Vol. 373,(3), 2009, 371–375.
- [12] Rohwer L.S., Nalwa H.S., *Handbook of Luminescence, Display Materials, and Devices: Display devices*, American Scientific Publishers, 2003.
- [13] Kar S., Chaudhuri S., *Controlled synthesis and photoluminescence properties of ZnS nanowires and nanoribbons*, J. Phys. Chem. B, Vol. 109(8), 2015, 3298–302.

- [14] Bringuier E., *Tentative anatomy of ZnS-type electroluminescence*, J. Appl. Phys., Vol. 75(9), 1994, 4291–4312.
- [15] Bryan J.D., Gamelin D.R., *Doped Semiconductor Nanocrystals: Synthesis, Characterization, Physical Properties and Applications*, Prog. Inorg. Chem., Vol. 54, 2005, 47–126.
- [16] Zhao Y., Hong J.M., Zhu J.J., *Microwave-assisted self-assembled ZnS nanoballs*, J. Cryst. Growth, Vol. 270(3–4), 2004, 438–445.
- [17] Li Y., He X., Cao M., *Micro-emulsion-assisted synthesis of ZnS nanospheres and their photocatalytic activity*, Mater. Res. Bull., Vol. 43(11), 2008, 3100–3110.
- [18] Hao Y., Meng G., Wang Z.L., Ye C., Zhang L., *Periodically twinned nanowires and polytypic nanobelts of ZnS: The role of mass diffusion in vapor-liquid-solid growth*, Nano Lett., Vol. 6(8), 2006, 1650–1655.
- [19] Lin D., Wu H., Zhang R., Pan W., *Preparation of ZnS Nanofibers Via Electrospinning*, J. Am. Ceram. Soc., Vol. 90(11), 2007, 3664–3666.
- [20] Walerczyk W., *Solvothermalna synteza nanokrystalicznych spineli glinowo-cynkowych modyfikowanych jonami metali przejściowych jako katalizatorów i nośników katalizatorów* [online: 25.03.2016] <http://biblioteka.intibs.pl/lib/exe/fetch.php?media=doktoraty-w:wiktoria.walerczyk.pdf>. (online: 25.03.2016).
- [21] Demazeau G., *Impact of high pressures in solvothermal processes*, J. Phys. Conf. Ser., Vol. 215(1), 2010.
- [22] Fan L., Song H., Zhao H., Pan G., Yu H., Bai X., Li S., Lei Y., Dai Q., Qin R., Wang T., Dong B., Zheng Z., Ren X., *Solvothermal synthesis and photoluminescent properties of ZnS/cyclohexylamine: inorganic-organic hybrid semiconductor nanowires*, J. Phys. Chem. B, Vol. 110(26), 2006, 12948–12953.
- [23] Xi G., Wang C., Wang X., Zhang Q., Xiao H., *From ZnS, en 0.5 Nanosheets to Wurtzite ZnS Nanorods under Solvothermal Conditions*, J. Phys. Chem. C, Vol. 112, 2008, 1946–1952.
- [24] Talapin D.V., Lee J.S., Kovalenko M.V., Shevchenko E.V., *Prospects of Colloidal Nanocrystals for Electronic and Optoelectronic Applications*, Chem. Rev., Vol. 110, 2010, 389–458.
- [25] He J.H., Zhang Y.Y., Liu J., Moore D., Bao G., Wang Z.L., *ZnS / Silica Nanocable Field Effect Transistors as Biological and Chemical Nanosensors*, J. Phys. Chem. C., Vol. 111(33), 2007, 12152–12156.
- [26] Lu L., Xu Z., Zhang F., Zhao S., Wang L., Zhuo Z., Song D., Zhu H., Wang Y., *Using ZnS Nanostructured Thin Films to Enhance Light Extraction from Organic Light-Emitting Diodes*, Energy Fuels, vol. 24, 2010, 3743–47.
- [27] Huang C.Y., Wang D.Y., Wang C.H., Chen Y.T., Wang Y.T., Jiang Y.T., Yang Y.J., Chen C.C., Chen Y.F., *Efficient light harvesting by photon downconversion and light trapping in hybrid ZnS nanoparticles/Si nanotips solar cells*, ACS Nano, vol. 4(10), 2010, 5849–5854.

## CONTENTS

Berkowicz G., Bradło D., Żukowski W.: Cenospheres as an innovative fluidised bed material .....	3
Djas M., Henczka M.: Influence of mixing on the course of reactive extraction of citric acid using supercritical CO <sub>2</sub> .....	
Gaca K.Z.: A review: The influence of the catalyst on formation and properties of resorcinol-formaldehyde gels.....	19
Gwadera M., Larwa B., Kupiec K.: Modelling of heat conduction in the ground.....	27
Komorowicz T., Neupauer K., Sabat K., Głuszek A.: Laboratory tests of photovoltaic modules formed of multicrystalline silicon cells .....	39
Kuc J., Grochowalski A., Świergosz T.: Correlation of hexabromocyclododecane and content of fat in fish.....	49
Larwa B., Teper M., Kupiec K.: Horizontal ground heat exchangers – analytical solutions and numerical simulations .....	57
Malinowska M., Śliwa K., Sikora E., Ogonowski J.: Qualitative analysis of the main polyphenols contained in apple pomace extract.....	69
Marszałek M., Kowalski Z., Makara A.: Application of pressure-driven membrane techniques for the recovery of water and fertilising components from pig slurry .....	77
Miastkowska M., Sikora E., Ogonowski J.: Nanoemulsions based on selected berry seed oils.....	91
Neupauer K., Komorowicz T., Kupiec K.: Cooling of hot water with non-uniform initial temperature .....	101
Sienkiewicz A., Czub P.: Synthesis and mechanical properties of novel epoxy-polyurethane materials based on modified soybean oil.....	111
Żaba A., Sovinska S., Kasprzyk W., Bogdał D., Matras-Postołek K.: Zinc sulphide (ZNS) nanoparticles for advanced application.....	125

## TREŚĆ

Berkowicz G., Bradło D., Żukowski W.: Cenofery jako innowacyjny materiał złoża fluidalnego.....	3
Djas M., Henczka M.: Wpływ mieszania na przebieg reaktywnej ekstrakcji kwasu cytrynowego z użyciem CO <sub>2</sub> w stanie nadkrytycznym.....	11
Gaca K.Z.: Przegląd: Wpływ katalizatora na powstawanie oraz właściwości żeli rezorcynowo-formaldehydowych.....	19
Gwadera M., Larwa B., Kupiec K.: Modelowanie przewodzenia ciepła w gruncie.....	27
Komorowicz T., Neupauer K., Sabat K., Głuszek A.: Badania laboratoryjne modułów fotowoltaicznych zbudowanych z polikrystalicznych ogniw krzemowych....	39
Kuc J., Grochowalski A., Świergosz T.: Badanie korelacji stężenia heksabromocyklododekanu i zawartości tłuszczu w rybach .....	49
Larwa B., Teper M., Kupiec K.: Gruntowe wymienniki ciepła – rozwiązania analityczne i symulacje numeryczne.....	57
Malinowska M., Śliwa K., Sikora E., Ogonowski J.: Analiza jakościowa głównych polifenoli zawartych w ekstrakcie z wytlóków z jabłek.....	69
Marszałek M., Kowalski Z., Makara A.: Zastosowanie ciśnieniowych procesów membranowych do odzysku wody oraz składników nawozowych z gnojowicy trzody chlewnej .....	77
Miastkowska M., Sikora E., Ogonowski J.: Nanoemulsje na bazie wybranych olejów z nasion owoców jagodowych.....	91
Neupauer K., Komorowicz T., Kupiec K.: Chłodzenie gorącej wody o niejednorodnej temperaturze początkowej.....	101
Sienkiewicz A., Czub P.: Synteza i właściwości mechaniczne nowych epoksydowo-poliuretanowych materiałów na bazie modyfikowanego oleju sojowego.....	111
Żaba A., Sovinska S., Kasprzyk W., Bogdał D., Matras-Postołek K.: Nanocząstki siarczku cynku (ZnS) do zaawansowanych aplikacji.....	125